2017

Determination of Stellar Parameters through the Use of All Available Flux Data and Model Spectral Energy Distributions

Gemunu Ekanayake
University of Kentucky, gbe8396@gmail.com
Digital Object Identifier: https://doi.org/10.13023/ETD.2017.170

STUDENT AGREEMENT:

I represent that my thesis or dissertation and abstract are my original work. Proper attribution has been given to all outside sources. I understand that I am solely responsible for obtaining any needed copyright permissions. I have obtained needed written permission statement(s) from the owner(s) of each third-party copyrighted matter to be included in my work, allowing electronic distribution (if such use is not permitted by the fair use doctrine) which will be submitted to UKnowledge as Additional File.

I hereby grant to The University of Kentucky and its agents the irrevocable, non-exclusive, and royalty-free license to archive and make accessible my work in whole or in part in all forms of media, now or hereafter known. I agree that the document mentioned above may be made available immediately for worldwide access unless an embargo applies.

I retain all other ownership rights to the copyright of my work. I also retain the right to use in future works (such as articles or books) all or part of my work. I understand that I am free to register the copyright to my work.

REVIEW, APPROVAL AND ACCEPTANCE

The document mentioned above has been reviewed and accepted by the student's advisor, on behalf of the advisory committee, and by the Director of Graduate Studies (DGS), on behalf of the program; we verify that this is the final, approved version of the student's thesis including all changes required by the advisory committee. The undersigned agree to abide by the statements above.

Gemunu Ekanayake, Student

Dr. Ronald Wilhelm, Major Professor

Dr. Christopher Crawford, Director of Graduate Studies

Determination of Stellar Parameters through the use of All Available Flux Data and Model Spectral Energy Distributions

---

DISSERTATION

A dissertation submitted in partial
fulfillment of the requirements for
the degree of Doctor of Philosophy
in the College of Arts and Sciences
at the University of Kentucky

By
Gemunu Ekanayake
Lexington, Kentucky

Director: Dr. Ronald Wilhelm, Professor of Physics and Astronomy
Lexington, Kentucky 2017

ABSTRACT OF DISSERTATION

Determination of Stellar Parameters through the use of All Available Flux Data and Model Spectral Energy Distributions

Basic stellar atmospheric parameters, such as effective temperature, surface gravity, and metallicity plays a vital role in the characterization of various stellar populations in the Milky Way. The Stellar parameters can be measured by adopting one or more observational techniques, such as spectroscopy, photometry, interferometry, etc. Finding new and innovative ways to combine these observational data to derive reliable stellar parameters and to use them to characterize some of the stellar populations in our galaxy is the main goal of this thesis.

Our initial work, based on the spectroscopic and photometric data available in literature, had the objective of calibrating the stellar parameters from a range of available flux observations from far-UV to far-IR. Much effort has been made to estimate probability distributions of the stellar parameters using Bayesian inference, rather than point estimates.

We applied these techniques to blue straggler stars (BSSs) in the galactic field, which are thought to be a product of mass transfer mechanism associated with binary stars. Using photometry available in SDSS and GALEX surveys we identified 85 stars with UV excess in their spectral energy distribution (SED) : indication of a hot white dwarf companion to BSS. To determine the parameter distributions (mass,

temperature and age) of the WD companions, we developed algorithms that could fit binary model atmospheres to the observed SED. The WD mass distribution peaks at $0.4M_{\odot}$, suggests the primary formation channel of field BSSs is Case-B mass transfer, i.e. when the donor star is in red giant phase of its evolution. Based on stellar evolutionary models, we estimate the lower limit of binary mass transfer efficiency $\beta \sim 0.5$.

Next, we have focused on the Canis Major overdensity (CMO), a substructure located at low galactic latitude in the Milky Way, where the interstellar reddening ($E(B-V)$) due to dust is significantly high. In this study we estimated the reddening, metallicity distribution and kinematics of the CMO using a sample of red clump (RC) stars. The average $E(B-V)$ (~ 0.19) is consistent with that measured from Schlegel maps (Schlegal et.al. 1998). The overall metallicity and kinematic distribution is in agreement with the previous estimates of the disk stars. But the measured mean alpha element abundance is relatively larger with respect to the expected value for disk stars.

KEYWORDS: Stellar parameters, Kurucz models, Blue straggler, Canis Major Overdensity, Red clump

Gemunu Ekanayake

May 4, 2017

Determination of Stellar Parameters through the use of All Available Flux Data and Model Spectral Energy Distributions

By

Gemunu Ekanayake

Director of Dissertation: Ronald Wilhelm

Director of Graduate Studies: Christopher Crawford

Date: May 4, 2017

ACKNOWLEDGMENTS

I would like to thank my advisor Prof. Ronald Wilhelm for all the support and guidance given throughout all these years. I'm eternally grateful for the opportunity you gave me to conduct research in astronomy. Most importantly thank you for being an awesome human being.

I also thank my committee members Prof. Renbin Yan, Prof. Thomas Troland and Prof. Sebasthiyan Bryson for their diverse guidance.

Last but not least, I would like to thank my parents and my sisters for their unconditional support.

TABLE OF CONTENTS

LIST OF FIGURES

LIST OF TABLES

Chapter 1 Introduction

The universe as we find it today, was created by the Big Bang about 13.8 Gyrs ago ([1]). After few billion years after the Big Bang, the Galaxies are formed. Understanding how these Galaxies formed and evolved through time is one of the fundamental objectives in modern astronomy.

Our home in the universe, Milky Way, gives us an unique opportunity to achieve this goal by measuring and analyzing the stars spread throughout the Galaxy. The Milky way galaxy consists of several billion stars of different ages, masses and sizes. The determination exact distribution of these stars is a difficult task, simply because we are living inside of it. But thanks to modern astronomy we have a good enough picture about the structure of our Galaxy. Milky way consists various stellar populations, each characterized by distinct spatial distribution, kinematics, and chemical content. The Milky Way is usually modeled by three discrete components;the thin disk, the thick disk, and the halo. However, these are by no means pure smooth distributions of stars, but rather combination of many different substructures. Due to the invention of modern sky surveys, evidence for much more complex substructures like stellar streams and overdensities are found.

Stars with initial masses between about 0.8 and 8 $M_{\odot}$ dominate the stellar populations in our Milky Way Galaxy. In this thesis we will be concerned with such low-intermediate mass stars, therefore the following discussion on stellar evolution is limited only to those stars.

1.1 Stellar Evolution

After the big-bang only hydrogen, helium and traces of lithium and deuterium were formed. All other elements identified today, including the main component of human

bodies, carbon, were formed later. Most elements lighter than iron are formed in main-sequence and old stars, while elements heavier than iron are originated in dying stars. Stars consist of roughly 6% percent of the baryonic matter [2].

According to recent observational studies, long thin filaments were formed inside molecular clouds and, next, these filaments fragment into protostellar cores due to gravitational instability, when their linear density exceeds a certain threshold. [3] An object may be called a star if it is able to generate energy by nuclear fusion at a level sufficient to stop the contraction due to gravity.

A star like the sun, but in general all the low-intermediate stars with masses between 1-8 $M_{\odot}$ spend almost 90% of their life on the main sequence (MS) of the Hertzsprung-Russel diagram, which represents the luminosity of a star as a function of its effective temperature (Figure 1.1).

At this stage, stars keep their equilibrium through thermonuclear reactions, p-p chain or the CNO cycle, which convert Hydrogen into Helium. When a star exhausts its initial hydrogen supply in the core, the main sequence phase arrives to its end and the star begins to contract until the temperature and density are high enough to ignite hydrogen in a shell around the hydrogen-exhausted core. This, in turn, causes the star to expand and climb up the Red Giant Branch (RGB)

The evolution on the red giant branch is much faster than main sequence phase. When hydrogen exhausted in the core, the star begins to burn hydrogen in a shell around the core. when the convection in the envelope moves in to the region where nuclear reactions taking place, it can dredges up the material that has been produced by p-p chain and CNO cycle. This could alter the chemical composition of the outer surface of the star. At this stage the star starts to loose mass from its outer boundary through a slow stellar wind.

Stars with initial mass less than 2.2 $M_{\odot}$ develop a semi-degenerate core during the RGB phase. It accretes mass from the shell without contracting and remains

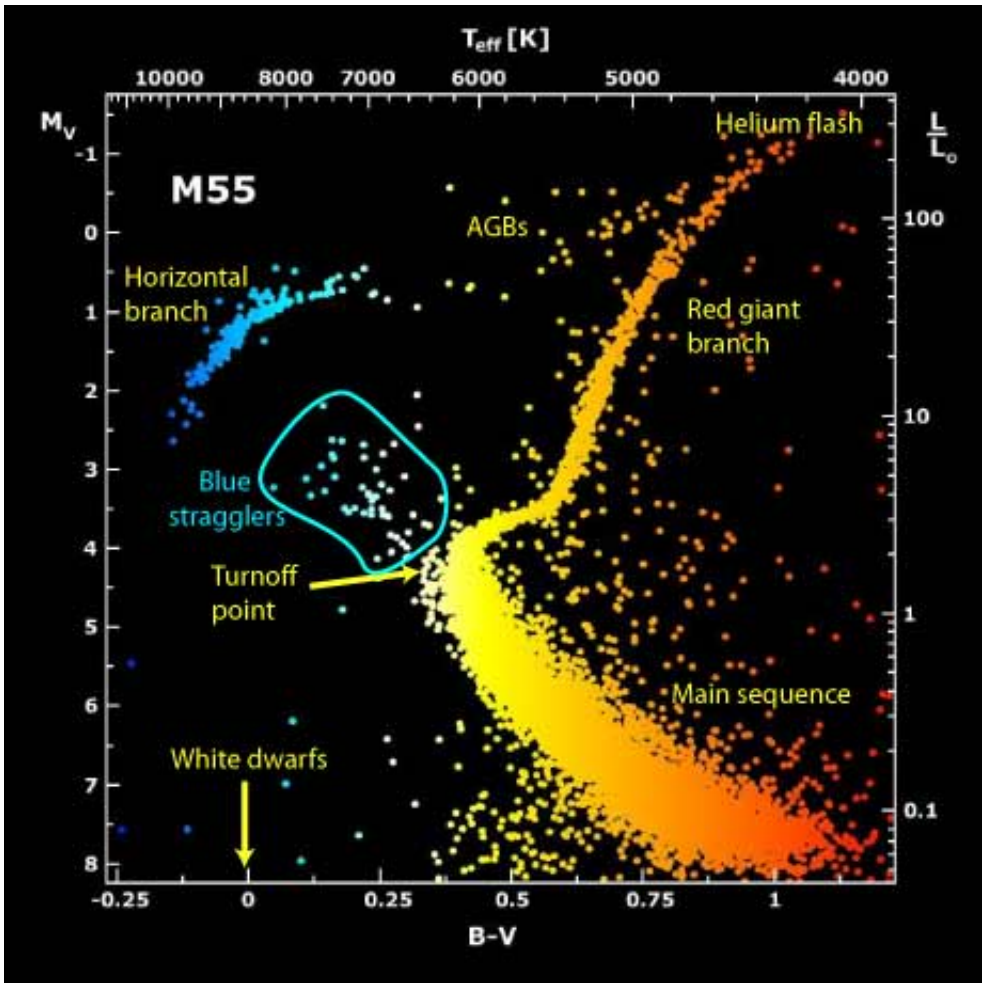

Figure 1.1: Hertzsprung-Russel diagram for globular cluster M55. Adopted from `http://www.atnf.csiro.au/outreach/education/senior/astrophysics/stellarevolution_clusters.html`

isothermal. Due to the partial degeneracy of the core the helium combustion temperature is lowered and initiate the 3α reaction causing a thermonuclear runaway. This semi-explosive ignition of helium burning is called He-flash.

Once the He-flash is finished star lands in the so called Zero Age Horizontal Branch in the HR diagram. For low mass stars the He-flash occurs when the core mass reaches $\sim .5\ M_{\odot}$. This number is key to determine the position of the star lands in ZAHB. Stars with small ratio of M_{core}/M_{star} lands in blue end of the ZAHB while stars with larger ratio lands in red end of ZAHB. This is simply because the thicker envelope

able to shield the hotter star and appear redder and cooler. For these reasons stars with intermediate mass occupy the reddest part of the ZAHB, creating the so called red-clump. During horizontal branch phase stars burn helium in their cores stably, via 3α reaction. Once the helium is exhausted in the core star starts to move towards the Asymptotic Giant Branch (AGB).

At the end of HB phase, stellar core consisting of carbon and oxygen. During the early AGB (EAGB) phase the shell of hydrogen, still on, continues to deposit helium in the layer that separates it from the core of C-O, making it more and more degenerate. Again similar to He-flash, the degeneracy lowers the ignition temperature of the helium until the shell lights up in a semi-explosive way. The shell of helium becomes dominant, and continues to deposit CO on the core, making it more and more degenerate. At the same time the inter-shell stops progressively to expand until the shell of hydrogen returns to dominate. During this phase of EAGB, the stars with the mass larger than $4.6M_{\odot}$

can experience the second chemical mixing process. As already mentioned, the expansion of the structure allow the convection layers to penetrate from the outside. If this is sufficiently deep to arrive to the inter-shell, it can bring the elements such as He, C, N, O, to the surface which are the products of combustion of hydrogen.

The next phase is called Thermally Pulsing AGB (TPAGB) and during this period stars experience multiple thermal pulses. The fundamental process that occurs during TPAGB is the third dredge-up. The mixing during third dredge-up involves extremely profound regions of the star ($\sim$ 75 percent of the structure) and generates chemical signatures that differ form those characterizing the other two dredge-ups, such as an increase of the abundance of carbon at the surface.

During the entire duration of the AGB phase, the stars suffer substantial mass loss. This is due to the fact that the envelope of these stars is expanded and cooled, therefore causing to from layers of molecules and dust, which are then removed as

stellar wind by the effect of radiation pressure.

After about a dozen thermal pulses, the latest expansion is sufficient to allow the release of the outermost layers around the nucleus of CO which is rapidly becoming fully degenerate. With this phase, known as post-AGB, the nuclear-active evolution of the stars ends leading to the final stages of a stars life.

Stars with low-intermediate mass end their life cycle as white dwarf stars. The white dwarfs consists of the fully degenerate core and very thin outer layer. These objects evolve by cooling down at constant radius.

1.2 Stellar Parameters

In order to fully describe a star, a number of parameters should be known. The mass M, the luminosity L, and the radius R can be considered as the first order parameters that describe a star. Models of stellar evolution and stellar atmospheres are based on these parameters. In order to test stellar evolution theory and the stellar atmosphere theory, high-precision measured fundamental parameters for stars in various evolutionary stages are needed.

The set of parameters based on L,M and R are used in studies that are closer to directly observed quantities. Among those the effective temperature T_{eff} and the logarithmic of surface gravity $log\ g$ are the most useful parameters, given by following equations.

$$T_{eff} = \frac{L}{4\pi R^2 \sigma} \tag{1.1}$$

where, σ is the Stefan-Boltzmann constant.

$$g = \frac{GM}{R^2} \tag{1.2}$$

where G is the gravitational constant.

Most evolutionary calculations are presented as isochrones, i.e. mass dependent tracks of constant age, in a HR diagram.

In addition to the effective temperature and the surface gravity, the chemical composition of a star is required to fully understand the system.

Most common term used in astronomy to describe the chemical composition of an astronomical object is called metallicity (Z), which is the mass fraction of elements which have larger atomic numbers that hydrogen or helium. Together with the mass fraction of hydrogen (X) and helium (Y) that covers the whole range of elements (with $Z + X + Y = 1$). One often use the solar metallicity $Z = 0.0169$ as a reference, with $X = 0.7346$ and $Y = 0.2485$ ([4]). The metallicity is an important attribute since it will effect the properties of a galaxy. Typically only one mettalicty is being measured. For example the Fe abundance, since it is usually the easiest to measure. The usual convention is to represent the metallicity with respect to the value of the sun. i.e

$$[Fe/H] = log_{10}\frac{(Fe/H)}{(Fe/H)_{\odot}} \tag{1.3}$$

In addition to the parameters discussed above, few more parameters may be required to fully describe the physics of a star. These parameters include angular momentum, magnetic field, mass loss rate and pulsation period.

All of these parameters evolve as a function of time, where the zero-point is usually defined when the star appears first on the main sequence, i.e. the so so-called zero age main sequence (ZAMS). Therefore in order to compare the observations to theoretical models, the age of the star is required as an additional parameter in some cases.

1.3 Measuring stellar parameters

Fundamental stellar parameters mentioned in previous section, such as effective temperature and surface gravity, can be measured using one (or more) of several types

of observations, such as spectroscopy, photometry, interferometry, etc. This inference can be achieved by using theoretical models or empirical calibration library constructed beforehand. Then the stellar parameters can be obtained from the model or the standard star (in empirical libraries) that best fits the observed quantities. The spectra obtained from high-resolution spectrographs with high signal to noise ratio (S/N) gives the most precise estimations for stellar parameters. Among others the study of hydrogen barlmer lines, the excitation and ionization balance of iron lines , line ratios and spectral synthesis are the basic techniques used in spectroscopic studies.

Photometric measurements, which are relatively cheap to obtain compared to spectroscopy , are used to estimate stellar parameters for large numbers of stars. It is well established that photometric colors are particularly useful for estimating Teff, capable of producing a typical scatter of < 0.01dex relative to spectroscopic measurements, even in cases where only a single photometric color is available ([5]). Photometric estimates of surface gravity and metallicity, on the other hand, have proven more challenging.

Methods based on machine learning provide a promising pathway to estimate stellar parameters more accurately. The algorithms defining these methods are data-driven, built to learn relationships between observables and parameters of interest without relying on parametric physical models. Using machine-learning classifiers Debosscher et al. (2007, [6]) and Dubath et al. (2011, [7]) were able to successfully classify the variable stars.

1.4 Outline of this Thesis

The main purpose of this thesis is to measure accurate stellar parameters of stars, aiming to find the statistical clues to characterize the stellar populations in our Galaxy. In order to reach this goal it is necessary to find more precise methods of determina-

tion of stellar parameters, especially the effective temperature (T_{eff}), surface gravity ($log\ g$) and metallicity ($[Fe/H]$). To achieve this, several techniques were implemented such that all available data being used to construct the energy distribution of a given star.

At first we studied the Spectral Energy Distributions (SED) of old metal poor A-type stars aiming to upgrade the UV calibration of these stars. For that we used a sample of stars that have IUE and NGSL spectra in addition to the accurate photometry. Here we introduced a probabilistic method to infer stellar parameters using the observed SED. This study is presented in Chapter 2.

In Chapter 3 we present the results of detecting the Blue Straggler-White Dwarf (BSS-WD) binaries in the Galactic field. The fitting using the composite SED of the binary we identified eighty stars with WD companions. Here we present the potential mass transfer histories based on the parameters determined via SED fitting.

In chapter 4 we present a study on Canis Major Overdensity (CMO). We used data-driven method to infer the stellar parameters of the sample of stars towards CMO in order to select Red Clump (RC) stars. We used RC to measure the reddening, kinematics and chemical content towards the CMO.

Chapter 2 Stellar Parameters in UV

2.1 SED

The observed spectral energy distribution (SED) of a star can reveal a lot information about the properties of the star. The total radiation emitted by a star depends on various complex physical processes of the star and one has to be able to disentangle the components which make up the SED in order to understand those physical processes. The radiation received at the Earth surface depends not only on the radiation emitted by the star alone, but also on the interstellar processes that modifies the SED by absorbtion and scattering of the photons.

Stellar SED can be studied by using broad band photometry, where the flux is measured over a certain range of wavelength. The flux in different bands is measured via a filter which will only let through light of certain wavelengths, in a range specific for each band. Depending on the specifications of the telescope and the instrument, the flux is only measured in a limited number of bands. Therefore, to fully sample the SED of a star, a combination of instruments/telescopes is necessary.

To be able to determine the stellar atmospheric parameters that shaped the flux distribution coming out of the star we need to fit the model atmosphere flux to the observations.

2.2 SED Fitting UV

The importance of using ultra-violet photometry in stellar studies was pointed out in many studies (eg.[8]). UV is useful in characterizing the metalicity and the star formation history of young stellar populations ([9]), to study the α element enhancement of stars ([10]) and to estimate the uv-upturn ([11], [12]) or the contribution of

blue horizontal branch stars to the integrated flux in galaxies.

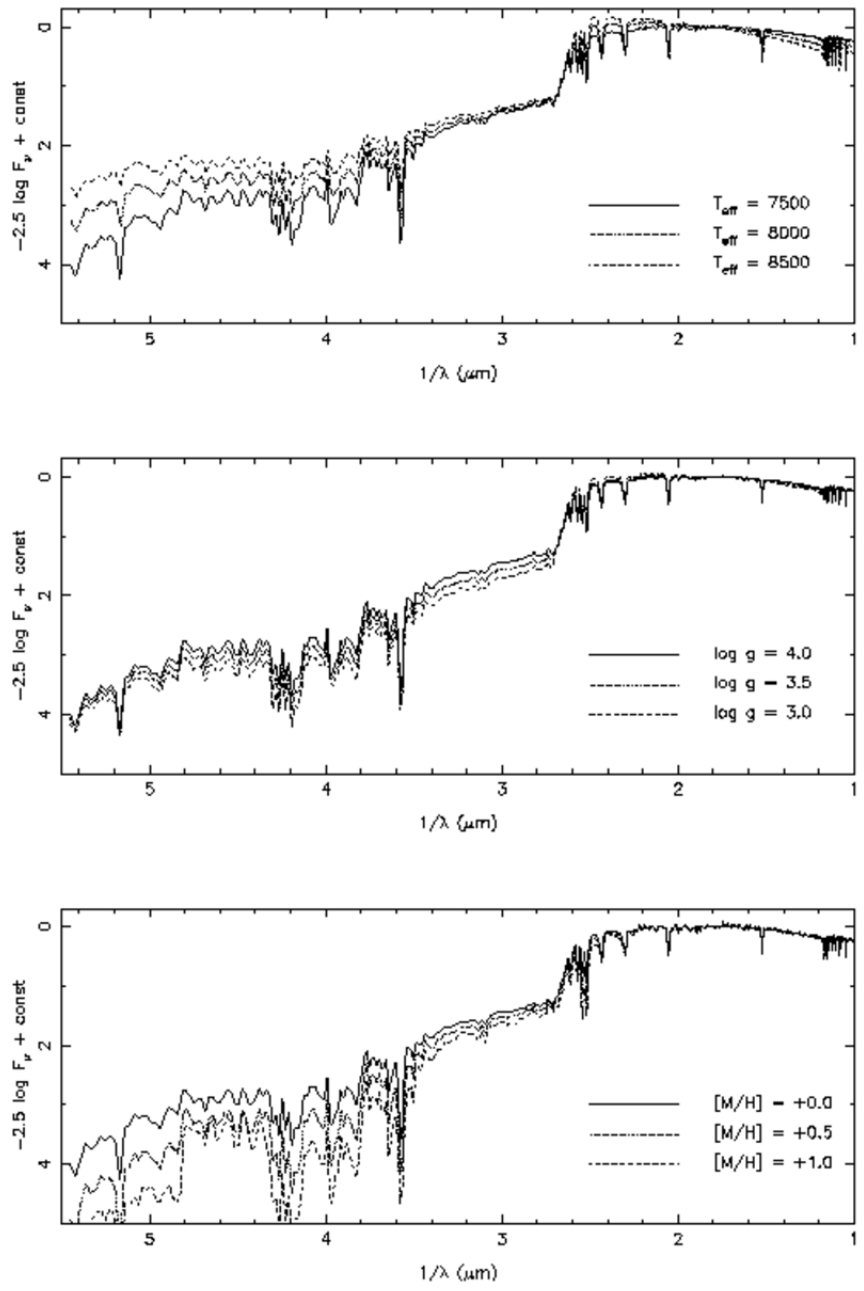

Figure 2.1: The sensitivity of flux distributions to Teff, log g and [M/H]. The solid line is for a model with Teff = 7500, log g = 4.0 and [M/H] = 0.0. The dotted and dashed lines indicate models with one of the parameters adjusted, as indicated. All fluxes have been normalized to zero at 5556.

In a simple stellar population (SSP) the blue wavelengths are highly sensitive to the hot stars like main-sequence turnoff, blue horizontal branch(BHB) or blue strag-

gler stars (BSSs). Figure 2.1 shows the sensitivity of the flux distribution to the various atmospheric parameters for an A-type model star. There is significant variation in the fluxes in UV region compare to the optical part when the model parameters are varied. The luminosity from these stars can have an important contribution to the integrated spectra ([13],[14]). It is vital to distinguish between the old and young stellar populations that contribute to the UV flux in order to properly characterize the stellar population. That process relies on identifying the different contribution to the different parts of the spectral energy distribution (SED). Therefore, combining optical and UV data is important aspect in SED studies. ([15])

Overwhelming majority of studies use Kurucz atmospheric models when comparing observed SED to synthetic SED to determine the stellar parameters. In optical wavelengths these synthetic spectra agreed fairly well with energy distributions of real stars having the same physical parameters. However, when fitting with UV fluxes the disagreement occurred between the model and observed fluxes. This is especially noticeable in the studies done using the earlier version of Kurucz models.([16]) Later Kurucz developed improved version of models with new opacity distribution functions (ODFs), with new atomic and molecular lines and were successful to certain degree in solving the issue of UV fluxes.

The object of this chapter is to determine how the UV flux of A-type stars like blue stragglers or blue horizontal branch stars affect the stellar parameter determination via SED fitting. Here we present our method of multi-band SED fitting based on Bayesian probabilistic inference to determine the stellar atmospheric parameters which uses all the available photometric data for a given object. We test our method for sample of A-type stars (either BHB or BSS) that have good spectroscopic and/or photometric data and well determined stellar parameters.

2.3 Stellar Libraries

In order to study the UV behavior in SEDs of blue horizontal branch and blue straggler stars we require stars that have good spectroscopic data from far UV to near IR. Unfortunately most spectral libraries limited to the optical region of the SED. The lack of libraries extending blueward 3500 Å has prevented the building of models that allow us to perform detailed studies, such as those performed in the optical range.

2.3.1 IUE

This is the fist available stellar UV library ([17]). This contains low resolution spectra for about 218 stars mostly with solar metallicity. The spectra were collected from International Ultraviolet Explorer (IUE) satellite, with wavelength coverage 1300 to 3400 ([18]). The library essentially composed of stars exhibiting normal behavior in the ultraviolet. Even though this is quite a small sample when compare to the size of the modern optical libraries, the difference between the available optical and UV libraries is quite significant. One of the shortcomings of the IUE is that the coverage in metallicity is mostly limited to solar values. According to our estimates only about 30 stars of the library have the metallicities less than -1.

2.3.2 The New Generation Spectral Library

A significant step regarding UV spectral libraries was later made by the New Generation Spectral Library (NGSL) (2009,[19]). The observation were made by the Imaging Spectrograph (STIS) onboard the Hubble Space Telescope (HST). The stellar spectra of the NGSL cover the range 2300-9000 at resolution R $\sim$ 1000. But unlike the IUE, it does not reach the Far UV wavelengths. However the 374 stars of this library were rigorously chosen to have a good coverage in the space of atmospheric parameters. NGSL spectra have a good coverage of stellar atmospheric parameters, with metallic-

ities between -2.0 dex and 0.5 dex and spectral types from O to M for all luminosity classes.

2.4 Data

By analyzing both IUE and NGSL libraries we were able to select 7 stars with well-determined atmospheric parameters. These stars are listed in Table 2.1. From IUE we used only low-resolution, large-aperture spectra. These stars have optical photometry for Johnson B, V, R, and I bands and/or for strgomgren u, b, v, and y bands. In some cases we found accurate multiple flux data for a given source, therefore we use simple averaging in these cases. However, since some optical data are erroneous or inconsistent, we decide not to use in our analysis. None of these stars have data in UV broad-bands like FUV or NUV. Therefore we calculate synthetic magnitudes for these stars using the observed spectra.

Our sample dominated by nearby stars with low E(B-V). Therefore the effect on SED from interstellar reddening is small. This is important in our study because the interstellar reddening affects the blue wavelengths significantly. We dereddened our spectra using the IDL de-reddening routine $CCMUNRED.PRO$ which uses the Fitzparick (1999) parametrization of the Milky Way extinction curves (Cardelli, Clayton 1989, [20]).

2.5 Analysis

2.5.1 Comparison of the Model and the Observed Spectra

Figures 2.2 and 2.3 compare the combined IUE + NGSL spectrum of a star to the best fit model spectrum. The best fit model was chosen based on the stellar parameters available in literature. The model spectra for specific $T_{eff}, log\ gand[Fe/H]$ were obtained by interpolating the Kurucz model grid. For that purpose we used the

spectrum synthesis package, SPECTRUM ([21]). SPECTRUM synthesizes stellar spectra assuming a plane-parallel atmosphere geometry and local thermal equilibrium (LTE) which is consistent with Kurucz ATLAS12 models. we interpolate the Kurucz models using *kmod* IDL package.[1]. *kmod* interpolates linearly a Kurucz model for the desired values of effective temperature, surface gravity and metallicity using 8 surrounding models.

For all the stars in our sample the matching between energy distributions is relatively good. However, some stars show deviation from the model spectrum at FUV wavelengths. For example the stars HD86986, HD2857, HD74721 and HD109995 show larger flux relative to the model spectrum below 2000 $\mathring{A}$. We estimate this difference by taking the average flux in the region below 2000 $\mathring{A}$ for both spectra, and noticed that observed spectra have 10-15 % stronger flux in far-UV. But if we take in to account the estimated errors for these parameters this difference can be easily accounted for.

Based on this investigation we can conclude that the Kurucz ATLAS12 models agree quite well with the observed energy distributions of low-matallicity BHB or BSS stars.

[1]http://www.as.utexas.edu/ hebe/

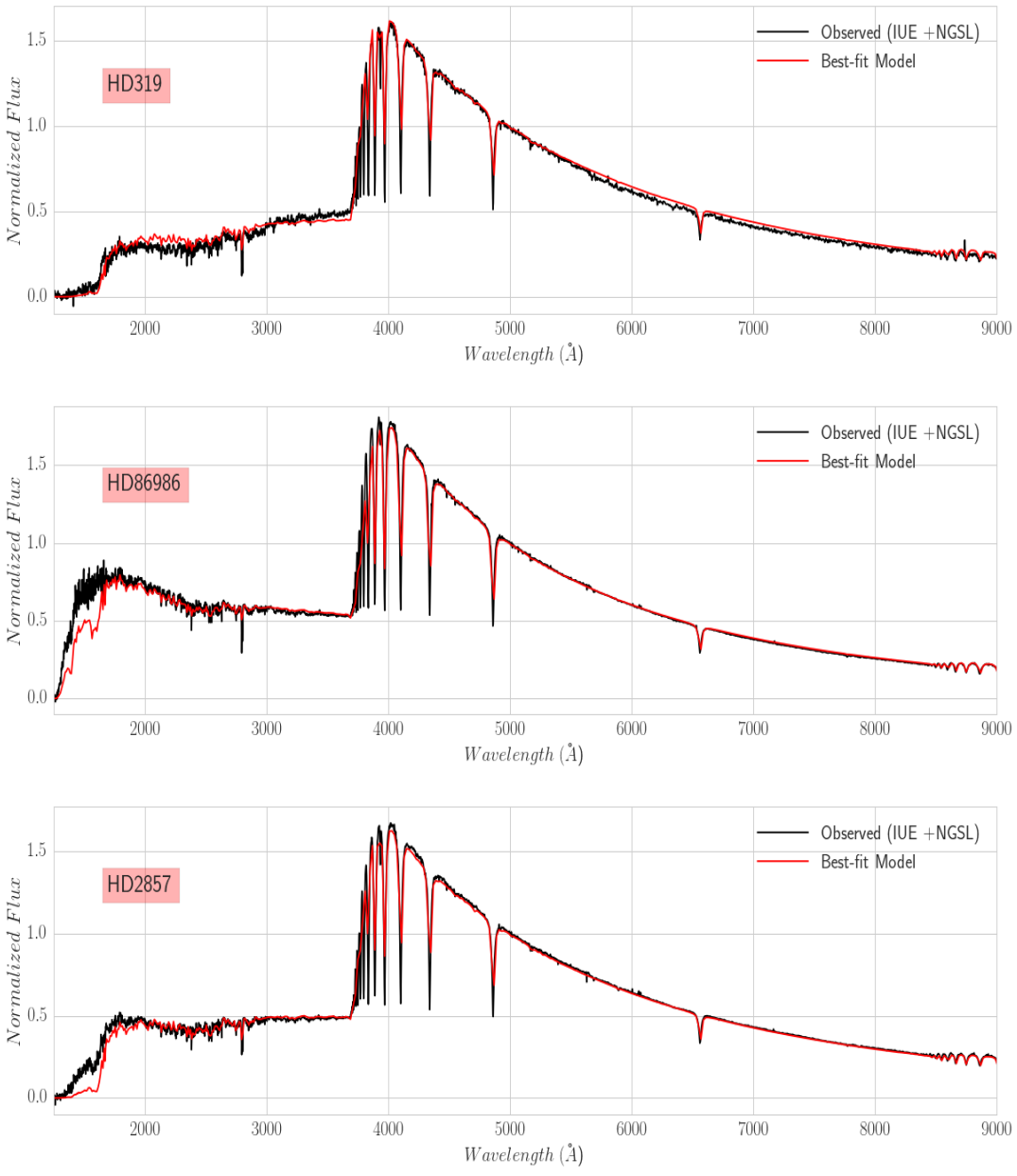

Figure 2.2: Comparison of the observed spectrum with the best fitting model spectrum for stars in our study.

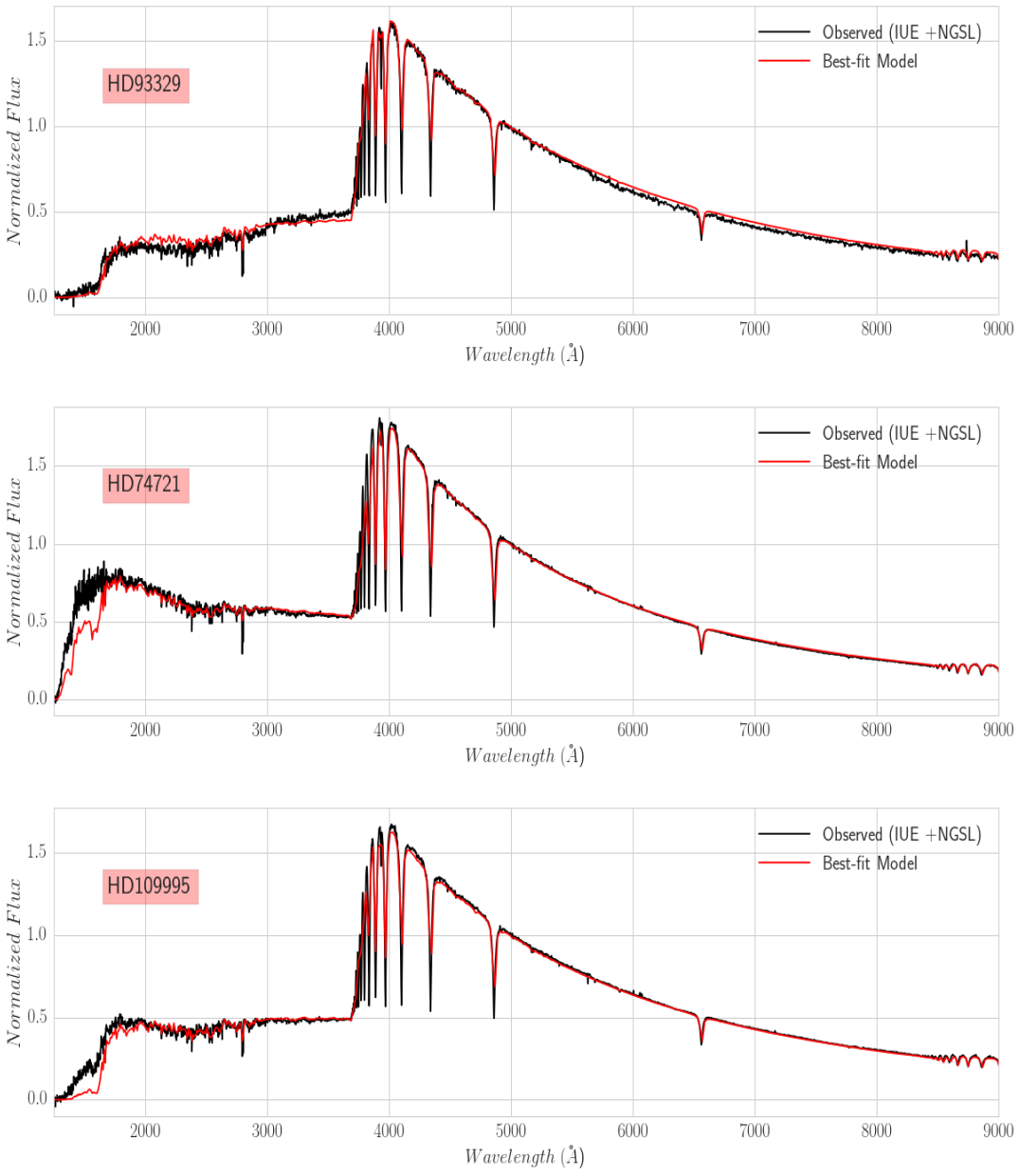

Figure 2.3: Comparison of the observed spectrum with the best fitting model spectrum for stars in our study.

2.5.2 Constructing SED

We used grids of model spectra calculated by Kurucz(2004) in this study. We calculate synthetic magnitudes based on these spectra for various bands including Johnson U, B, V, R, I stromgren u, v, b, y and GALEX FUV and NUV.

The standard formula to calculate the synthetic magnitude for particular bandpass is,

$$m = -2.5\ log(\frac{\int_{\lambda_i}^{\lambda_f} \lambda f_\lambda S_\lambda d\lambda}{\int_{\lambda_i}^{\lambda_f} \lambda S_\lambda d\lambda}) + ZP \tag{2.1}$$

where f_λ is the flux calculated at the surface of the star, and S_λ is the response function for a given passband and integration limits represent the wavelength interval for a given passband. Response functions for the different passbands are shown in Figure 2.4.

As mentioned above all of the stars in our sample have accurate optical photometry in several bands. For the UV part of the SED we calculated the FUV and NUV magnitudes using the combined NGSL and IUE spectra.

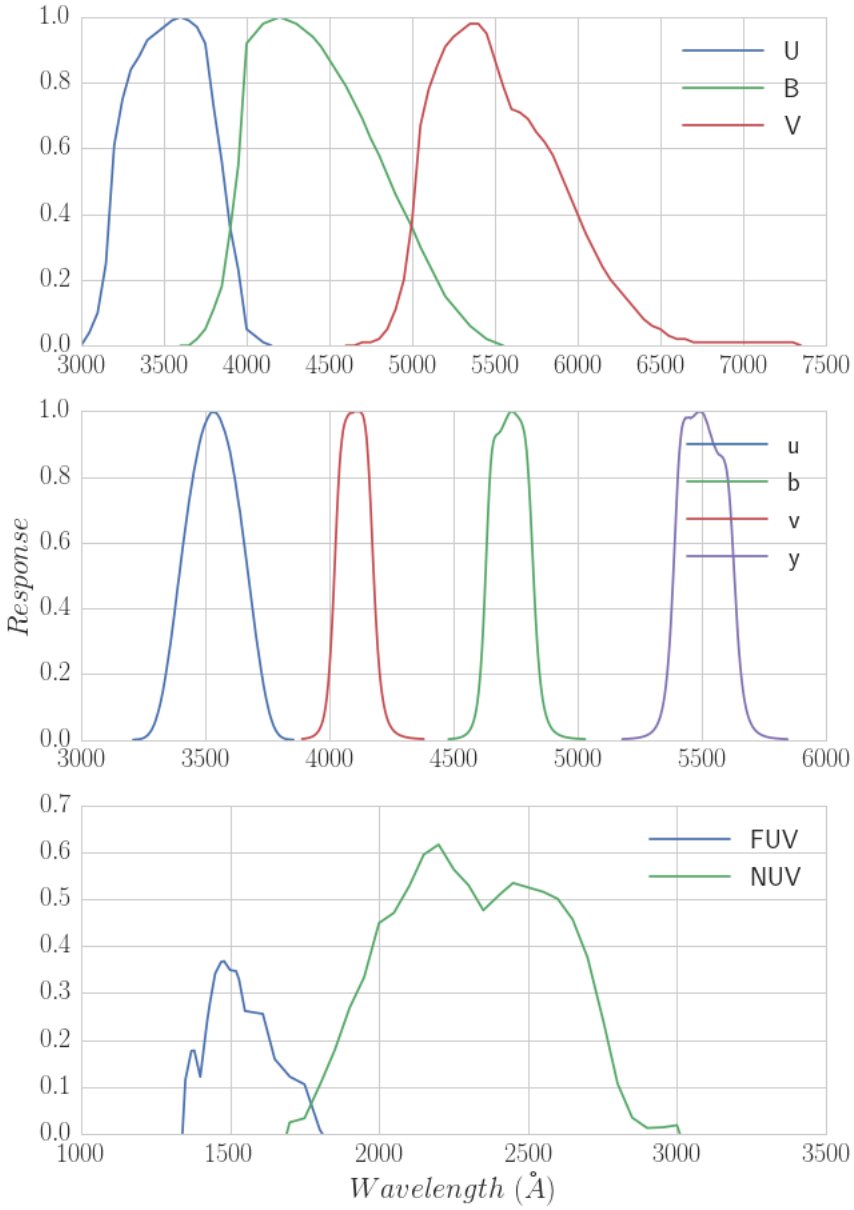

Figure 2.4: Passband response functions from which synthetic magnitudes have been computed. All curves are normalized to one, and as shown as function of wavelength.

2.5.3 Bayesian Inference

There are many different codes available for SED fitting and most of them considers the best-fit model parameters. This method can cause problems when the observational data covers a large wavelength ranges. Moreover, the errors associated with the best-fit measurements can be physically meaningless sometimes.

In this study therefore we decided to use the Bayesian approach, for measuring the goodness of fit between the observed and model data while incorporating the statistical measurement errors. The key idea here is to obtain a full probability distribution for a given parameter. The knowledge of the full distribution allows to estimate meaningful confidence intervals for a given parameter. In addition a full distribution can be reduced to a point estimate by computing the expectation value, mode or standard deviation whenever necessary for tabulating or visualizing purposes.

In Bayesian statistics, the posterior probability distribution $p(\theta/D)$ of the true value of the model parameters θ given the observations D is proportional to the product of likelihood function $p(D/\theta)$ and prior $p(\theta)$,

$$p(\theta/D) \propto p(D/\theta)p(\theta) \tag{2.2}$$

Here $p(\theta)$ encodes any a priori knowledge about the parameters which we wish to include in our model. It reflects our knowledge of the distribution of the parameters in the absence of the observations D.

When we don't have any prior information we can use a flat (or uniform) prior for all of our parameters. Then we compute the likelihood of observing SED by assuming normally distributed uncertainties on the observed magnitudes, such that the likelihood function is given by,

$$p(\theta/D) \propto p(D/\theta) = exp(-\chi^2_{red}) \tag{2.3}$$

where,

$$\chi^2 = \sum_i \frac{(f_{obs} - f_{model})^2}{\sigma_i^2} \tag{2.4}$$

where i denotes the ith band and the sum is performed over all observed photometric bands of the star being fitted. The reduced chi-square, χ^2_{red} as defined by χ^2/k, where k is the degree of freedom: $k = n - m$. Here n is the number of photometric measurements and m is the number of free parameters in the model.

Taking the probability $P_i = P(\theta/D)$ as weights for each model, the expectation value for a give parameter can be calculated.

$$\hat{x} = \frac{\sum_i P_i x_i}{\sum_i P_i} \tag{2.5}$$

Also, the standard deviation,

$$\sigma_x = \sqrt{\frac{\sum_i P_i (x_i - \hat{x})^2}{\sum_i P_i}} \tag{2.6}$$

2.5.4 SED Fitting Results

We computed the posterior probability density for the stars in our sample and examples of them are shown in Figure 2.5.

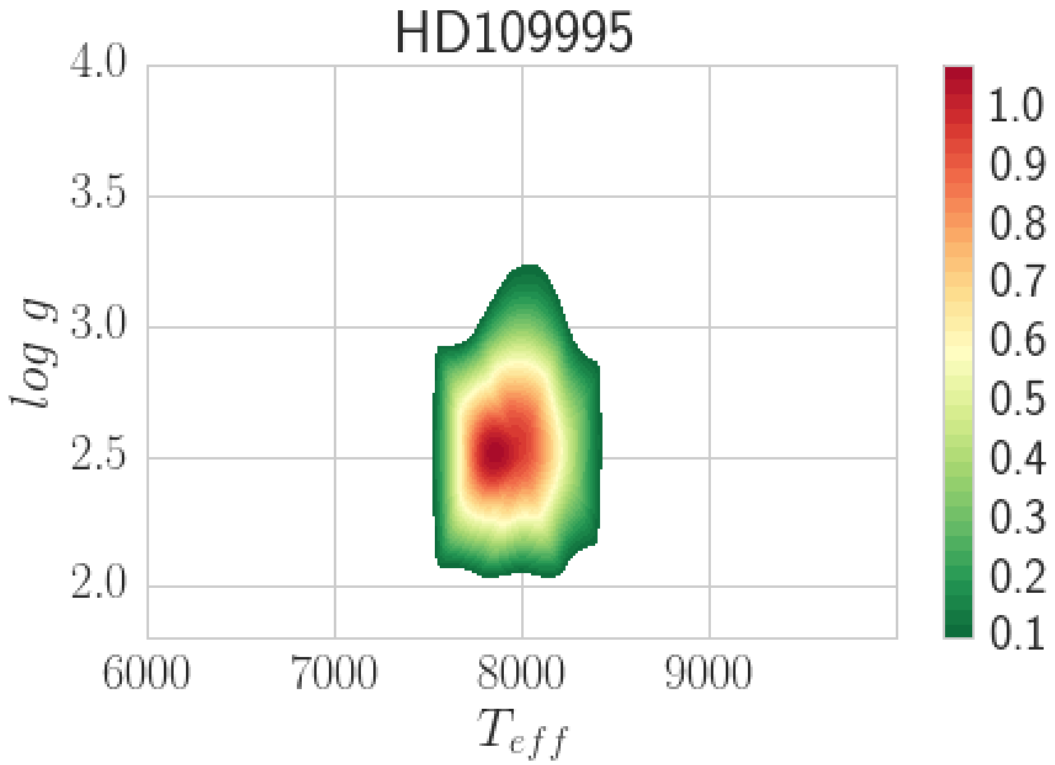

Figure 2.5: Example posterior joint distribution between T_{eff} and $log\ g$ for a star in our study. Color bar on right of plot represent the probability.

The whole sample follows the same pattern, where the posterior for $log\ g$ and $[Fe/H]$ is typically broad, while that of T_{eff} is relatively tighter.

The final expectation values and standard deviations calculated from these distributions are shown in Table 2.1.

Object	T_{eff} (K)	$log\ g$ (dex)	$[Fe/H]$ (dex)
HD2857	7450/7560	2.6/2.9	-1.6/-1.1
HD74721	8640/8500	3.55/3.3	-1.48/-1.2
HD86986	7850/7790	3.1/3.0	-1.5/-1.2
HD10995	8000/7900	3.5/3.2	-1.7/-1.2
HD93329	8127/8200	2.8/3.1	-1.2/-0.9
HD319	8140/8090	4.3/3.7	-0.7/-0.9
HD60778	8100/8130	2.7/3.	-1.4/-1.1

Table 2.1: Stellar parameters obtained from SED fitting compares to published values (column format is published/SED fitting)

As shown in the Table 2.1 , our temperature values agree quite well with the high resolution spectroscopic measurements. The $log\ g$ and $[Fe/H]$ values are not as accurate as T_{eff} values, and has average scatter about 0.3 dex compare to the published values. But the broader probability distribution in these parameters causes significantly larger errors in $log\ g$ and $[Fe/H]$. Typical errors are 150 K for temperature and 0.6 dex for $log\ g$ and $[Fe/H]$.

2.6 Summary

In this section, we evaluate the consistency between observed energy distribution of metal-poor A-type stars and that of Kurucz(ATLAS12) models, especially focusing on the UV wavelengths. We noticed that the observed and model energy distributions agreed quite well overall, with slight deviation at far-UV wavelengths. We have estimated that the model fluxes below 2000 Å predict less flux than the observed flux.

In addition we measured the stellar parameters for these stars following a Bayesian-like probability SED fitting procedure. The purpose of this method was to use the all available flux data from UV to IR, while considering the statistical significance of the full model parameter space. The method successfully predict the temperature values but there is significant scatter in surface gravity and metalicity measurements. This

suggests that the method is not very successful in breaking the degeneracy between parameters. However, we emphasize the most useful aspect of the Bayesian inference is the ability to incorporate pre-known information (prior) to the calculations. In our method we treated all the parameters with equal probability (flat priors). By using appropriate priors for the parameters can in principle break the degeneracies between parameters and give more accurate estimates.

Chapter 3 Blue Straggler Stars in the Galactic Field

3.1 Introduction

3.1.1 Blue Straggler Stars

Blue Straggler stars were first discovered in a photometric study of globular cluster M3 by Sandage in 1953. [22]. They are identified by there position in color magnitude diagram, in which they appear along the extension of the main sequence but more bluer and brighter than the main sequence turn-off and apparently younger than the most of the stellar population. The BSS sequence is a typical feature of most of the globular clusters.(Figure 2.1) Moreover, since Sandages discovery blue stragglers have been observed in many stellar environments,like , open clusters [23] , globular clusters [24], dwarf spheroidal galaxies [25] and galactic field.[26]

Interestingly, the single stellar evolutionary theory failed at explaining the existence of BSS sequence in CMD of steller populations. Even though exact mechanism of the formation of blue stragglers is not fully understood there are two theories popular among astronomers . Both theories rely on the basic idea that BSS are formed by adding mass to a main sequence star in a binary or multiple stellar system via some mechanism.

(1) Merger between stellar systems

This could happen in many scenarios: merger of a contact binary, merger during a dynamical encounter and a merger of an inner binary in hierarchical triple system. Direct stellar collision will result in a slower rotating BSS. Binary coalescence, however, will result in a faster rotating object (if the pair is of similar mass).

(2) Mass transfer between two stars in a binary system.

This is the case where the more massive star in a binary system transfers material,

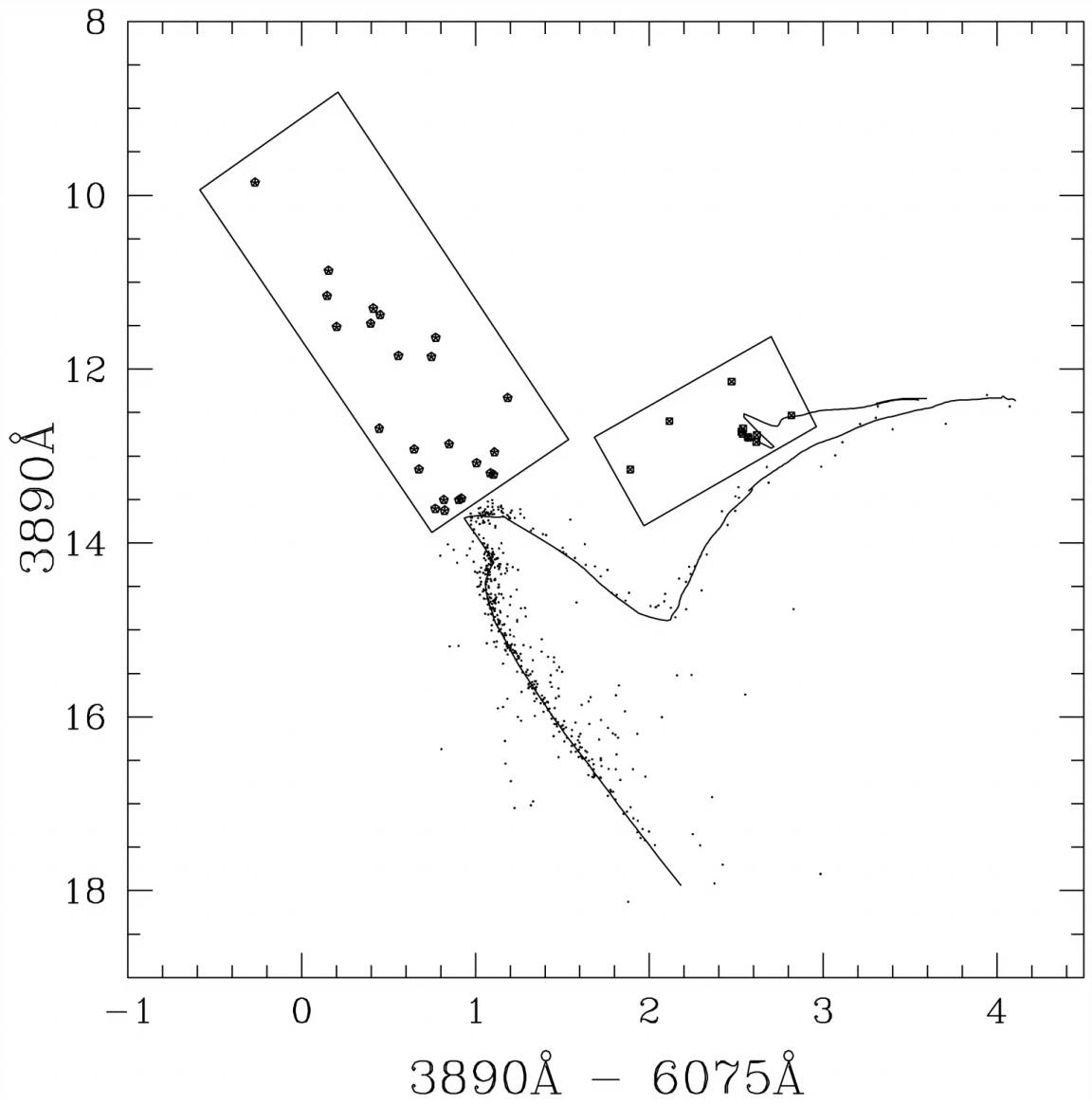

Figure 3.1: Observed CMD for M67. The axes are the color and magnitude labeled with the central wavelengths. The pentagonal points are the blue stragglers more luminous than the main-sequence turnoff, the squares the intermediate-color stragglers and clump giants, including one possible AGB star.Adopted from [27]

during its post main-sequence phase,to its companion star. If the mass transfer is stable, this may add sufficient mass to the secondary to convert it into a blue straggler. This appears to be the main formation channel for BSS.

By comparison, BSS formation via the mechanisms involving single stars were

either discredited or believed to be much rarer. Some of the interesting ideas related to single star BSSs are : delayed or late star evolution, extended main sequence lifetimes due to large scale mixing [28] , highly evolved stars that happened to land close to the normal main sequence and tidal capturing of young Galactic field stars.

3.1.2 Mass Transfer via Roche-Lobe Overflow

The Roche lobe is the region around a star in a binary system within which orbiting material is gravitationally bound to that star. It is an approximately circular-shaped region bounded by a critical gravitational equipotential, with the apex of the tear drop pointing towards the other star (the apex is at the L1 Lagrangian point of the system). When the radius of a star in a binary system becomes larger than its Roche-Lobe, it will transfer mass to its companion star as shown Figure 3.2. This mechanism is called Roche lobe overflow (RLOF). It was one of the first models suggested for the origin of BSS [29].

In a cluster of stars , when the accretor is a main sequence star and accrete enough material to increase its mass above that of the cluster turnoff, a blue straggler is formed.

The product of binary mass transfer depends on several characteristics of the system:

1. the evolutionary status of the donor : this implies its complete internal structure
2. the structure of the donor envelope
3. the mass ratio of the binary
4. the type of the accretor

The nature of all these properties are responsible for the stability of the mass transfer and for its final product.

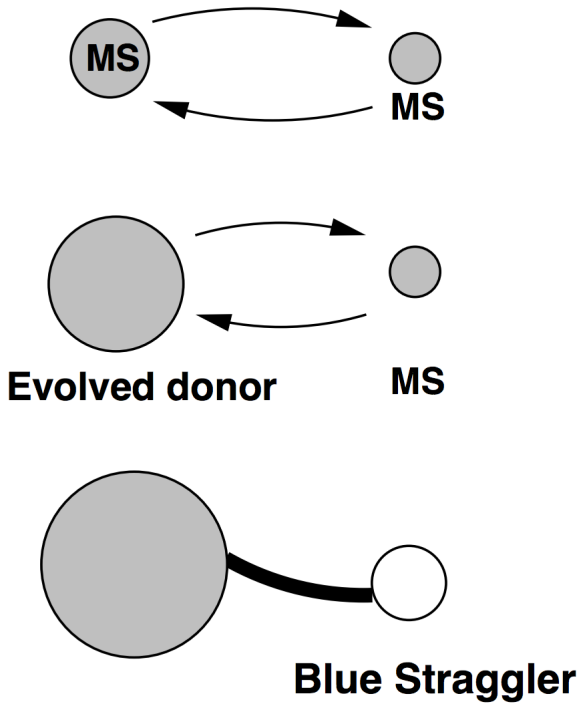

Figure 3.2: The evolutionary pathway to produce blue straggler stars (BSSs) through mass transfer. First the bigger primary evolves off the main sequence and fills its Roche lobe. Then secondary gains mass from the primary becoming a BSS

Generally the mass transfer binaries are classified on the basis of what state of evolution the donor is in ([30])

Case A: during hydrogen burning in the core of the donor.This can happen if the orbital separation of the binary is small (usually a few days).

Case B: after exhaustion of hydrogen in the center of the donor (red giant phase). In this case orbital period is less than about 100 days, but longer than a few days.

Case C: after exhaustion of central helium (He) burning (AGB phase). Here the orbital period is above 100 days.

It is believed that Case A mass transfer is more likely to be result in the coelescense of the two stars.(for example [31]) In that sense it can be treated as one of the merger scenarios. According to the binary evolution simulations ([31] etc.), in order to produce a BSS via Case B and Case C, the mass transfer has to stable. During stable

mass transfer the donor stays within its Roche-lobe. Therefore the stability of the mass transfer depends on donors response to the mass loss and on how conservative the process is and what are angular momentum loss processes in this binary.

Given stable mass transfer, case B mass transfer leaves a He white dwarf companion bound to the blue straggler, while Case C mass transfer leaves a CO white dwarf companion.

3.1.3 Field Blue Straggler Stars

For given stellar population the dominant formation channel of BSSs depends on its environment. The BSS in galactic field, where the stellar number density is much lower than globular clusters, were formed primary due to mass transfer [26]. High resolution study of Field BSS done by Preston an Sneden [26] suggested that 60 % their sample were binaries. Moreover they concluded that the great majority of field BSSs probably created by Roche-lobe overflow during red giant branch evolution (Case B). Ryan et. al. ([32])studied lithium deficiency and rotation of the BSS and came to the conclusion that these stars can be regard as mass transfer binaries.

The origin of BSS in the Galactic field is related to the formation of the Galactic halo as well. In addition to the idea of in situ origin, Preston ([33]) argued that modest fraction of BSS could be a stellar population belong to an accreted Galactic satellites similar to Carina dSph.

While we have an overall understanding of how blue stragglers could be formed via different mass transfer mechanisms, stellar evolution theory is far from predicting the exact nature and the frequencies. To test the theory with observations, it is vital to identify the clean sample of mass transfer candidates. Since blue stragglers in globular clusters are contaminated by those formed via collisions, blue stragglers in a field are the best candidates for a clean sample of mass-transfer BSS.

As mentioned in the last section the mass-transfer process result in BSS with a

white dwarf companion. BSS are much brighter than WDs at optical wavelengths so ,such binaries are hard to find. But if the WD companions to BSS are young and hot, they can be detected at ultraviolet wavelengths. This opens the possibility to detect the mass transfer formation of BSS.

3.1.4 White Dwarf Stars

White dwarfs are the end product of stellar evolution for the low-intermediate mass main sequence stars. In fact, more than 95 % of all stars are expected to end their lives as white dwarfs. In white dwarfs gravitational collapse in prevented by the pressure of degenerate electrons, rather than the thermo-nuclear reactions. One of the key features of white dwarfs is the cooling sequence, i.e. white dwarfs decrease their luminosity as they age.

Based on the composition of the thin atmosphere, white dwarfs classified into several types. White dwarfs that have hydrogen dominated atmospheres are called DA white dwarfs, while white dwarfs have helium dominated atmospheres are called DB. DA white dwarfs are the most common type. There gravity is so strong such that all the heavy elements are sinked down below the visible layers. This will create a thin pure hydrogen atmosphere in the white dwarf. In hot (young) white dwarfs this sedimentation process happens happens very quickly because the diffusion time scales are only of the order of days. In the case of DB white dwarfs (pure He atmospheres), the outer H layer has been completely lost, and He as the next lightest element floats up to the top.

A small number of white dwarfs (less than 10 % of total WD observed) are composed of different elements in their atmospheres, such as C (DQ) and other heavy elements (DZ). Hot white dwarf atmospheres composed of ionized He are called DO, and cool stars which show no identifiable features are labelled as DC.

Pre-white dwarf atmospheres are mainly composed of He and/or a mixture of C,

N and O, or H depending on the previous evolution from the MS. The H-rich stars remain their whole lives as DA. He- and CNO-rich stars initiate their life as hot DO and the diffusion of heavy elements is supposed to leave behind a surface of H as they cool. Below Teff $<$ 10000 K, the chemical evolution of the WD becomes more complicated and is not fully understood.

This chapter focuses on the detecting the mass transfer field BSSs from the SDSS survey and use them to characterize the formation histories.

3.2 Analysis

3.2.1 Identification of Field Blue Straggler Stars

The stellar population in Galactic field is different from the other two principal Galactic populations, thick and thin discs. While the stars in the halo field are old and metal poor the stars in discs are young and metal rich. But separation of these populations is not easy because the distributions overlap.

Over the years many photometric studies have been done to identify field BSS, primarily using color-color plots. For example Yanni et. al ([34]) identified 2700 field BSSs using SDSS photometry . Sirko et. al used SDSS photometry in combination with spectroscopy to identify field BSSs ([35]).

The data used for this study were taken from the Sloan Digital Sky Survey Data Release 12 (SDSS DR12) and Galaxy Evolution Explorer (GALEX) GR5, an ultraviolet survey.

3.2.2 SDSS Data

SDSS is an optical photometric and spectroscopic survey that obtains its data from a 2.5 m telescope in Apache observatory in New Mexico. SDSS DR12 offers the latest data from SDSS project 3. It provides photometry in 5 bands (u, g, r, i and z) for 400 million objects spanning a magnitude range 15-22 and covering 11500 deg^2,

approximately quarter of the celestial sphere. The detection limit for point sources with 1 arcsecs seeing is 22.3, 23.3, 23.1, 22.3 and 20.8 magnitudes on the AB system respectively, at an air mass of 1.4. Also DR12 includes low resolution spectroscopy with resolution R $\tilde{1}800$ and wavelength coverage 3800-9200A, for about 2 million objects.

Using the SDSS photometry field BSSs can be identified using the u-g vs g-r color-color plot using the following color cuts.(Figure 3.3)

$$0.60 < (u - g) < 1.60 \tag{3.1}$$

$$-0.20 < (g - r) < 0.05 \tag{3.2}$$

This area in the color-color diagram is populated by A-type stars including high gravity BSS and low gravity BHB stars. Therefore, in order to separate the BSS from BHB stars one would need stellar parameters for individual stars. For that purpose we employed the current version of the Extension for Galactic Understanding and Exploration (SEGUE) Stellar Parameter Pipeline (SSPP) [37].

SSPP uses 8 primary methods for the estimation of effective temperature, T_{eff}, 10 for the estimation of $logg$ and 12 for the estimation of $[Fe/H]$. Typical errors for the SSPP measurements are, $\sigma(T_{eff}) = 200K$, $\sigma(logg) = 0.4dex$, and $\sigma([Fe/H]) = 0.3\ dex$ (These evaluations are for the stars that have spectra signal to noise ratio ($S/N = 25$), so these errors increase as the S/N decreases.)

The stars selected via the initial color cut using equation 3.1 and 3.2 were plotted in $T_{eff} - log\ g$ plane as shown in Figure 3.4. The two sequences of low gravity BHB and high gravity BSS are clearly visible in the $logg$ vs T_{eff} diagram. We select only the BSSs above 7000 K to avoid contamination of other F,G type main sequence stars and/or variable RR lyrae stars.

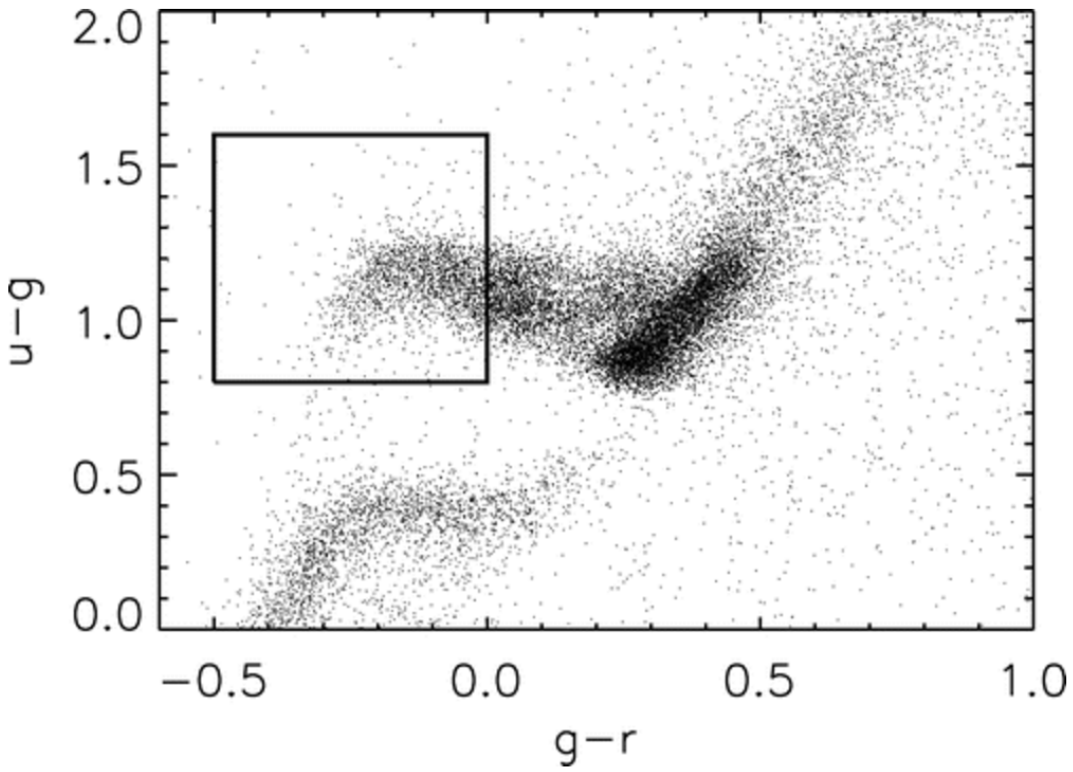

Figure 3.3: The color selection in u-g and g-r used to select BHB and BS stars. Adopted from Xue et.al. [36]

3.2.3 GALEX Data

The Galaxy Evolution Explorer (GALEX) was a NASA Small Explorer mission [1], all-sky ultraviolet survey conducted from 2003-2013. It was performed in two ultraviolet(UV) bands Far-UV(FUV) and Near-UV(NUV). (Figure 3.5) The effective wavelengths are 1516 and 2267 angstroms for FUV and NUV bands respectively. It consists of 0.5 m diameter modified Ritchey-Cheretien telescope which has a wide 1.25 degree filed of view and simultaneous imaging coverage in the FUV and NUV. The image resolution of the instrument is 4.2" in the FUV band and 5.3" in the NUV band. With pixels 1.5", this translates to FWHM of approximately 2. pixels in the

[1] See http://www.galex.caltech.edu for more information.

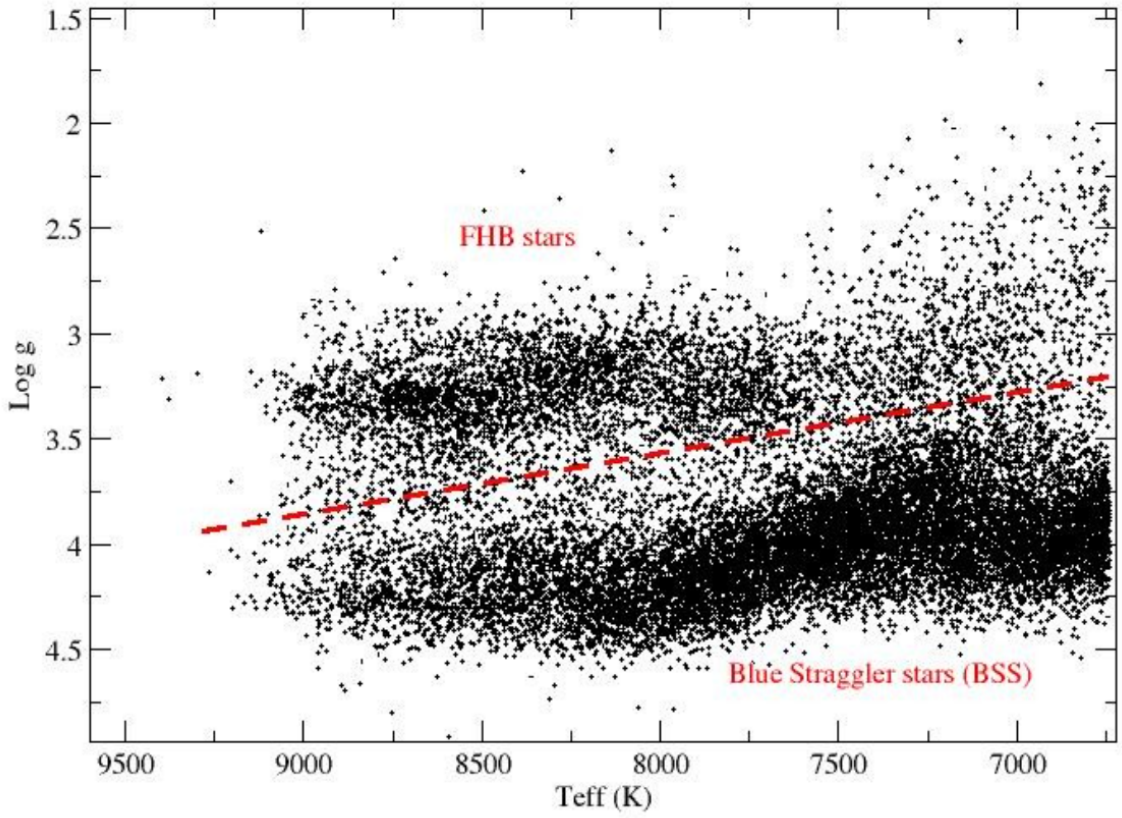

Figure 3.4: BSS-BHB separation in SDSS data using the stellar parameters

FUV and 3.5 pixels in the NUV.

The main survey of the mission is the All-sky Imaging Survey (AIS), which covers about 3/4 of the sky and has depth up to $m(AB)21$. During each observation period, an average of 10 different fields (10 deg^2) are observed, with a typical exposure time of 100 s and several hundred to 1000 objects observed per field. The AIS was designed to complement other large surveys, primarily SDSS, and comprises the vast majority of the data products produced by the mission.

The other GALEX surveys are deeper, but restricted to smaller fractions of the observable sky. Medium Imaging Survey (MIS) exposures are a single orbit, typically 1500 s, and cover a total observed area of 1000 deg^2 with sensitivity mAB up to 23. The Deep Imaging Survey (DIS) consists of 20 orbit exposures (mAB 25) over 80

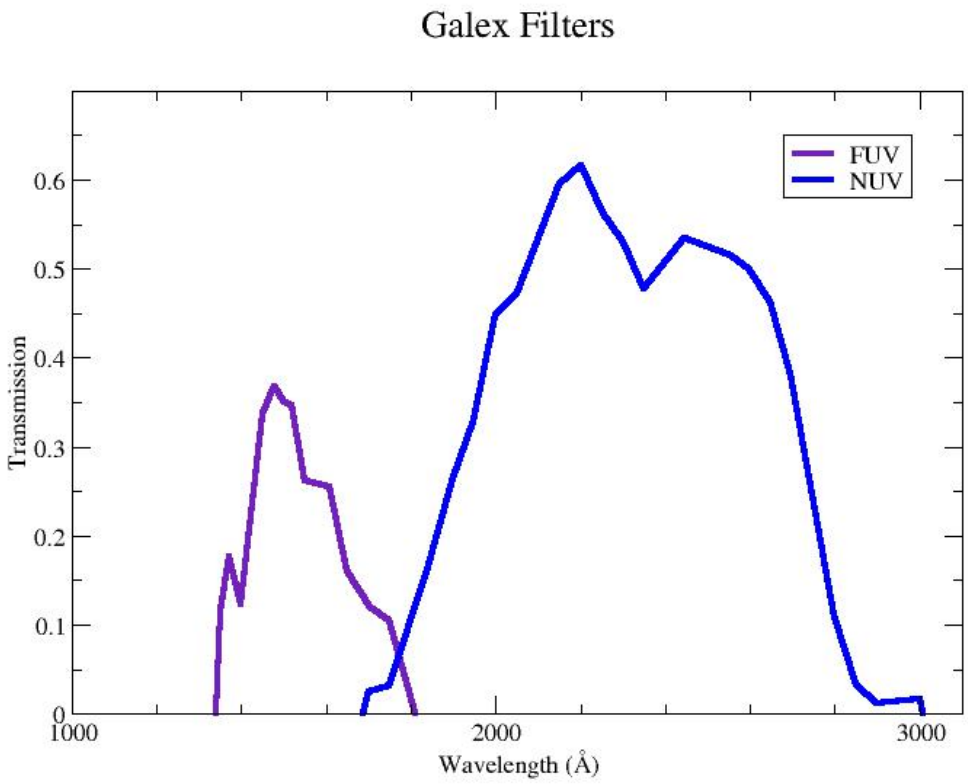

Figure 3.5: Transmission curves for GALEX bandpasses

deg^2 and is designed to overlap with existing multiwavelength coverage.

3.2.4 Cross-Identification of sources

Most GALEX observations are designed to cover regions of the sky already observed by the SDSS at a comparable depth (Figure 3.6).

In order to construct spectral energy distributions(SED) from UV to IR requires to linking SDSS sources to GALEX counterparts. The matching was done online using the CDS X-Match Service [2], adopting a match radius of 5" . Such a match highly depends on the positional accuracy and resolution of both surveys. Because the GALEX images have lower angular resolution, we tallied instances of multiple

[2]http://cdsxmatch.u-strasbg.fr/xmatch

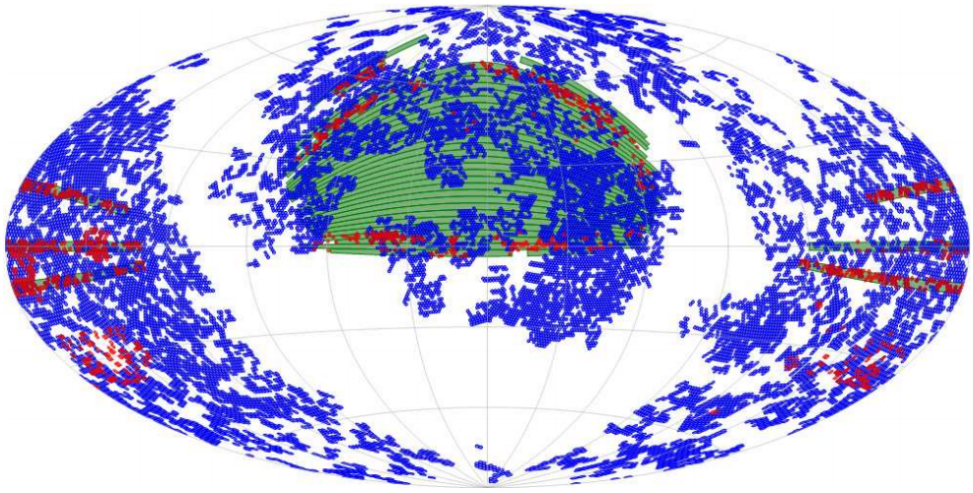

Figure 3.6: Footprints of the SDSS (green), GALEX AIS (blue) and MIS (red) imaging surveys [38]

matches (more than one potential optical counterpart per UV source). UV sources with multiple optical matches inside the match radius must be treated with caution, since the UV flux may be the composite of multiple stars. These are about 10% of our total sample. The GALEX and optical positions of matched sources are within 2 arcseconds in the vast majority ($> 90\%$) of cases, indicating consistency in the astrometry and robust matching between the two catalogs. We restricted matches that were closest-neighbor members of one survey to the other and vice versa.

Our final sample includes 2188 stars. Their GALEX and SDSS photometry are given in Appendix 1 . The distribution of stellar parameters for these stars are shown in Figure 3.7.

3.2.5 Extinction Correction

SDSS data were corrected for interstellar extinction using the extinction relations given in Schafley(1998)([39]) while FUV and NUV were corrected for extinction using the relations given Rey. et. al.(2007)([40]). The $E(B-V)$ were taken from Schelegal et al.(1998)([41]). The extinction coefficients for each band are listed in Table 3.1.

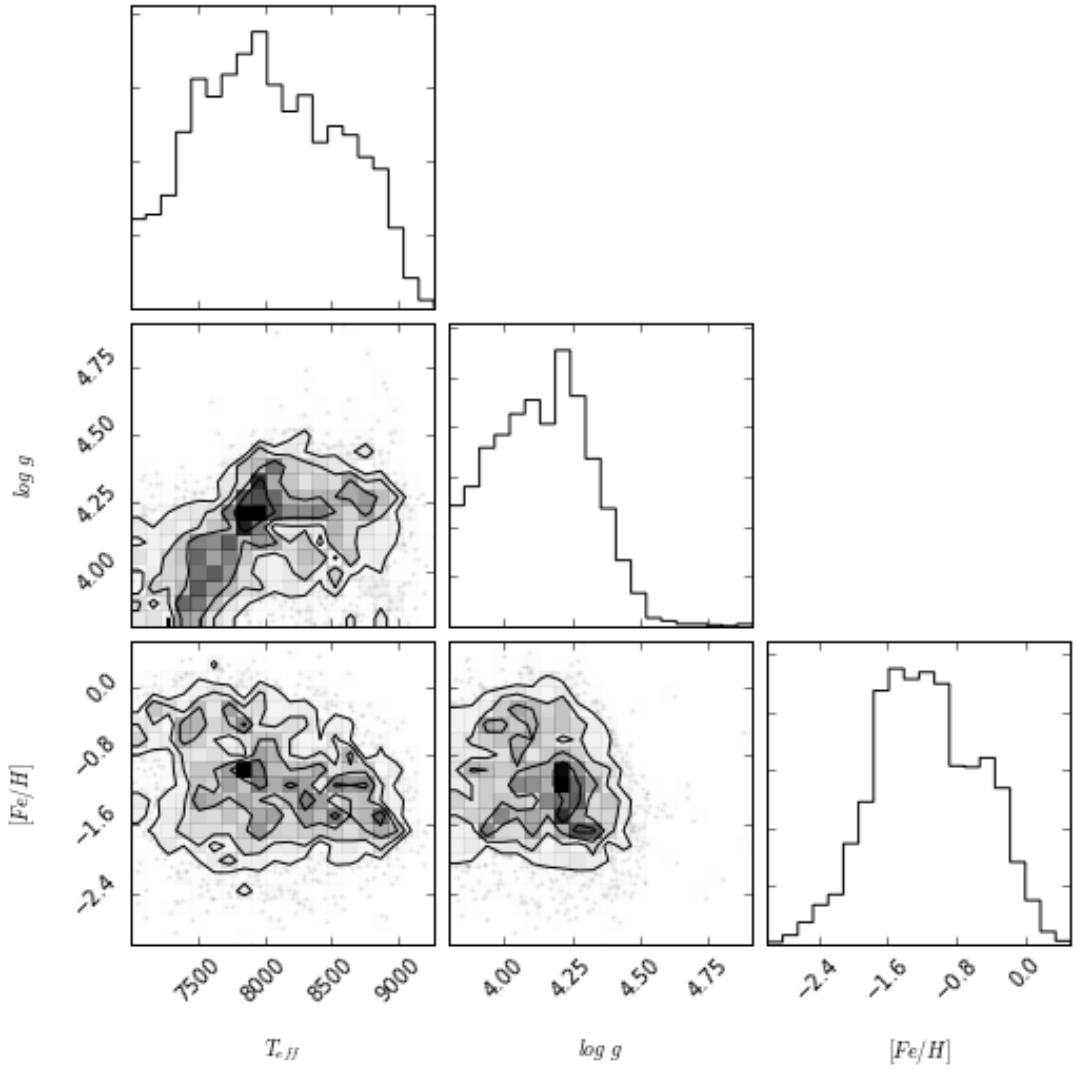

Figure 3.7: Stellar parameter distributions for filed BSSs selected in this study

3.2.6 UV-Excess Stars

The optical CMDs are usually dominated by the cool stars so that the characterization BSSs or other hot stars like extreme blue horizontal branch or the binary star products is difficult. In addition BSSs can be easily mimicked by photometric blends of sub-giant branch (SGB) and red giant branch (RGB) stars in the optical CMD. Therefore UV colors must be used to identify the special features of the BSSs.

Bandpass	A/E(B-V)
FUV	8.16
NUV	8.9
u	4.239
g	3.303
r	2.285
i	1.698
z	1.263

Table 3.1: Extinction in different passbands

Identification of UV-excess stars based on their position in FUV/optical color-color plot is one useful application of UV photometry. Using GALEX and SDSS colors together have enabled the discovery of white dwarf-main sequence (WDMS) binary systems, i.e., binaries with WD primaries and late-type main-sequence secondaries ([42])

Smith, Myron A et al([43]) adopted a similar approach to identify the FGK-type stars with excess UV in their spectral energy distribution. They used combined data from GALEX satellite's far-UV (FUV) and near-UV (NUV) bandbasses as well as from the ground-based SDSS survey and the Kepler Input Catalog to identify stars that exhibit FUV-excesses relative to their NUV fluxes and spectral types. They considered the these UV excesses originate from various types of hot stars, including white dwarf DA and sdB stars, binaries, and strong chromosphere stars that are young or in active binaries.They calibrate the UV-excess stars using their distribution in (FUV - NUV) - T_{eff} plane (Figure 3.8).

In this study we identify UV-excess BSSs using a similar approach.

3.2.7 Temperature Sanity Check

Our method for selecting UV excess BSSs depend on the temperature of the stars. Rahther than using SSPP values directly, as a sanity check we remeasured the tem-

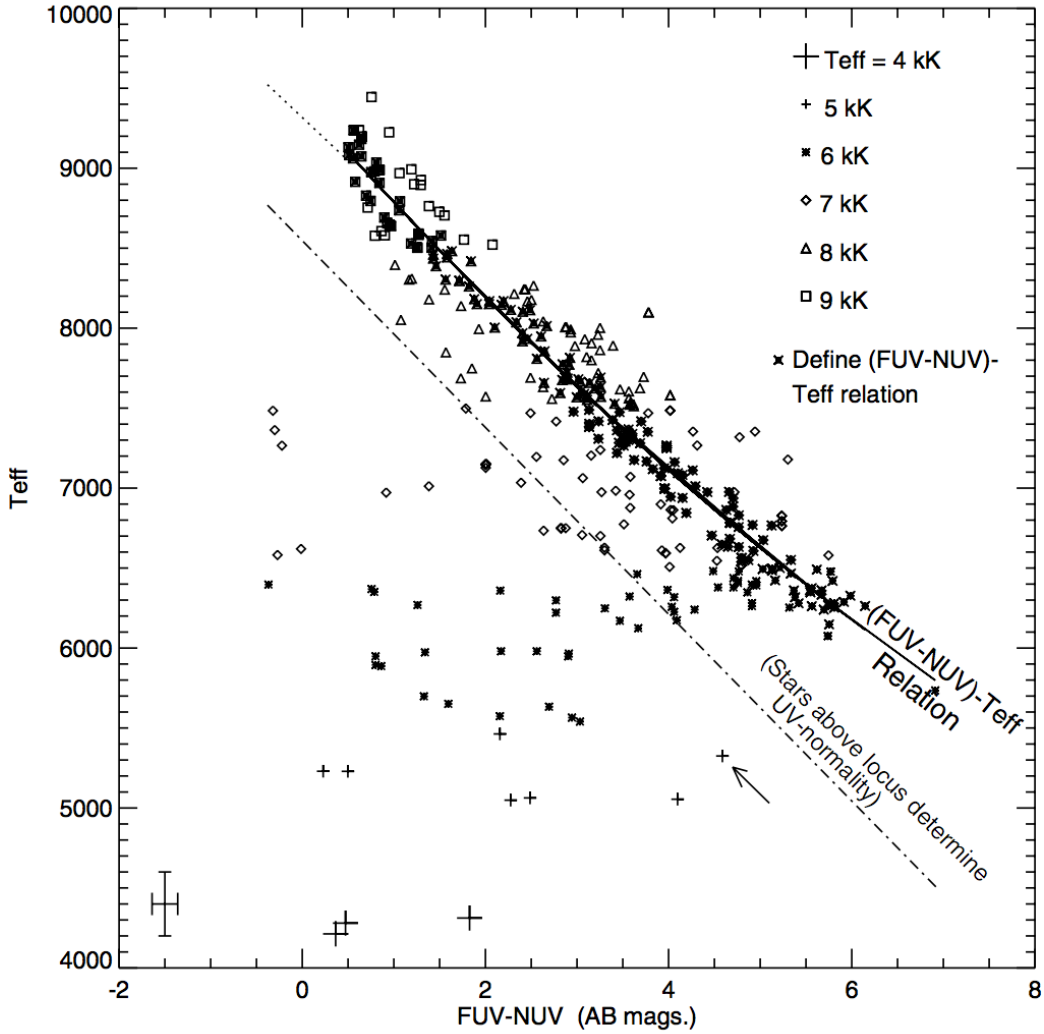

Figure 3.8: (FUV-NUV) vs. SDSS/DR7 Teff values from GALEX-SDSS data. Symbols denote 1 kK bins in Teff. Solid symbols denote the stars used to define the upper (FUV-NUV) - Teff diagonal sequence and calibrate this color from their Teff values. The dot-dashed locus separates the calibration sequence from the UV-excess population in the lower left. [43]

peratures for our sample by fitting of the Hydrogen balmer lines of the SDSS spectrum to model spectrum. For that purpose we created the synthetic spectra using SPECTRUM package ([21]). SPECTRUM synthesizes stellar spectra assuming a plane-parallel atmosphere geometry and local thermal equilibrium (LTE).

We adopted Kurucz ATLAS12 atmosphere models.[3] In order to achieve a more dense grid of spectra we interpolate the Kurucz models using kmod IDL package.[4]. kmod interpolates linearly a Kurucz model for the desired values of effective temperature, surface gravity and metallicity using 8 surrounding models. Our final grid consists of spectra with the temperatures in the range 6500 - 10,000 K in steps of 125 K.

The final temperatures were estimated using the Bayesian formalism describe in section 2.3. Note here we fit the spectral absorption line, rather than photometric point, therefore our degree of freedom is equal to the number of pixels in a given line(or the number of wavelength data points). Since we used $H-\alpha$ and $H-\beta$ lines in our fitting, we we multiply the individual likelihood to get the final posterior probability. Finally the point estimates of mean and error in temperatures were calculated.The mean error obtained for temperatures is 140 K.

We compared the temperatures obtained from our method to those obtained from the SSPP in order to check the consistency (Figure 10). Both SSPP and our method predicts consistent values for majority of the stars. Given the uncertainties in our measurements we continue our analysis with the all the stars except the ones with T_{eff} difference larger than 250 K. For the rest of the analysis we consider only the SSPP values.

[3]Kurucz models are available at http:kurucz.harvard.edu
[4]http://www.as.utexas.edu/ hebe/

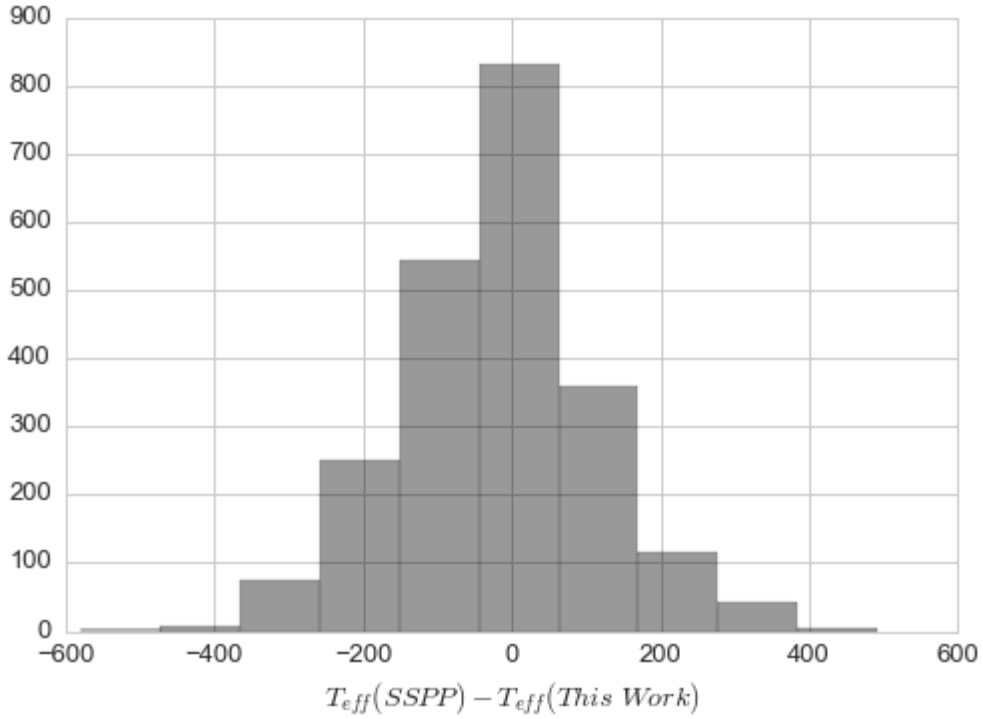

Figure 3.9: Comparison of temperatures of BSSs in this work with SSPP

We plotted Teff values determined from the SSPP vs $FUV - NUV$ color of the stars in our sample (Figure 3.10). The diagonal sequence in the Figure 3.10 reflects the relationship between SDSS T_{eff} and $FUV - NUV$ for the main-sequence stars. We fit the main diagonal sequence with a quadratic fit and the stars lying outside the 2σ from the best fit were selected as UV-excess BSS stars. These are our candidates for the BSS with a hot WD companion.

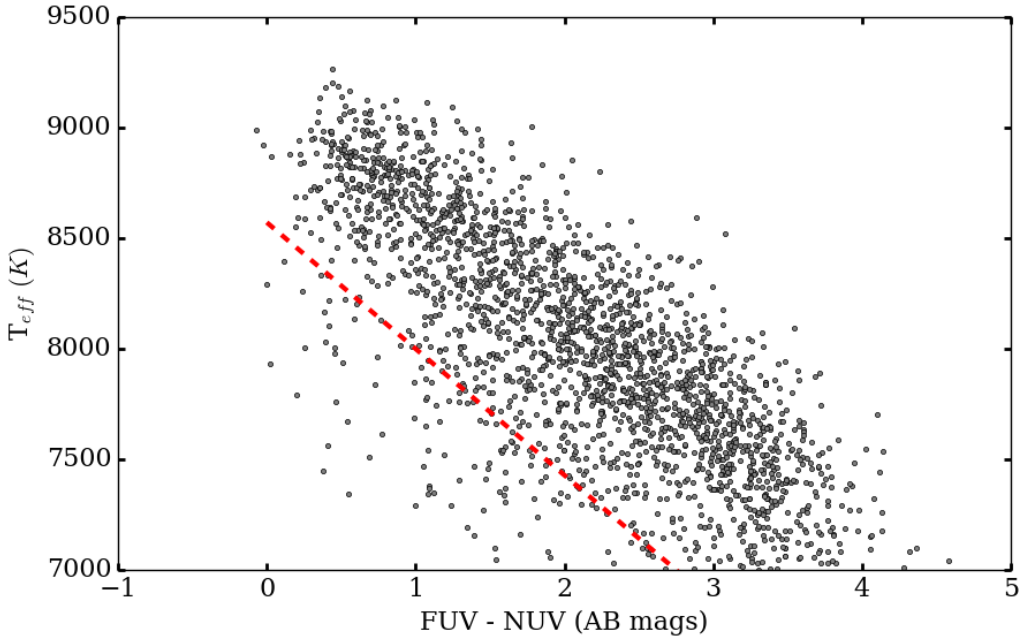

Figure 3.10: (FUV-NUV) vs. SSPP temperature values from SDSS-GALEX data. The red dashed line is the 2σ deviation from the fit to the diagonal sequence. Stars located left to this line are BSS with UV-excess.

3.2.8 BSS-WD Fitting

In order to obtain the stellar parameters of BSS-WD binaries, we fit the observed SED of UV-excess stars with a composite model SED consists of BSS and white dwarf. We employed theoretical grid of spectra developed by Kurucz(2004), in which the effective temperature, T_{eff} covers a range from 6000 to 10000 in steps of 250 K, and the surface gravity, $logg$ covers a range from 0.5 to 5. in steps of 0.5, and metallicity, $[Fe/H]$ covers a range from -2.5 to 0.5 in steps of 0.5. In order to use our SED fitting routine, model spectra were converted to bandpass fluxes, as explained in next section.

For white dwarf models we employed the theoretical color tables developed by Bergeron(University of Montreal; private communication). For these models stellar

Table 3.2: Stellar parameters and photometry of UV-excess BSS

ID	T_{eff}	*log g*	$[Fe/H]$	FUV	NUV	u	g	r	i	z
915-52443-549	7423 157	3.84 0.49	-0.69 0.2	19.0 0.17	17.13 0.04	15.76 0.02	14.71 0.01	14.68 0.02	14.73 0.01	14.82 0.02
740-52263-440	7673 129	4.32 0.15	-1.98 0.07	19.89 0.24	19.35 0.13	18.64 0.02	17.84 0.01	17.89 0.01	17.94 0.02	18.07 0.03
684-52523-47	7004 40	3.88 0.23	-0.78 0.05	20.93 0.21	18.06 0.03	16.41 0.03	15.44 0.02	15.3 0.01	15.27 0.02	15.34 0.02
3131-54731-429	7936 110	4.36 0.03	-1.35 0.1	20.08 0.25	19.57 0.07	18.55 0.03	17.53 0.02	17.56 0.01	17.62 0.01	17.59 0.03
2951-54592-114	7615 73	3.93 0.44	-2.07 0.16	19.42 0.24	18.64 0.1	17.55 0.02	16.51 0.02	16.49 0.01	16.54 0.01	16.57 0.02
2849-54454-349	7083 37	4.21 0.29	-1.53 0.02	19.46 0.18	17.57 0.05	16.22 0.01	15.32 0.02	15.2 0.02	15.16 0.01	15.22 0.02
1894-53240-211	7441 78	4.19 0.21	-1.25 0.08	21.18 0.26	19.58 0.04	18.48 0.02	17.44 0.02	17.33 0.01	17.37 0.01	17.43 0.02
2299-53711-626	7742 64	3.93 0.18	-0.25 0.04	21.67 0.43	20.53 0.19	18.71 0.03	17.61 0.01	17.61 0.01	17.7 0.02	17.81 0.03
2299-53711-453	7460 50	3.88 0.21	-0.24 0.08	21.01 0.48	19.53 0.16	17.69 0.02	16.5 0.01	16.45 0.01	16.5 0.01	16.58 0.01
2848-54453-473	7032 31	4.14 0.25	-1.41 0.04	19.47 0.1	17.15 0.02	15.9 0.01	14.95 0.02	14.82 0.02	14.81 0.02	14.88 0.01
1254-52972-515	7672 140	4.2 0.11	-0.02 0.05	18.66 0.38	17.5 0.12	15.96 0.02	15.01 0.01	15.07 0.02	15.15 0.01	15.33 0.01
1252-52970-306	7791 0	4.14 0.23	-0.25 0.03	16.95 0.11	16.75 0.06	16.28 0.02	15.4 0.02	15.41 0.01	15.48 0.01	15.61 0.02
2335-53730-480	7468 33	3.98 0.31	-0.49 0.14	19.14 0.46	17.75 0.15	16.04 0.05	14.98 0.02	14.9 0.02	14.97 0.02	15.02 0.02
3241-54884-335	8029 71	4.13 0.2	-1.97 0.25	19.3 0.21	18.9 0.13	18.16 0.04	17.23 0.02	17.32 0.01	17.42 0.01	17.54 0.02
685-52203-430	7686 112	3.93 0.36	-1.03 0.07	19.69 0.17	18.7 0.08	17.26 0.01	16.11 0.02	16.09 0.02	16.12 0.02	16.15 0.02
3130-54740-107	7344 69	4.15 0.22	-1.89 0.07	19.87 0.19	19.32 0.07	18.45 0.02	17.45 0.02	17.38 0.01	17.35 0.02	17.43 0.02
2252-53565-281	7301 44	4.19 0.16	-0.27 0.04	21.02 0.39	19.05 0.05	17.4 0.01	16.32 0.02	16.24 0.01	16.26 0.01	16.3 0.01
1961-53299-168	7291 45	4.05 0.19	-0.76 0.02	19.49 0.17	18.25 0.07	17.61 0.02	16.61 0.01	16.53 0.02	16.54 0.02	16.62 0.02
1960-53289-343	7127 33	4.23 0.17	-0.54 0.06	20.9 0.4	18.45 0.09	16.71 0.02	15.68 0.02	15.54 0.01	15.54 0.02	15.57 0.02
3138-54740-521	7381 31	4.03 0.3	-1.11 0.03	21.04 0.45	19.95 0.19	18.44 0.03	17.4 0.01	17.31 0.01	17.35 0.02	17.38 0.02
3138-54740-401	7562 177	4.31 0.16	-2.59 0.01	19.49 0.21	19.08 0.12	17.77 0.03	16.76 0.01	16.75 0.01	16.73 0.01	16.71 0.02
1857-53182-27	7343 129	4.31 0.2	-0.88 0.08	21.53 0.34	20.45 0.19	18.87 0.03	17.9 0.01	17.77 0.01	17.79 0.01	17.88 0.03
366-52017-28	7320 60	4.2 0.23	-1.01 0.08	21.16 0.37	19.37 0.12	17.88 0.02	16.91 0.02	16.86 0.01	16.86 0.02	16.92 0.02
2797-54616-614	8005 47	4.24 0.19	-1.22 0.32	20.87 0.38	20.41 0.26	18.74 0.04	17.67 0.01	17.71 0.01	17.81 0.02	17.92 0.03
2551-54552-257	7368 100	4.07 0.06	-1.31 0.06	21.51 0.34	19.91 0.12	18.75 0.02	17.58 0.02	17.51 0.02	17.52 0.02	17.52 0.03
2247-53857-96	7290 68	4.18 0.29	-0.54 0.04	20.57 0.34	19.57 0.14	18.18 0.02	17.1 0.02	17.05 0.01	17.08 0.01	17.15 0.02
2180-54613-519	7368 46	3.98 0.31	-1.83 0.01	20.94 0.29	18.85 0.06	17.75 0.02	16.89 0.02	16.87 0.02	16.87 0.02	16.92 0.02
1659-53224-452	7530 40	4.05 0.19	-0.56 0.09	19.56 0.15	17.9 0.05	16.46 0.02	15.39 0.01	15.38 0.01	15.45 0.02	15.55 0.02
2550-54206-232	7097 80	4.24 0.14	-0.97 0.05	21.17 0.36	18.61 0.07	17.16 0.02	16.15 0.01	16.04 0.02	16.02 0.02	16.04 0.02
2189-54624-640	7307 61	4.0 0.67	-1.5 0.0	21.51 0.45	19.91 0.11	18.71 0.03	17.74 0.02	17.73 0.01	17.75 0.01	17.84 0.03
595-52023-92	7542 81	4.11 0.08	-1.72 0.04	19.07 0.18	17.99 0.05	16.88 0.02	15.89 0.01	15.87 0.01	15.92 0.01	15.98 0.02
1727-53859-288	7045 39	3.84 0.43	-0.53 0.02	21.79 0.43	20.25 0.14	18.61 0.02	17.52 0.02	17.42 0.02	17.42 0.02	17.48 0.02
2782-54592-113	7445 103	3.88 0.45	-1.61 0.05	19.64 0.21	19.26 0.12	18.33 0.02	17.23 0.01	17.16 0.01	17.12 0.01	17.11 0.02
3308-54919-447	7368 82	3.92 0.4	-1.41 0.09	20.9 0.37	19.81 0.14	18.8 0.03	17.95 0.02	17.91 0.01	17.96 0.02	18.04 0.03
2781-54266-417	7768 145	4.37 0.16	-1.34 0.03	20.35 0.26	19.28 0.11	18.16 0.02	17.23 0.02	17.31 0.01	17.34 0.01	17.41 0.02
2156-54525-520	7483 58	3.89 0.42	-0.98 0.02	21.75 0.42	20.26 0.14	18.71 0.02	17.7 0.01	17.68 0.02	17.74 0.01	17.83 0.02
3297-54941-411	7411 56	3.98 0.45	-1.14 0.17	19.99 0.28	18.52 0.08	17.34 0.02	16.33 0.02	16.27 0.02	16.3 0.02	16.32 0.02
2152-53874-290	7557 40	4.14 0.23	-1.02 0.09	19.07 0.16	17.47 0.05	16.17 0.01	15.11 0.02	15.11 0.01	15.17 0.01	15.26 0.02
3406-54970-104	7191 81	4.32 0.02	-1.98 0.02	21.27 0.32	19.92 0.11	18.77 0.02	17.87 0.02	17.79 0.02	17.77 0.03	17.83 0.02
3406-54970-518	7335 50	4.25 0.18	-1.79 0.04	21.91 0.44	19.89 0.11	18.8 0.02	17.9 0.02	17.8 0.01	17.82 0.01	17.86 0.03
3387-54951-106	7979 116	4.21 0.38	-1.84 0.21	20.53 0.4	20.07 0.2	18.75 0.02	17.73 0.02	17.73 0.02	17.87 0.02	17.99 0.02
3384-54948-315	7403 67	3.89 0.33	-1.92 0.07	21.29 0.28	19.45 0.07	18.29 0.02	17.3 0.02	17.24 0.02	17.25 0.02	17.32 0.02
1348-53084-179	7652 15	4.19 0.21	-2.24 0.0	19.6 0.18	18.53 0.06	17.59 0.02	16.59 0.01	16.59 0.02	16.67 0.02	16.69 0.02
2124-53770-535	7005 44	4.08 0.04	-1.45 0.05	21.25 0.45	18.57 0.09	17.13 0.02	16.25 0.01	16.12 0.01	16.12 0.01	16.15 0.01
2336-53712-115	7469 22	4.07 0.23	-0.6 0.07	21.01 0.4	19.96 0.19	18.5 0.02	17.46 0.02	17.4 0.01	17.45 0.01	17.52 0.02
424-51893-60	7176 23	3.93 0.11	-0.61 0.09	21.31 0.46	18.84 0.09	17.09 0.02	16.04 0.02	15.94 0.02	15.95 0.01	16.0 0.02
2445-54573-173	7317 87	4.25 0.34	-1.37 0.46	21.78 0.34	19.85 0.1	18.72 0.02	17.66 0.02	17.57 0.02	17.65 0.02	17.69 0.02
1282-52759-79	7541 52	3.83 0.35	-1.8 0.13	21.1 0.37	19.53 0.11	18.32 0.02	17.22 0.03	17.23 0.01	17.29 0.01	17.36 0.02
3377-54950-189	7349 31	4.13 0.35	-1.38 0.09	19.95 0.21	18.83 0.07	17.75 0.02	16.84 0.01	16.78 0.01	16.81 0.02	16.84 0.02
2899-54568-252	7164 29	4.01 0.12	-0.22 0.05	20.04 0.23	17.51 0.04	15.63 0.03	14.57 0.02	14.46 0.02	14.47 0.01	14.56 0.02
1456-53115-620	7072 59	3.9 0.27	-0.84 0.04	21.53 0.48	18.97 0.05	17.32 0.02	16.22 0.02	16.14 0.02	16.18 0.02	16.24 0.02
2661-54505-400	7402 59	4.13 0.12	-0.7 0.08	20.64 0.27	18.93 0.05	17.65 0.02	16.61 0.02	16.59 0.01	16.62 0.01	16.71 0.01
335-52000-452	7758 159	4.1 0.16	-2.03 0.06	19.58 0.19	19.11 0.1	18.49 0.02	17.54 0.02	17.61 0.01	17.66 0.01	17.7 0.02
2647-54495-235	7096 51	3.9 0.12	-1.47 0.02	21.61 0.42	19.04 0.09	17.62 0.02	16.66 0.02	16.56 0.02	16.55 0.02	16.59 0.02
3253-54941-210	7296 41	3.96 0.27	-1.74 0.04	21.47 0.47	19.29 0.07	17.99 0.02	17.06 0.02	17.0 0.02	17.03 0.02	17.08 0.02
334-51993-267	7270 74	3.94 0.28	-1.38 0.01	21.78 0.41	20.32 0.13	18.76 0.02	17.7 0.02	17.63 0.02	17.66 0.01	17.71 0.02
3214-54866-426	7159 49	3.85 0.3	-1.68 0.04	21.69 0.48	19.99 0.16	18.55 0.04	17.6 0.02	17.57 0.02	17.55 0.02	17.61 0.02
2892-54552-128	7256 80	3.84 0.37	-1.99 0.13	22.22 0.3	19.94 0.08	18.67 0.02	17.82 0.02	17.71 0.01	17.71 0.01	17.77 0.02
3285-54948-131	7509 116	3.94 0.2	-1.66 0.02	18.48 0.1	17.79 0.05	16.93 0.03	15.98 0.03	16.03 0.03	16.06 0.02	16.14 0.03
2512-53877-326	7061 48	3.86 0.16	-2.04 0.09	21.44 0.38	18.85 0.04	17.48 0.02	16.5 0.01	16.41 0.02	16.44 0.01	16.46 0.02
3170-54859-111	7520 98	4.23 0.31	-2.39 0.05	20.12 0.14	18.93 0.04	17.87 0.02	16.86 0.01	16.82 0.01	16.84 0.02	16.89 0.02
878-52353-617	7240 51	4.14 0.31	-1.81 0.16	20.61 0.3	18.79 0.07	17.41 0.02	16.44 0.02	16.33 0.02	16.36 0.03	16.38 0.02
3193-54830-593	7838 78	4.19 0.22	-1.14 0.02	20.44 0.22	19.71 0.11	18.66 0.03	17.55 0.02	17.62 0.01	17.66 0.02	17.75 0.03
267-51608-422	7336 59	3.98 0.32	-1.55 0.06	21.55 0.36	19.96 0.1	18.5 0.02	17.5 0.02	17.44 0.02	17.49 0.02	17.56 0.03
1739-53050-128	7533 73	3.98 0.16	-2.23 0.05	20.89 0.37	19.31 0.08	18.01 0.02	16.98 0.02	16.81 0.01	16.87 0.02	17.13 0.02
1934-53357-4	7408 39	4.03 0.09	-1.43 0.15	21.64 0.28	20.35 0.12	19.02 0.03	17.97 0.03	17.95 0.02	17.98 0.02	18.02 0.04
1590-52974-388	7126 23	3.95 0.05	-0.24 0.02	21.86 0.46	19.31 0.1	17.71 0.02	16.58 0.01	16.49 0.02	16.51 0.02	16.57 0.02
3195-54832-552	7059 34	4.07 0.14	-0.42 0.03	20.81 0.39	18.9 0.1	17.32 0.02	16.3 0.02	16.22 0.02	16.2 0.01	16.26 0.01
3230-54860-409	7081 54	4.34 0.14	-0.42 0.07	20.77 0.37	18.49 0.08	16.74 0.02	15.65 0.02	15.55 0.02	15.58 0.02	15.63 0.02
2273-53709-207	7353 128	4.05 0.32	-0.48 0.13	20.97 0.4	19.41 0.12	18.1 0.02	16.86 0.02	16.72 0.01	16.67 0.01	16.62 0.01
3230-54860-353	7541 69	3.89 0.27	-1.52 0.05	21.47 0.49	19.89 0.17	18.76 0.02	17.75 0.01	17.71 0.02	17.77 0.02	17.84 0.02
3226-54857-452	8004 116	4.15 0.17	-0.52 0.17	18.15 0.11	17.89 0.02	17.58 0.02	16.66 0.01	16.74 0.01	16.86 0.01	16.99 0.02
758-52253-5	7930 117	3.99 0.18	-1.34 0.04	18.47 0.12	18.45 0.04	18.45 0.03	17.75 0.02	17.79 0.02	17.92 0.01	18.05 0.03
2420-54086-395	7780 101	4.07 0.38	-1.47 0.05	21.25 0.35	20.17 0.12	18.82 0.02	17.84 0.01	17.8 0.01	17.87 0.01	17.94 0.02
2541-54481-384	7282 26	3.87 0.0	-0.24 0.01	20.22 0.21	18.0 0.04	16.32 0.02	15.26 0.01	15.16 0.03	15.17 0.02	15.25 0.02
2055-53729-37	7297 44	3.99 0.25	-0.56 0.05	19.97 0.17	17.86 0.04	16.37 0.01	15.32 0.02	15.26 0.0	15.27 0.01	15.35 0.01
3166-54830-409	7203 14	4.18 0.12	-0.45 0.03	20.72 0.34	18.28 0.07	16.59 0.02	15.55 0.01	15.46 0.01	15.49 0.02	15.61 0.02
3161-54779-445	7351 62	4.04 0.23	-0.81 0.1	21.42 0.48	19.45 0.13	18.2 0.02	17.13 0.02	17.11 0.01	17.22 0.02	17.3 0.02
2941-54507-638	7097 25	4.09 0.11	-0.46 0.02	20.89 0.27	18.37 0.04	16.64 0.02	15.65 0.01	15.51 0.01	15.52 0.01	15.57 0.02
2337-53740-222	7100 26	3.89 0.17	-0.24 0.04	19.51 0.17	17.98 0.06	16.27 0.01	15.17 0.01	15.04 0.01	15.04 0.01	15.1 0.01

masses and cooling ages are obtained from a detailed evolutionary cooling sequences appropriate for these stars. For the white dwarfs with pure hydrogen model atmospheres above temperatures = 30,000 K, the carbon-core cooling models of Wood ([44]) with thick hydrogen layers of $M_H/M* = 10^4$ were used. For temperatures below 30,000 K, cooling models similar to those described in Fontaine, Brassard, & Bergeron et. al ([45]) but with carbon-oxygen cores and $M_H/M* = 10^4$ were used. For the pure helium model atmospheres, similar models being used but with $M_H/M* = 10^{-10}$.[5]

3.2.9 Synthetic Fluxes

In the course of fitting procedure we calculate synthetic fluxes for both BSS and WD in GALEX and SDSSS bandpasses. The synthetic spectra can be converted to a monochromatic flux for a given bandpass via,

$$f = \frac{\int_{\lambda_i}^{\lambda_f} \lambda f_\lambda S_\lambda d\lambda}{\int_{\lambda_i}^{\lambda_f} \lambda S_\lambda d\lambda} \tag{3.3}$$

where f_λ is the flux at a given wavelength λ and S_λ is the filter response at a given wavelength. The integration limits are the minimum and maximum wavelength of the bandpass.

3.2.10 Observed Fluxes

The observed, extinction corrected, magnitudes were transformed to fluxes using the standard formulas. For SDSS bandpasses,

$$m_{AB} = -2.5 \log f_\nu - 48.6 \tag{3.4}$$

[5]see Bergeron, Leggett, & Ruiz 2001, ApJS, 133, 413 for more details

Note, here according to definition introduced of Fukugita et.al (1996, [46]), flux is given in the units of frequency. To express this in terms of λ formalism, the only change need to be made is to replace f_ν by $\frac{\lambda^2}{c^2} f_\lambda$.

The FUV and NUV fluxes are determined by means of the conversion,

$$m_{FUV} = -2.5 \log \frac{Flux\ FUV}{1.40 * 10^{-15}} + 18.82 \tag{3.5}$$

$$m_{NUV} = -2.5 \log \frac{Flux\ NUV}{2.06 * 10^{-16}} + 20.08 \tag{3.6}$$

3.2.11 SED Fitting

In the fitting process we minimize the following chi-square function:

$$\chi^2 = \sum_i \frac{(\alpha^2 f_{wd,i} + \beta^2 f_{bs,i} - F_i)^2}{\sigma_{F,i}^2} \tag{3.7}$$

Where i sum over all bandpasses.

$f_{bs,i}, f_{wd,i}, F_i$ are the flux of the BSS model, flux of the WD model and flux of the observed star respectively. $\alpha = (R_{bs}/D)$ and $\beta = (R_{wd}/D)$ are scale factors depend on radii($R_{bs}\ and\ R_{wd}$) of each component and the distance (D).

The radii of both components (R_{bs}, R_{wd}) and distance are necessary as scale factors for the individual fluxes when combining the atmosphere models of both components to a single SED. However, for WD models the mass and the surface gravity is known. So for each model in the grid we can calculate the radius, according to:

$$R_{WD} = \sqrt{\frac{GM_{WD}}{g_{WD}}} \tag{3.8}$$

For the BSS, we first obtain absolute magnitude calibration for our sample. we used

transformation equations given in Zhao & Newberg(2006, [47]), which were derived from the SDSS stars with known UBVRI photometry, including a sample of BSS stars.

$$V = g - 0.561(g - r) - 0.004 \tag{3.9}$$

$$(B - V) = 0.916(g - r) + 0.187 \tag{3.10}$$

These transformations are valid within the range $-0.5 < g - r < 1.0$,([48]) which is consistent with the color range we adopted here.

Using the V magnitude we obtained from Equation 3.9, we can now calculate the absolute magnitude in V band (M_v)using the relation given in Kinman et al.(1994, [49]):

$$M_v = 1.32 + 4.05(B - V) - 0.45\left[\frac{Fe}{H}\right] \tag{3.11}$$

This relation was constructed by studying the BSSs in globular clusters with different metallicities covering a wide range of colors and absolute magnitudes.

The luminosity of the star can be then, found by using the M_v and bolometric correction as,

$$\left(\frac{L}{L_o}\right) = 10^{-0.4[M_v - V_o - 31.752 + (BC_v - BC_{v,o})]} \tag{3.12}$$

Where for the bolometric correction we adopt the values given by Torres(2010) [50] :

$V_o = -26.75$

$BC_{v,o} = -0.09$ and

$BC_v = a + b(logT_{eff}) + c(logT_{eff})^2 + ...$

Coefficient	Value ($3.70 < logTeff < 3.90$)
a	-0.370510203809015E+05
b	0.385672629965804E+05
c	-0.150651486316025E+05
d	0.261724637119416E+04
e	-0.170623810323864E+03

Table 3.3: Bolometric Corrections by Flower (1996) as a Function of Temperature: $BC_v = a + b(logT_{eff}) + c(logT_{eff})^2 + ...$

The BC_v coefficients are give in Table 3.5 which was adopted from Torres(2010) [50].[6]

Then, the radius of the BSS can be estimated using the relation,

$$\left(\frac{R}{R_o}\right) = \left(\frac{T_o}{T_{eff}}\right)^2 \left(\frac{L}{L_o}\right)^{0.5} \tag{3.13}$$

To select the best fit white dwarf model, the χ^2 value of each fit is calculated using the equation 3.7. The optimal SED fits for some of the stars are shown in Figure 3.11. The presence of a hot white dwarf companion in a BSS binary causes the excess FUV emission of the system. This is clear in Figure 3.11. The expected emission from BSSs without WD companions is much fainter than the observed flux at FUV. But adding WD companions of increasing temperature results in bright, blue emission as evidence by the best fitting composite model (Grey line in Figure 3.11).

3.2.12 Distribution of WD parameters

In this section, we present the distributions of mass, age and effective temperatures of the white dwarfs determined from our SED fitting routine. The values are given

[6]Note that these BC_v coefficients are reprint from the often used polynomial fits by Flower(1996), which were misprinted in the original publication.

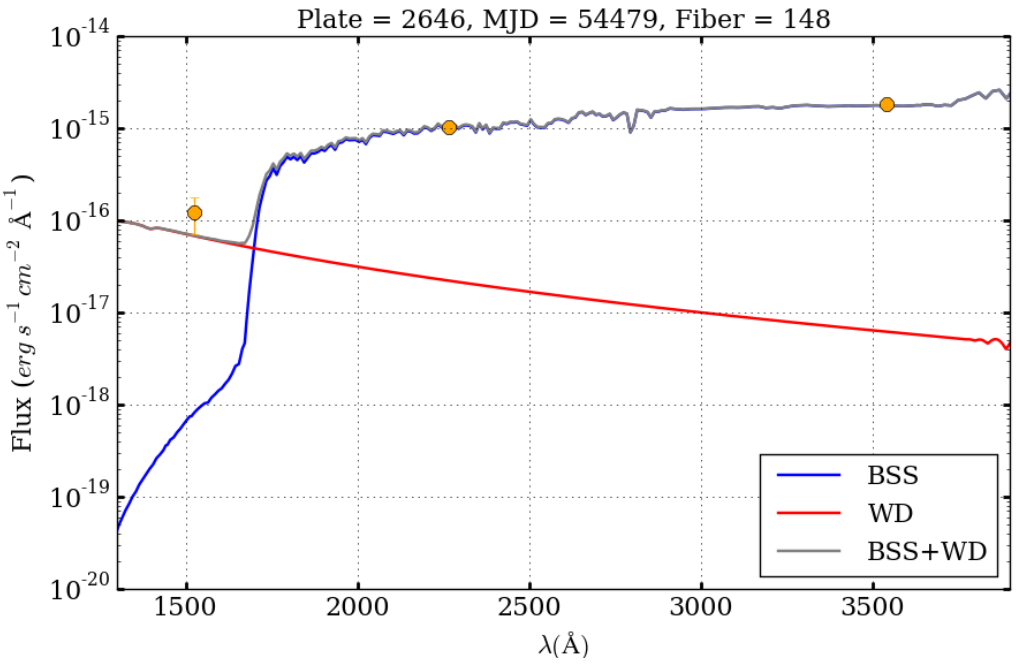

Figure 3.11: Example of BSS+WD fitting. Orange circles are the observed FUV,NUV and u photometry. Blue and Red lines represent the synthetic spectra of BS (ATLAS9- Kurucz) and WD (Bergeron) respectively.Grey is the combined best fit spectrum for observed photometry.

in table 3.

The most striking features of the distributions are: Vast majority of white dwarfs are very young (few million years old, See figure 3.11) and with temperatures range between 20000 - 40000 K (see figure 3.12).

This is consistent with our initial selection criteria of BSS, as recently formed BSS are expected to have mush larger UV excess.

The white dwarf mass distribution is shown in the bottom panel of figure 3.11.

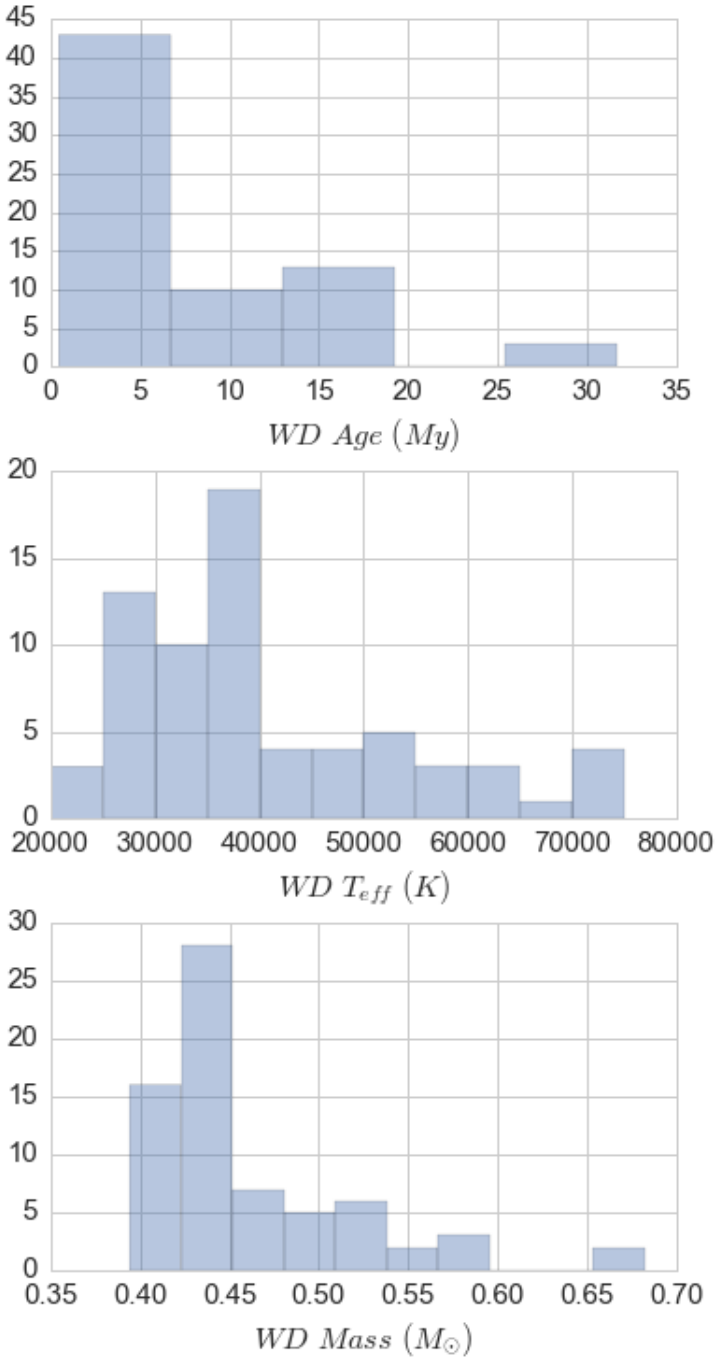

Figure 3.12: White Dwarf parameters

One interesting feature of the mass distribution is the peak at white dwarf mass 0.41 $M_{\odot}$. White dwarf stars with masses below 0.47 $M_{\odot}$ are thought to be He-core white dwarfs. (Core helium ignition starts when the core mass is roughly $0.47M_{\odot}$) If these stars were single stars, they would have main sequence life times that are longer than age of the Universe. Therefore these stars must be a product binary star evolution.

Only possible scenario for having such low mass white dwarf is case-B binary mass transfer. At this stage expanding red giant core has not yet fully grown, therefore the resultant white dwarf will appear with a smaller mass.

On the other hand white dwarfs with masses $> .5M_{\odot}$ are consistent with theoretical predictions from the Case-C mass transfer hypothesis. Case-C mass transfer (from an asymptotic giant to a main sequence star) leaves a carbonoxygen white dwarf companion with a mass of about .5 $M_{\odot}$ -0.6 $M_{\odot}$ dictated by the core mass of the asymptotic giant donor at the end of the mass transfer phase ([51]).

The WD Mass distribution in the Galactic field peaks at about 0.59 $M_{\odot}$ and exhibits a significant low- mass tail of white dwarfs with masses lower than 0.45 $M_{\odot}$ which peaks at 0.40 $M_{\odot}$ ([52]) (Figure 3.13). That white dwarfs predominantly found in close binary systems, mostly with another white dwarf or a neutron star companion ([53]). Interestingly, the low mass end of this distribution is consistent with our results as well.

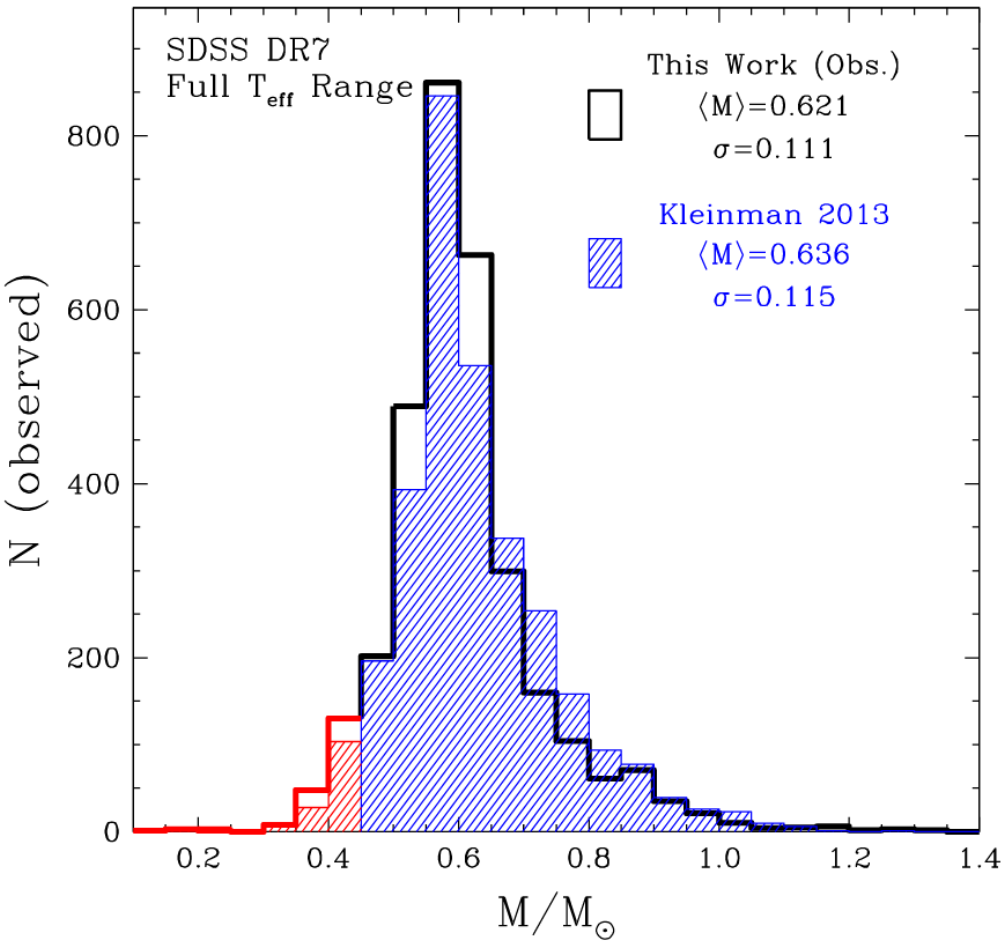

Figure 3.13: This figure adopted from [52] shows the comparison of the SDSS DR7 WD mass distributions from their work (black) and Kleinman et al. (2013, filled blue). The low-mass objects (red; M $< 0.45\ M_{\odot}$) are thought to be the WD originated from binary mass transfer processes.

The presence of any detected WDs can be used to map out the history of mass transfer-formed BSSs.

3.2.13 Mass Transfer efficiency

Mass transfer efficiency β, which is defined as the mass fraction of the lost mass from the primary accreted by the secondary, is an important parameter that determines the character of the BSS. This has been a major issue for the binary evolution calculations.

Table 3.4: Stellar Parameters of WD stars

ID	WD_Teff	WD_mass	WD_age(My)
915-52443-549	45000.0	0.68	2.81
740-52263-440	120000.0	0.7	0.07
684-52523-47	20000.0	0.39	31.7
3131-54731-429	70000.0	0.56	0.57
2951-54592-114	55000.0	0.51	1.29
2849-54454-349	30000.0	0.43	9.66
1894-53240-211	35000.0	0.45	4.59
2299-53711-626	35000.0	0.45	4.59
2299-53711-453	25000.0	0.41	16.8
2848-54453-473	25000.0	0.41	16.8
1254-52972-515	85000.0	0.6	0.27
1252-52970-306	120000.0	0.7	0.07
2335-53730-480	30000.0	0.43	9.66
3241-54884-335	120000.0	0.7	0.07
685-52203-430	70000.0	0.99	0.6
3130-54740-107	60000.0	0.53	0.96
2252-53565-281	30000.0	0.43	9.66
1961-53299-168	65000.0	0.54	0.74
1960-53289-343	20000.0	0.39	31.7
3138-54740-521	30000.0	0.43	9.66
3138-54740-401	55000.0	0.51	1.29
1857-53182-27	40000.0	0.46	3.1
366-52017-28	35000.0	0.45	4.59
2797-54616-614	60000.0	0.53	0.96
2551-54552-257	35000.0	0.45	4.59
2247-53857-96	50000.0	0.5	1.69
2180-54613-519	35000.0	0.45	4.59
1659-53224-452	35000.0	0.45	4.59
2550-54206-232	25000.0	0.41	16.8
2189-54624-640	50000.0	0.5	1.69
595-52023-92	50000.0	0.5	1.69
1727-53859-288	35000.0	0.45	4.59
2782-54592-113	50000.0	0.5	1.69
3308-54919-447	85000.0	0.6	0.27
2781-54266-417	75000.0	0.57	0.45
2156-54525-520	40000.0	0.46	3.1
3297-54941-411	35000.0	0.45	4.59
2152-53874-290	35000.0	0.45	4.59
3406-54970-104	35000.0	0.45	4.59
3406-54970-518	35000.0	0.45	4.59
3387-54951-106	55000.0	0.51	1.29
2337-53740-222	30000.0	0.43	9.66

Because of its uncertainty most calculations treat it as constant value.([54], [55]). Lu. p et.al used monte carlo simulations to calculate the models to investigate the origin of BSSs population in M67. In their calculations they used the $\beta = 0.5$ and $\beta = 1.0$ (fully conservative mass transfer, i.e. no mass or angular momentum loss from the system) and found that the higher value could reproduce the data better.

Using the WD parameters we obtained via the BSS-WD fitting can be used to infer the lower limit of this important parameter.

The amount of mass transferred from the now WD to BSS, δM_t,

$$\delta M_{trans} = M_i - M_{wd} \tag{3.14}$$

where M_i is the progenitor mass of the WD.

We interpolate theoretical relations which were constructed using BaSTI evolutionary models(Pietrinferni et al., 2006([56])) so that we can calculate the progenitor mass at a given metallicity and age (Figure 3.14).

We adopted the non-canonical BaSTI models with the mass loss efficiency of the Reimers law(Reimers 1977) set to η =0.2. The initial He mass fraction ranges from 0.245 to 0.303, for the more metal-poor to the more metal-rich composition, respectively. The adopted BaSTI models cover twelve metallicity bins: Z=0.0001, 0.0003, 0.0006, 0.001, 0.002,0.004, 0.008, 0.0100, 0.0198, 0.0240, 0.0300 and 0.0400.

Joffre P. et. al (2011, [57]) estimated the age of the field halo stars using as sample of SDSS stars. The estimated the mean age 11 giga years, which we adopted in our calculations to determine the mass from interpolated BASTI models. The field stars Joffre P. et. al used in their study has a metallicity of -1.6 dex. To be consistant with that work we limited our sample to the stars with $[Fe/H] <$ -1. This reduce our sample to 35 stars.

Following as similar procedure, we can determine the mass of the BSS M_{BSS} by using the theoretical relations and the temperature the of the BSS. However to calculate the amount of mass transferred one would require the initial mass of the

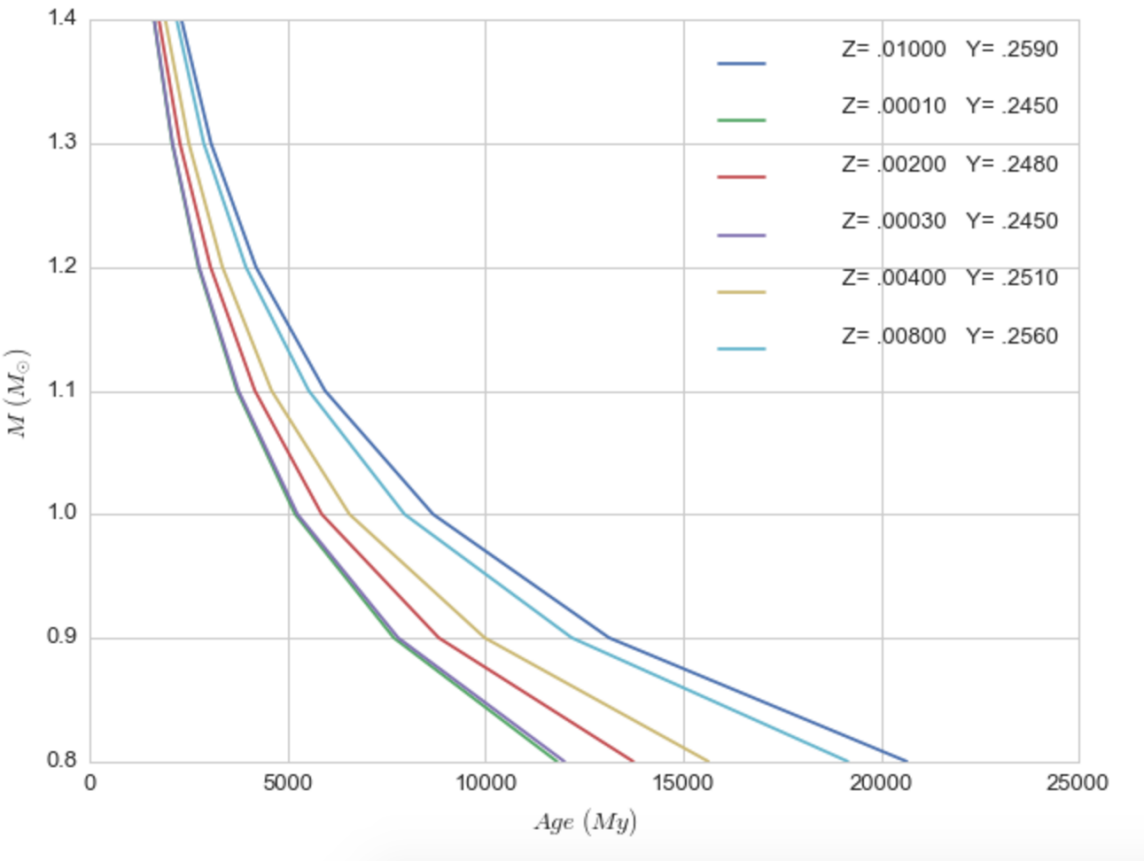

Figure 3.14: Theoretical mass-age relations from BaSTI evolutionary models.

secondary star (Now BSS), where the exact value is impossible to infer. But we can estimate the lower limit of the transferred mass by considering the halo turnoff mass of 0.8 $M_\odot$,

Then the mass accreted on to the secondary (now BSS) is given by,

$$\delta M_{acc} = M_{BSS} - 0.8 \tag{3.15}$$

Now this will give us the lower limit of the mass transfer efficiency.

The derived β values are shown as cumulative histogram in Figure 3.15. All the stars have mass transfer efficiencies above $\beta \sim 0.5$.

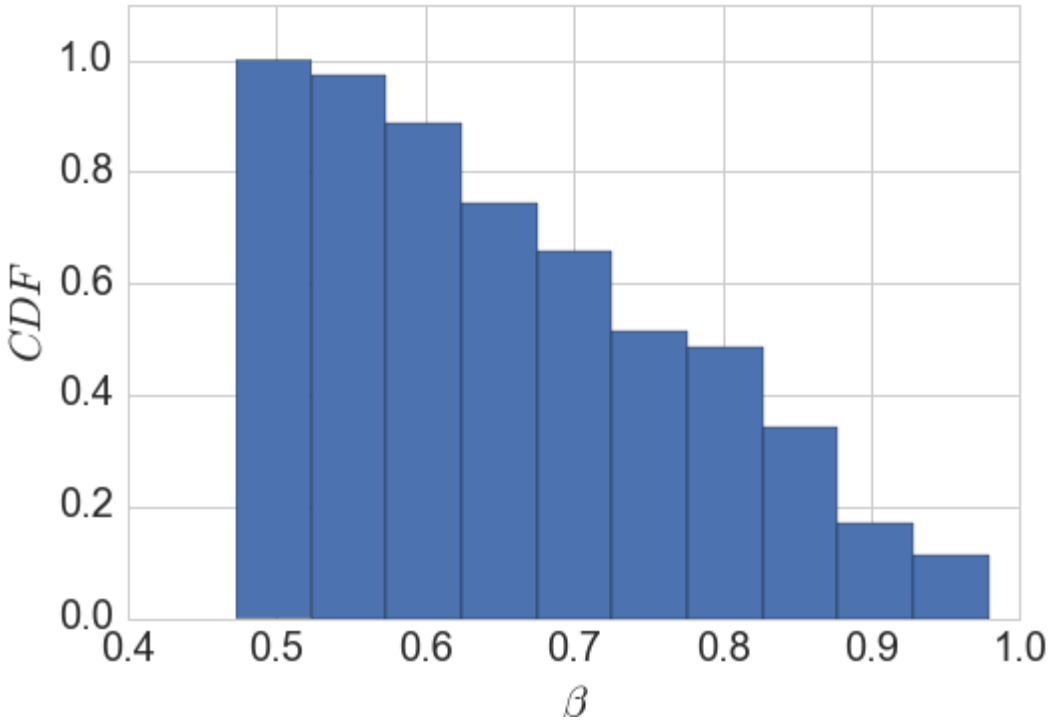

Figure 3.15: Cumulative distribution of mass transfer efficiency

The value we obtained for the lower limit of β is important to show that the nature the mass transfer. Since the majority of the stars tend to have larger β implies that in these binaries the conservative mass transfer is favorable.

3.3 Summary

We utilized UV-optical SED study of the BSS binaries in the Galactic field. Using our fitting routine we identified the WD companions to field BSSs which formed through ass transfer. We found these BSS has significant FUV excess by comparing the observed SED to a composite model with WD and BSS components.

We found WDs are not more than few million decades years old, suggesting mass transfer in these binaries ended very recently. In addition we conclude that majority

of the WDs are helium WDs. The obvious way to produce such low mass stars is via the mass transfer process of RGB star in a binary system.

Combining the WD stellar parameters with the evolutionary models we estimated the lower limit of the binary mass transfer efficiency in these stars to be, $\beta = 0.5$.

In order to determine the exact formation mechanisms for a particular population of BSSs a detailed characterization of the BSSs is needed. This require determining the rotation velocities and binary orbital parameters. Since the formation channel for BS binaries can distinguish from the type of companion star expected, it is vital to identify the observational constraints of the companion. In addition these binaries will be good test cases for more sophisticated mass transfer modeling efforts in the future.

Chapter 4 Canis Major Overdensity

4.1 Introduction

The existence of strong elliptical-shaped stellar overdensity, close to the Galactic plane at $(l = 240, b = 8)$, in the constellation of Canis Major was identified by Martin et. al in 2004 ([58]), based on the analysis of red giant stars of the 2 Micron All Sky Survey (2MASS). They identified the large scale Galactic asymmetry in stellar distribution above and below the Galactic plane and was first interpreted as a remnant of a disrupting dwarf galaxy.

In addition their follow up spectroscopic study showed that that the M-giants in Canis Major Overdensity (CMO) has average velocity of 109 km/s with a low dispersion, which is not consistent with the expected velocity for thick disk stars, thus supporting their initial hypothesis.

The idea of external origin is consistent with current paradigm of galaxy formation, which states that large disk galaxies like our Milky Way can be formed by the accretion of smaller systems of dark matter, stars and diffuse gas. Therefore merging dwarf galaxy has been thought to be the progenitor of the, so called Monoceros stream, a low-latitude stellar stream encircling the Milky Way about 100 degrees at a galactocentric distances from 15 kpc to 20 kpc ([59]). Penarrubia et. al (2005, [60]) attempted to figure out the current location of the progenitor of the Monocerros stream through N-body dynamical modelling. They have shown that it is possible to find a model that explains all the detected parts the stream that is consistent with CMO being the projenitor of the stream.

Another hypothesis regarding the origin of CMO is that the overdensity is due to an effect of the stellar component of the warp of the Galactic disk. Momany et. al (2004, [61]) showed that the overdensity can be explained by a simple shift

of the Galactic plane by 2 degrees to the south. They compared the kinematics of CMa M-giant selected sample with Galactic disk stars in the UCAC2 catalog and found no abnormality in proper motion, suggesting CMa stars represent the thick disk kinematics. In addition Using the UCAC2 proper motion catalogue, they showed that stars composing the overdensity are rotating around the Milky Way in a prograde manner and at a tangential velocity that is compatible with the disc.

One of the main obstacles for resolving this issue of CMO origin is the very high extinction in the Galactic disk. Due to it's position at very low galactic latitude the stars in CMO suffers significant extinction from dust and gas. Many of the studies of CMD have adopted their reddening values from the maps presented by Schlegel et. al(1998,[62]). Some authors suggested that Schlegel maps overestimated the reddening values for $E(B-V) > 0.2$ ([63]). Momany et. al (2006, [53]) used the reddening values adopting the reddening corrections as suggested by Bonifacio, and showed that the effect of reddening in detecting the overdensity (Figure 4.2).

In this work we present a photometric and spectroscopic study of sample of red clump of stars along the line of sight of the center of the CMO. We use these stars to measure the Galactic extinction towards the CMa and estimate the kinematic signature towards the CMO.

4.1.1 Red Clump Stars

The red clump is a prominent feature in the color magnitude diagrams of intermediate-age star clusters. This represents moderately high metallicity, low mass stars in the stage of He-burning in their cores. Due to their relatively large convective envelopes, they appear at the redder end of the horizontal branch close to the first-ascent red giant branch. Theoretical models predict that their absolute luminosity fairly weakly depends on their age and chemical composition. This constant intrinsic luminosity of RC stars gained significance as standard candles so they are widely used as

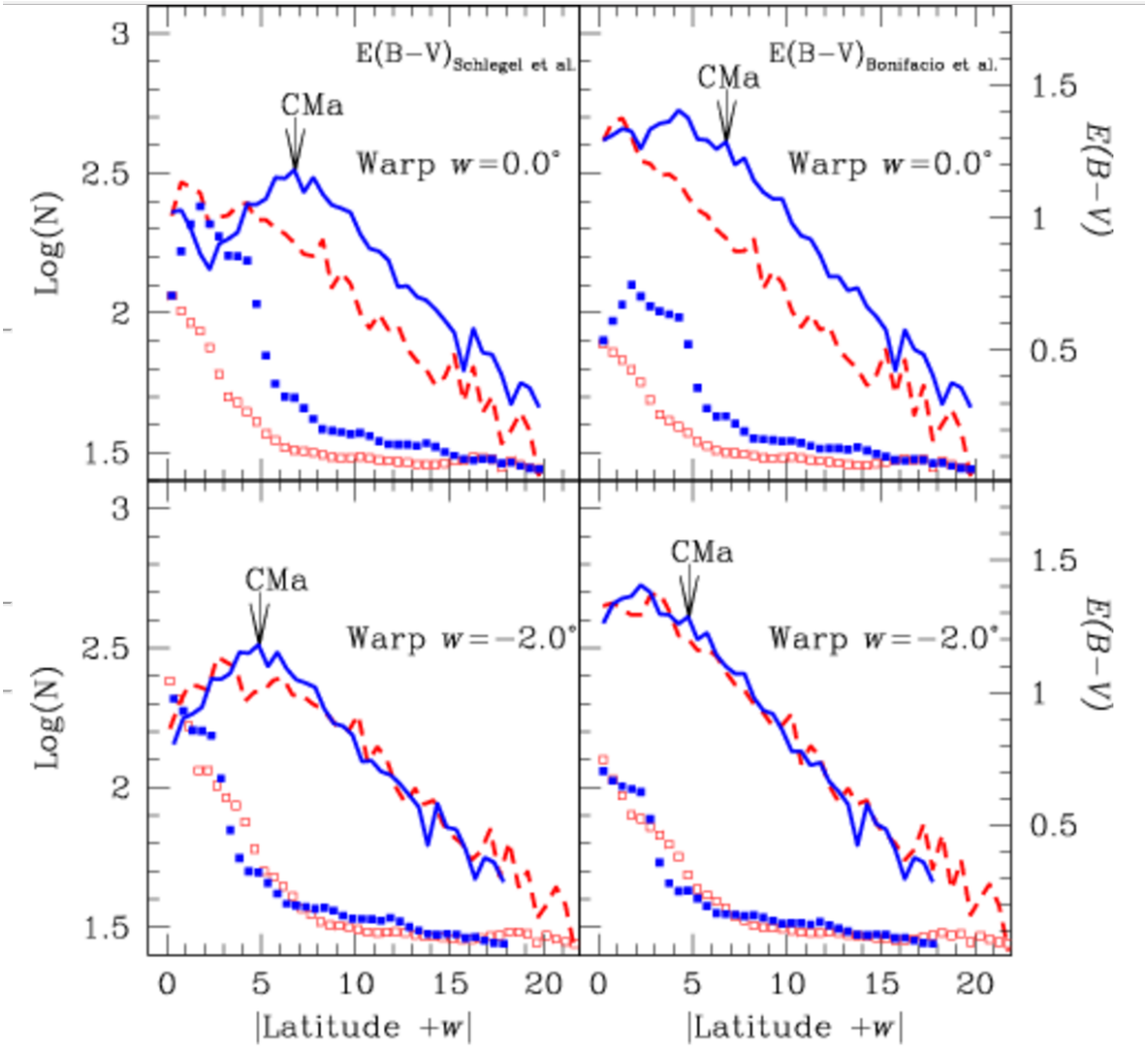

Figure 4.1: Latitude profiles of a 2MASS M-giant star sample selected around CMa. Upper-left panel assumes a North/South symmetry around $b = 0°$, lower-left panel assumes a warp amplitude of $2°$ in the southern direction. Star counts in left panels are corrected for reddening using the Schlegel et al. maps. Right panels show the same plots, except for correcting the Schlegel et al. values with the formula given in Bonifacio et al. showing the CMa over-density has almost disappeared.

probes of stellar distances, ages, kinematics, and extinctions ([64], [65]). The absolute magnitude-color diagram obtained from Hipparchus data clearly shows this compact nature of the absolute magnitude such that the variance in the I-band is only about 0.15 mag (Figure).

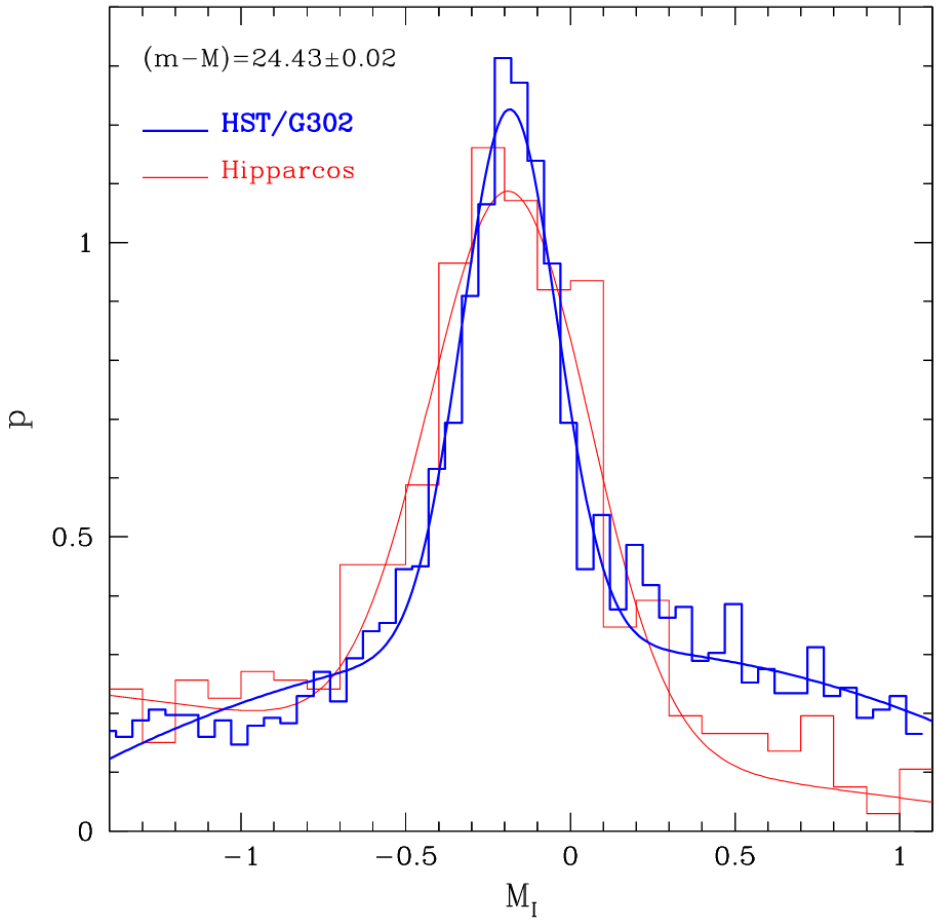

Figure 4.2: The number of red clump stars in the solar neighborhood, based on Hipparchus data,is shown as a function of absolute magnitude of I band with the thin solid line (fit and histogram).The number of red clump stars in the G302 field (Holland et al. 1996), is shown as a function of absolute magnitude with thick solid line. All distributions are normalized. Adopted from [66]

4.1.2 Observational Data

The data for this study come from two sources. The photometric data in Johnson U,B,V,R and I bands were come from a photometric survey conducted by Giovanni Carraro. The original data set consists of 670 stars, observed along the line of sight of the expected center of the CMD. All of these stars were observed in 2MASS survey, so we extracted the 2MASS J,H and K band photometry for these stars by cross-matching the catalogues. While we working on this project, the first data from the

Pan-STARRS1 (PS1-DR1) was released ([67]). By positional cross matching of PS1-DR1 catalogue with our data, we obtained PS1 photometry for all the stars in our sample. The PS1 survey used a 1.8 meter telescope and its 1.4 Gigapixel camera to image the sky in five broadband filters (g, r, i, z, y).

Kenneth Carrel[1] conducted a spectroscopic survey on a selected sample from Carraro's photometric data. From the photometric data he selected candidate RC and Blue Plume (BP) stars based on their position on $V-(V-I)$ color-magnitude diagram (Figure 4.3). These candidates stars were observed using the AAOmega spectrograph at the Anglo-Australian telescope. The spectra has resolution of 2000 and average signal to noise ratio of 25.

4.2 Analysis

4.2.1 Red Clump Selection

As mentioned in previous section, our initial candidates of red clump stars were selected using the $V-(V-I)$ color-magnitude diagram (Figure 4.3). While the chosen color-magnitude cut encompasses majority of red clump stars, it also allows for the inclusion of large number of contaminating nearby main-sequence stars and G,K giant stars from the Galactic disk.

To minimize the contamination from both the main sequence and red giant stars we estimated their stellar parameters.

4.2.2 Separating RC from Giants

Bovy et. al (2014, [68]) presented a method to limit the contamination from red giants while building the APOGEE-RC catalog. using stellar evolutionary models and high quality asteroseismology data they were able to calibrate and identify large number of red clump stars from the APOGEE data. They applied temperature

[1]http://www.angelo.edu/

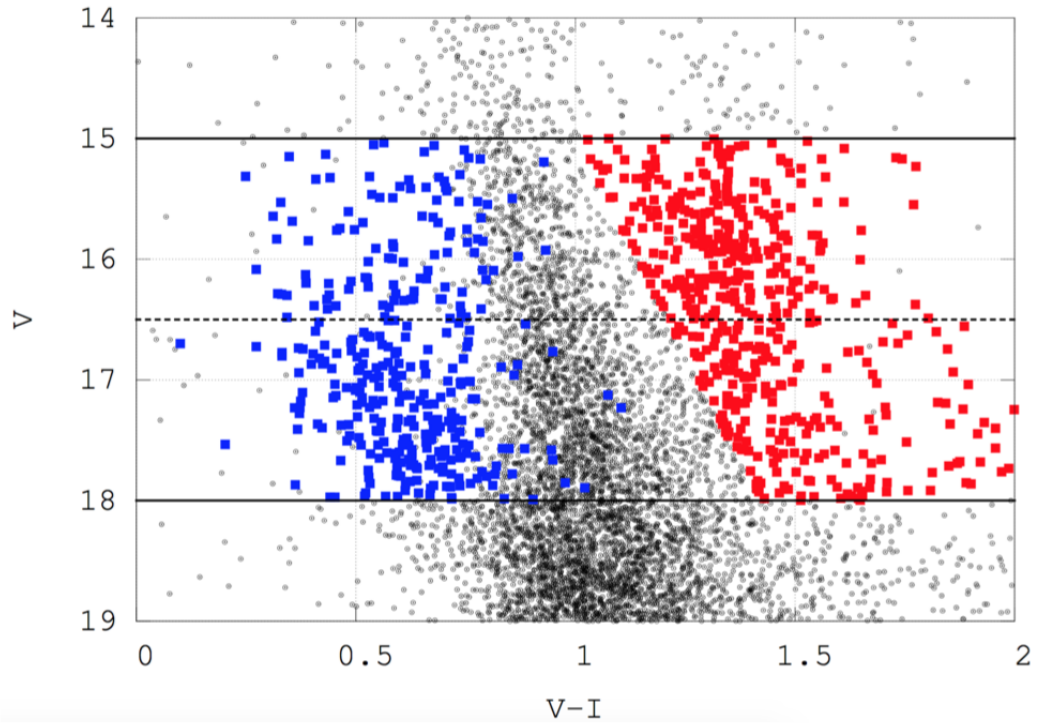

Figure 4.3: The CMD in the V vs V-I plane of all stars in the direction of the CMO. Data points in red indicate stars belonging to the red clump. For the clarity the Blue Plume stars are also highlighted in blue.

dependent cuts to identify the systematic differences between the RGB and RC stars that have similar metallicities. These cuts are valid only if the accuracy of the stellar parameters are comparable with that of APOGEE data. Currently spectroscopic pipeline for APOGEE has the errors 200 K for temperature and 0.2 dex for both *log g* and metalicity.

Anna q Ho et. al.(2017, [69]) present a data-driven method (this package is called *The Cannon*) applied to spectral modeling to determine the stellar parameters of the low-resolution LAMOST giants. Using overlapping data set from both surveys as a training set they measured LAMOST stellar parameters with typical uncertianities of 70 K in T_{eff}, 0.1 in *log g* and 0.1 in $[Fe/H]$, and 0.04 in $[\alpha/\mathrm{M}]$, values comparable to

the conservative APOGEE DR12 uncertainties. This method increases the accuracy of LAMOST data set significantly.

In order to get a much cleaner sample of red clump of stars we decided to use *The Cannon* to measure the stellar parameters for our stars using the LAMOST giants as the training set. The applicability of the spectral model created by The Cannon is limited by the bounds of the training set. Therefore we need to restrict our test set such that they are reasonably close to the training set. To that end we employed spectrum fitting package ULySS to measure stellar parameters, to select the candidate giant stars from our sample.

4.2.3 Atmospheric Parameters using UlySS

The spectrum fitting package ULySS[2] was developed by Koleva et. al(2009,[70]) Main technique behind this package is minimizing χ^2 between an observed spectrum and a linear combination of non-linear models. UlySS constructs a model spectrum using the MILES interpolator, presented in Prugani et. al (2011, []) using MILES spectral library. The interpolator returns a spectrum for any temperature, metallicity, and gravity by an interpolation over the entire MILES library. Then the program identifies the best fitting parameters for a given observed spectrum. For our sample, fit is performed over the wavelength range 3900 - 6800 Å.

The results from UlySS stellar parameters are shown in Figure 4.4. Based on their distribution in the $T_{eff} - log\ g$ plane it is possible to separate high gravity main sequence stars from giants with ease.

By applying a simple cut of $log\ g < 4.0$ and $T_{eff} > 4500$, we selected a sample of 217 red giants stars. Then from this giant sample we need to identify individual RC candidates in order to continue our analysis.

[2]http://ulyss.univ-lyon1.fr/

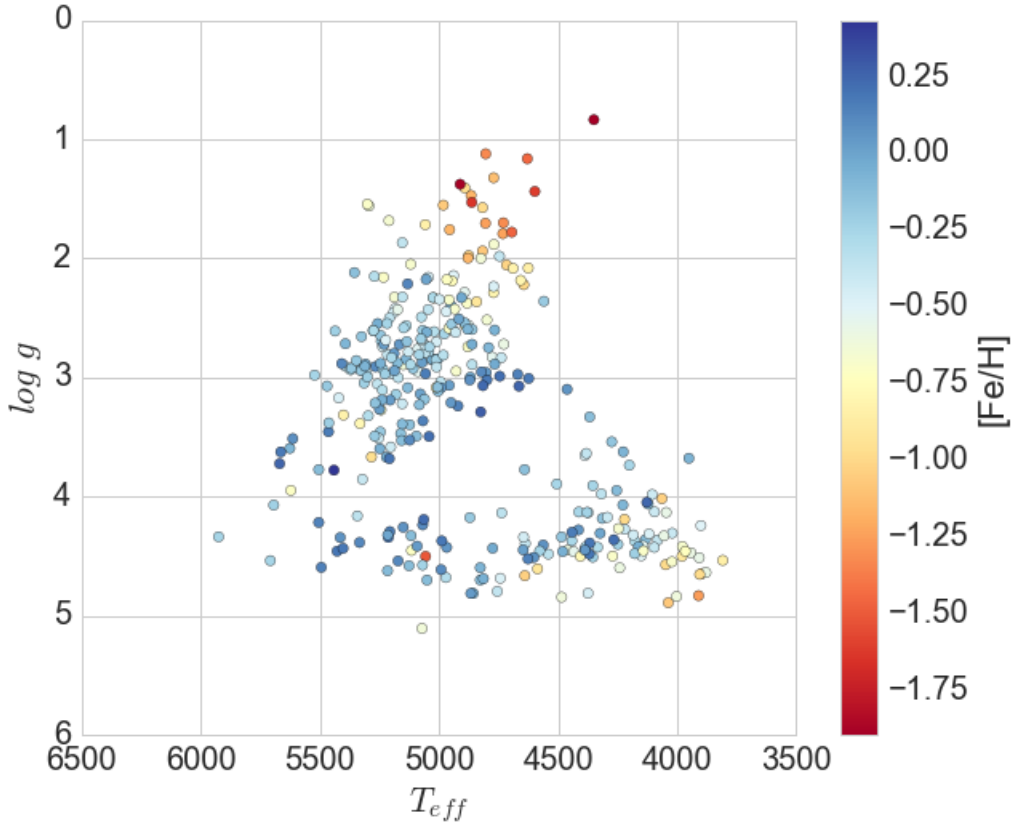

Figure 4.4: The stellar parameters derived from ULySS spectrum fitting.

4.2.4 The Cannon

The Cannon is a data driven method that construct a generative model based on the spectra in the training set. It constructs a probability density function (pdf) as a function of 'labels' (stellar parameters) for the flux of the spectra as a function of wavelength. The spectral model is characterized by θ_λ the coefficients at each wavelength λ and l_n some function built from the labels of the training set:

$$f_{n\lambda} = \theta_\lambda l_n + noise \tag{4.1}$$

The noise is an rms combination of the associated uncertainty variance $\sigma^2_{n\lambda}$ of

each of the pixels of the flux from finite photon counts and instrumental effects and the intrinsic variance or scatter of the model at each wavelength of the fit, s_λ^2. This model assumes that the noise model is a Gaussian random number with zero mean and unit variance.

In the test step, the spectral model is being used to predict the labels to the test spectra. This is the inverse of the Equation 4.1. Here *The Cannon* uses the spectral model coefficients and scatter, to be exactly those that were determined in the training step. Then the pixels and fluxes of a test spectrum are optimized for the labels of that star.

To be used by *The Cannon* any spectroscopic data set must satisfy the conditions laid out in Ness et al. (2015, [71]). The spectra must have same resolution, wavelength coverage and must be continuum normalized. In addition each spectrum must be accompanied by a noise spectrum.

4.2.5 Training Step

In training step The Cannon uses the objects in training set to train the model.

We define the label vector, l_n of the equation (4.1), to be a quadratic function of labels.

4.2.5.1 LAMOST Data

LAMOST, also called the Guo Shou Jing Telescope, is a 4-meter reflecting Schmidt telescope with 4000 fibers on a 20-square degree focal plane ([72]). The LAMOST survey is planned to observe more than 5 million low resolution stellar spectra during its 5-year survey. The resolution of the spectra are around 1800 which is consistent with the resolution of our sample.

We selected a subset of LAMOST stars as our training set, presuming the labels determined by Anna q Ho et. al.(2017, [69]) to be ground truth. In selecting the

training set we adopt following cuts in labels: $4100 < T_{eff} < 5500$, $1 < log\ g < 4.$ and $1 < [Fe/H] < 4.$.

Figure 4.5 shows the first order coefficients of the labels in the spectral model. The higher the coefficient at a given wavelength, the more the flux is sensitive to the label at that wavelength. Note there are many regions where the different labels dominates in contribution to the flux. It is evident that spectral feature likes Mg I, Na I D, and the Ca II triplet are all sensitive to the T_{eff}, $log\ g$ and $[Fe/H]$.

4.2.6 Test Step

Using the spectral model we developed in the train step we derived the labels for our test stars. The newly derived stellar parameters are show in figure 4.6. The mean metallicity of the stars is $\sim$ -0.30. which is consistant with the mean meatallicity of the thick disk at this distance.

The errors in The Cannon are determined from the covariance matrix of the model. The typical uncertianities of the test labels are 70 K T_{eff}, 0.1 for $log\ g$ and 0.1 for $[Fe/H]$.

4.2.7 RC Sample

Based on the stellar parameters derived we then proceeded to select the RC stars from our sample. We followed the methodology described in Bovy et.al([]).

We start with the cut,

$$1.8 < log\ g < 0.0018 dex/K(T_{eff} - T_o([Fe/H])) + 2.5 \tag{4.2}$$

where,

$$T_o = -382.5 K/dex[Fe/H] + 4607 K \tag{4.3}$$

Our final RC sample include 74 stars. Using this sample we can estimate the reddening and the kinematics towards the CMO.

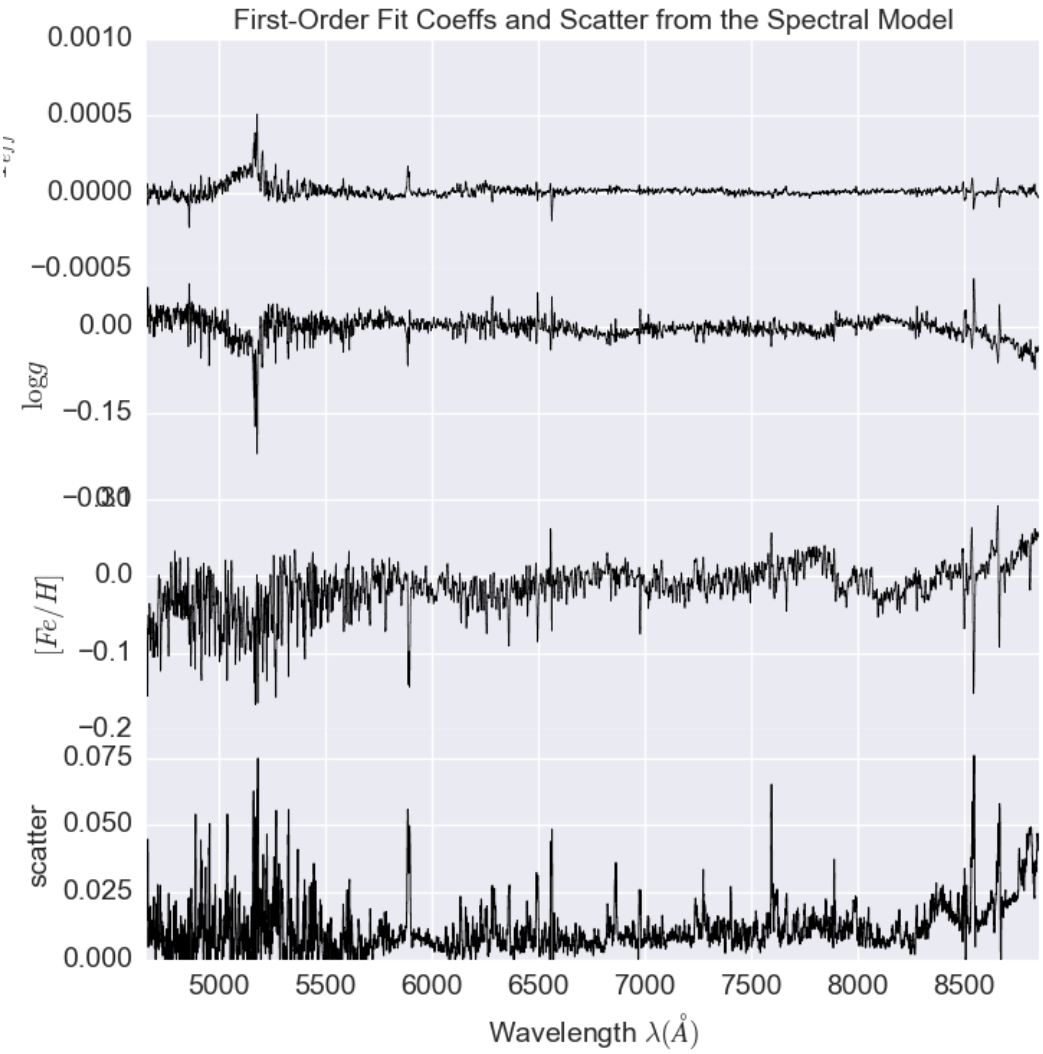

Figure 4.5: First-order coefficients and scatter of the spectral model.

4.2.8 Reddening Estimation

To estimate the individual reddening of each star we fit the observed energy distribution to a best fit model SED. Since we already know the stellar parameters we can select the model SED that best represent the observed star. The difference in the model the observed SED depend two parameters, the distance to the star and the extinction. These are treated as free parameters in our fitting routine.

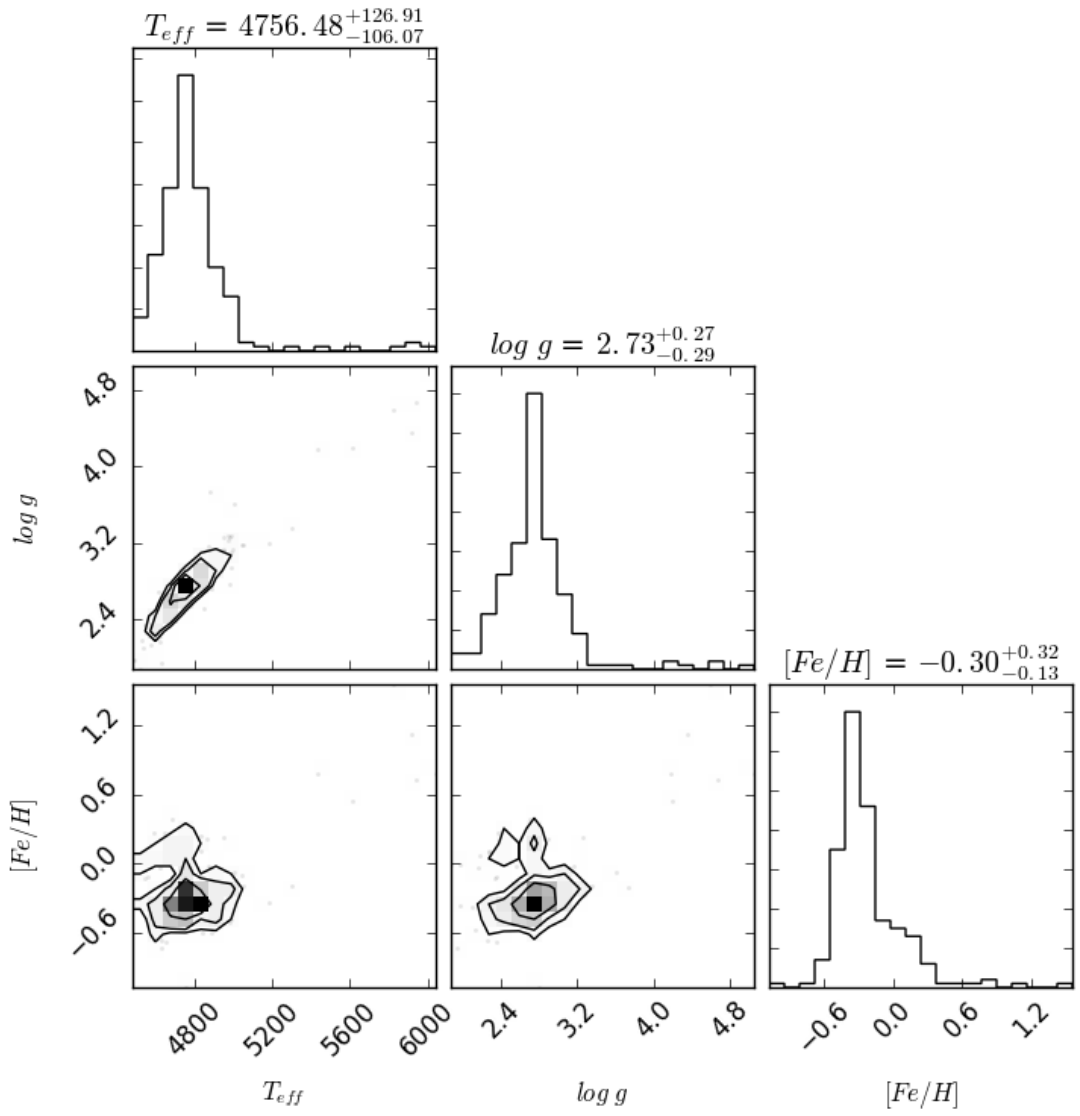

Figure 4.6: Stellar parameters derived from The Cannon.

The best fitting reddening value is obtained by minimizing the following function.

$$\chi^2 = \sum_{n=1}^{n} \frac{(f_{i,o} - \alpha f_{i,m} 10^{-0.4 k_i E(B-v)})^2}{\sigma_{i,o}^2} \tag{4.4}$$

n : number of photometric points

$f_{i,o}$: observed flux in band i

$f_{i,m}$ model flux in band i

k_i : extinction coefficient for a given passband i

$\sigma_{i,o}$: observation error in flux in band i

$\alpha = (\mathrm{R/D})$: a scaling factor depends on radius R and distance D.

The SEDs were constructed using the all available flux data including Johnson, 2MASS and PS1. The photometric magnitudes were converted to flux using the relation;

$$m = -2.5log(f) + ZP \tag{4.5}$$

Magnitude zero points are adapted from Bessel (1990, [73]) and Tonry et. al (2012, [74]).

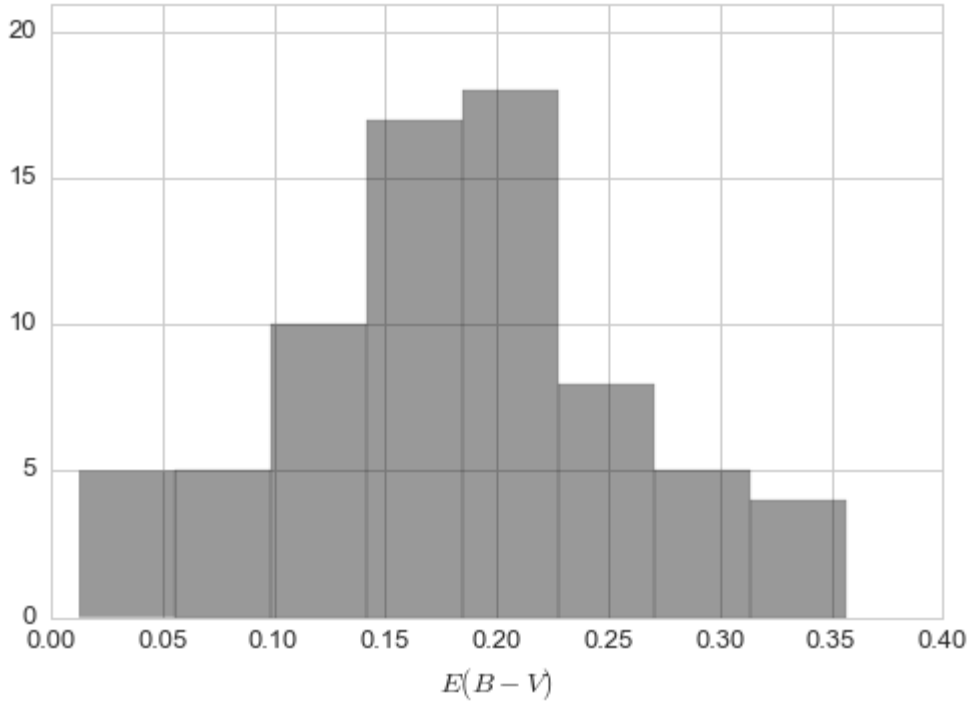

Figure 4.7: Stellar parameters derived from The Cannon.

The histogram of $E(B-V)$ for individual star are shown in figure 4.7. The distribution has mean value of $E(B-V) = 0.19$. This in agreement with the value

predicted at the center of CMO by Schlegal et. al maps. In addition the recent 3D dust maps constructed by Green G. et. al indicates average reddening of $E(B-V) \sim 0.20$ towards this location.

4.2.9 Distance Measurements

Given the reddening values obtained in the previous section, we now proceed to analyze the distribution of RC stars. We start off by looking at the heliocentric distances to the CMO.

In order to estimate the distances to individual stars we require absolute magnitude. There are many absolute magnitude calibrations of RC stars using different photometric bands (For example [75] and [76]).

The average absolute Ks magnitude of nearby RC stars is well-calibrated using Hipparchus parallaxes. We choose the recent Laney et al. (2012) calibration of $M_K = -1.61$ of local RC stars. This calibration is in very good agreement with the work of Alves (2000, [77]), but is 0.07mag brighter than the calibration of van Helshoecht, V. et. al ([78]).

The distance to a star from the Earth is given by,

$$D_{helio} = 10^{\frac{k-M_K}{5}-2} \tag{4.6}$$

The calculated distances to the individual stars is shown in Figure 4.8. Standard error analysis off Equation 4.6 gave the average distance error of 15%.

As can be seen in the Figure 4.6, the stars located at centered around 8 kpc. This is consistent with the CMO distance estimated by Martin et. al.(2004) and Bellazini et.al.

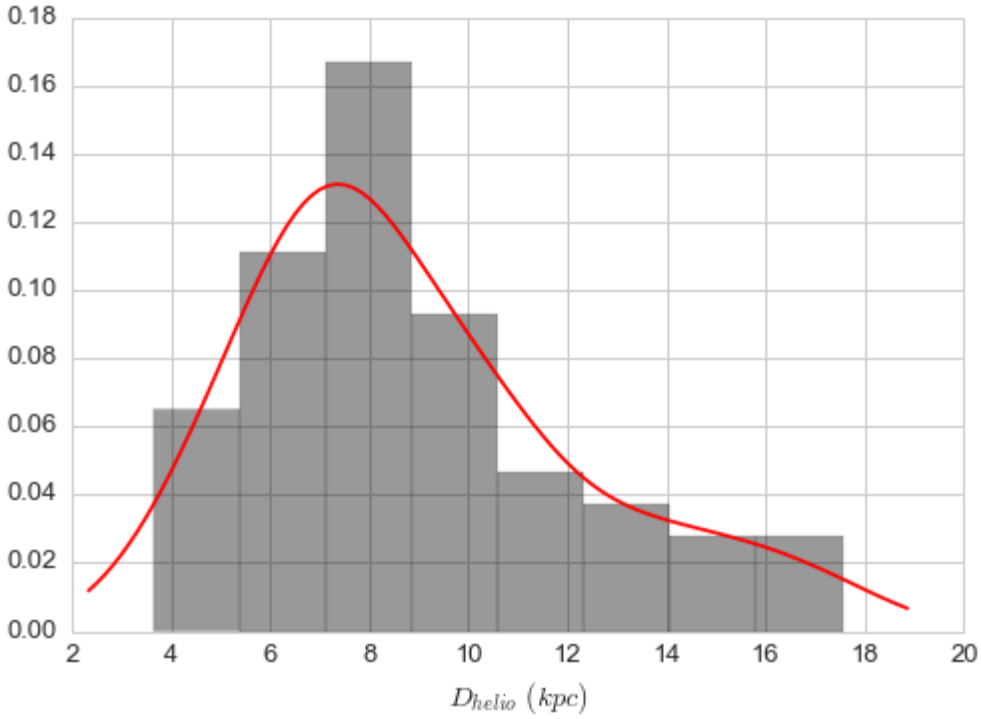

Figure 4.8: Heliocentric distance distribution of RC stars.

4.2.10 Velocity Distribution

The line of sight velocities (V_{helio}) measured from RC spectra are with respect to the sun. We converted the V_{helio} to line of sight velocity with respect to the Galactic Standard of rest using the relation given in Li et al. (2012, [79] and Dehnen et.al. (1998, [80]),

$$V_{GSR} = V_{helio} + 10coslcosb + 220.0sinlcosb + 7.2sinb \tag{4.7}$$

Also, the heliocentric distances can be converted to the Galactocentric distance using the following equation.

$$D_{GC} = \sqrt{[D_{helio}cosbcosl - D_{\odot}]^2 + D^2_{helio}cos^2bcos^2l + D^2_{helio}sin^2b} \tag{4.8}$$

where we adopt the distance to the Galactic center $D_{\odot} = 8.0\ kpc$, according to Boehel et. al. (2016, [81]). Figure.. show the distance vs velocity with respect to the Galactic Standard of rest. Dashed lines represent the Galactic rotational velocities evaluated at the location of the CMO. These lines were constructed for three different rotational velocities $v_{\phi} = 150, 180, 210 km/s$ using the following relation.

$$V_{GC} = \frac{8.0\ V_{\phi} cosb cosl}{\sqrt{D_{GC} cos^2 b cos^2 l - 8.0\ cosb cos^2 l}} \tag{4.9}$$

The average azimuthal velocities of the Galaxy are $v_{\phi} = 15, 180, 215 km/s$ for the halo, thick disk and thin disk respectively ([81]). Figure 4.9 implies that stars in our sample follow either thick disk or thin disk velocities. In addition the large velocity dispersion of the sample suggests that these stars are a part of dynamically hot component, in contrast to a dynamically cold merger remnant.

4.2.11 Alpha Element Abundance

Analysis of the elemental abundance patterns in thick-disk stars is very useful in unraveling the information about the Galactic evolution. The ratio of Alpha Element Abundance to iron $[\alpha/Fe]$, is one of the most important measurement that provide information about the star formation history in the Galaxy.

The observed [alpha / Fe] trend with [Fe/H] is due to the time delay between SN II, which produce alpha elements and iron-peak elements (Arnett 1978, [82]), and SN Is, which yield mostly iron-peak with little alpha element production.

Studies of disk dwarf stars by several authors confirmed the trend of increasing [alpha / Fe] with decreasing [Fe/H] in the Galactic disk. Hayden et. al (2014, [83]) Used a sample of 69,919 red giants from the SDSS-III/APOGEE Data Release 12, to measure the distribution of stars in the $[\alpha/Fe]$ vs. $[Fe/H]$ plane. They found that the location of the high-alpha sequence is nearly constant across the disk, however there are very few high-alpha stars at R $>$ 11 kpc (Figure 4.10).

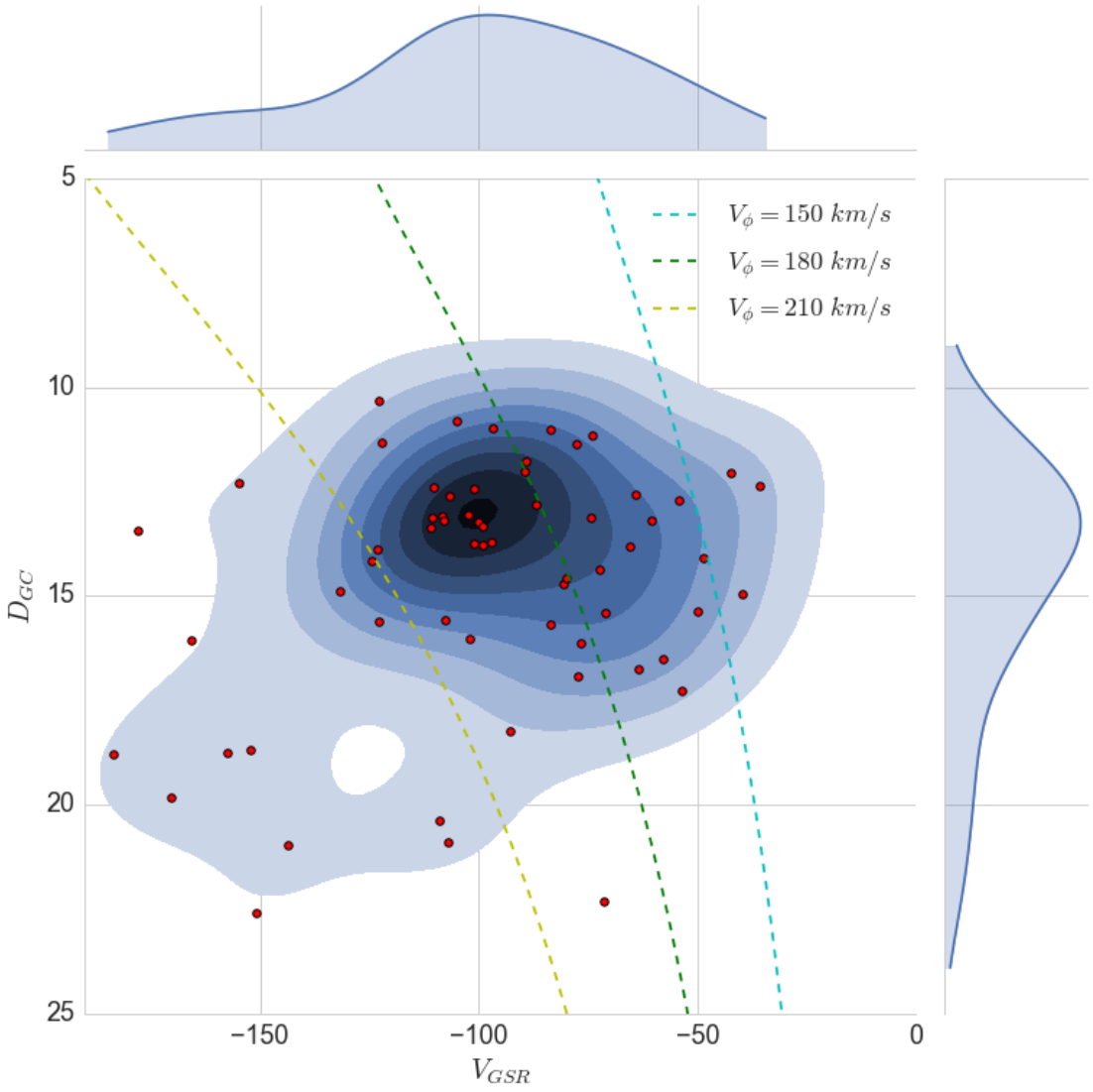

Figure 4.9: BSS-BHB separation in SDSS data using the stellar parameters

Anna Ho et. al. measured the alpha element abundance for the all LAMOST DR12 giants using The Cannon. This was the first attempt to measure the $[\alpha/M]$ for these objects but cautioned about their accuracy given the limits in their training set. Nevertheless, we attempted to measure $[\alpha/M]$ with The Cannon using LAMOST training data. The distribution of the stars in the $([Fe/H], [\alpha/M])$ plane is shown in the figure.

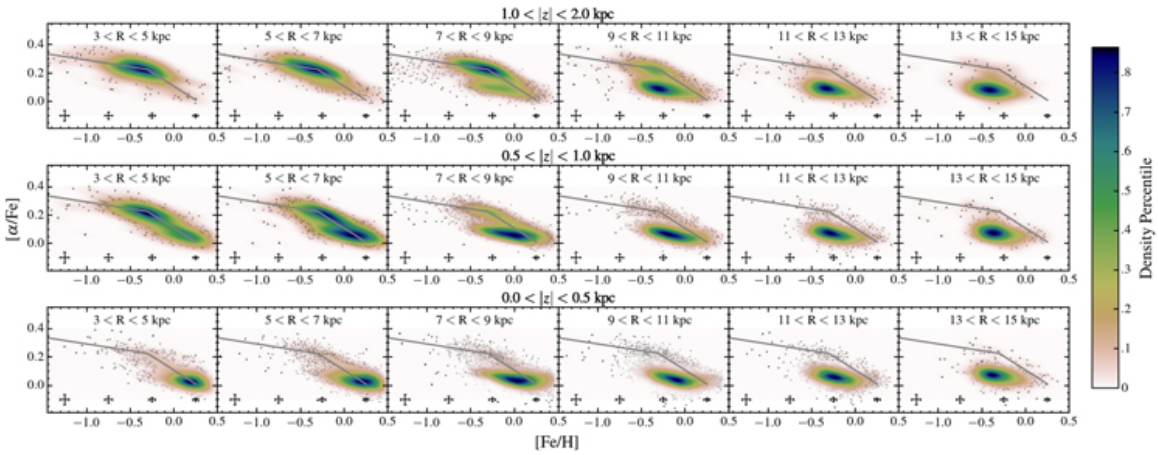

Figure 4.10: Stellar distribution of stars in the [/Fe] vs. [Fe/H] plane as a function of R and $|z|$.

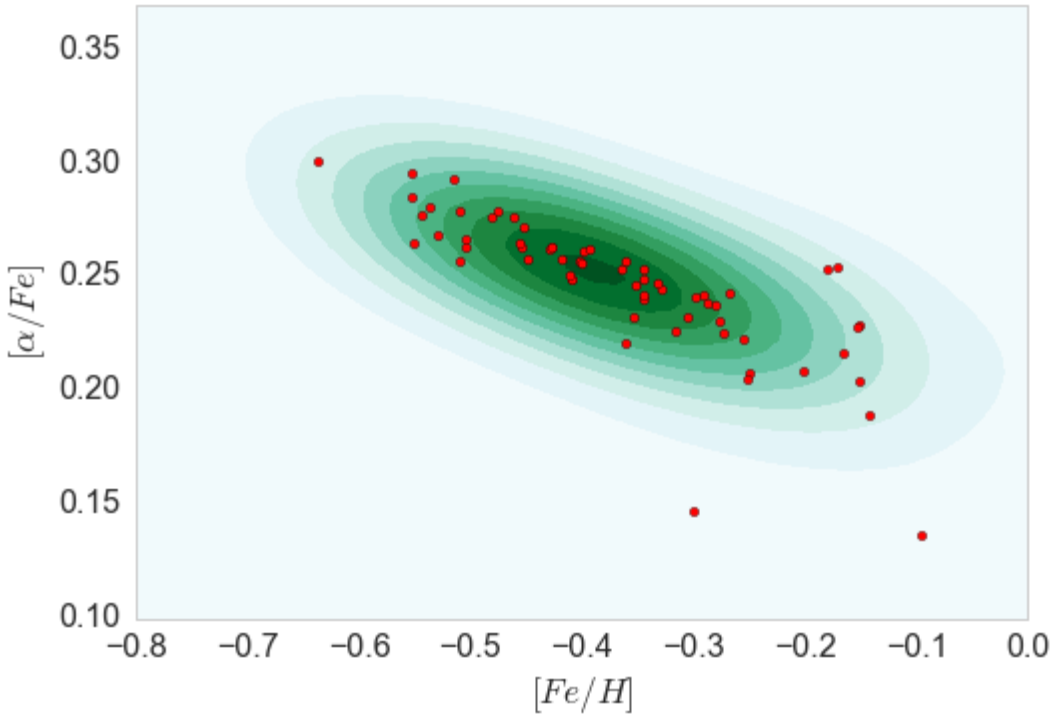

Figure 4.11: Distribution of stars in the [/Fe] vs. [Fe/H] plane for our stars.

In order to compare our results with Hayden et. al, we calculated the vertical

distance to stars from the Galactic plane (Z height). This can easily be calculated from the distance and the declination angle using the equation, $Z\ Height = D_{GC}\ sinb$. The distribution of $Z\ Height$ is give in Figure 4.12.

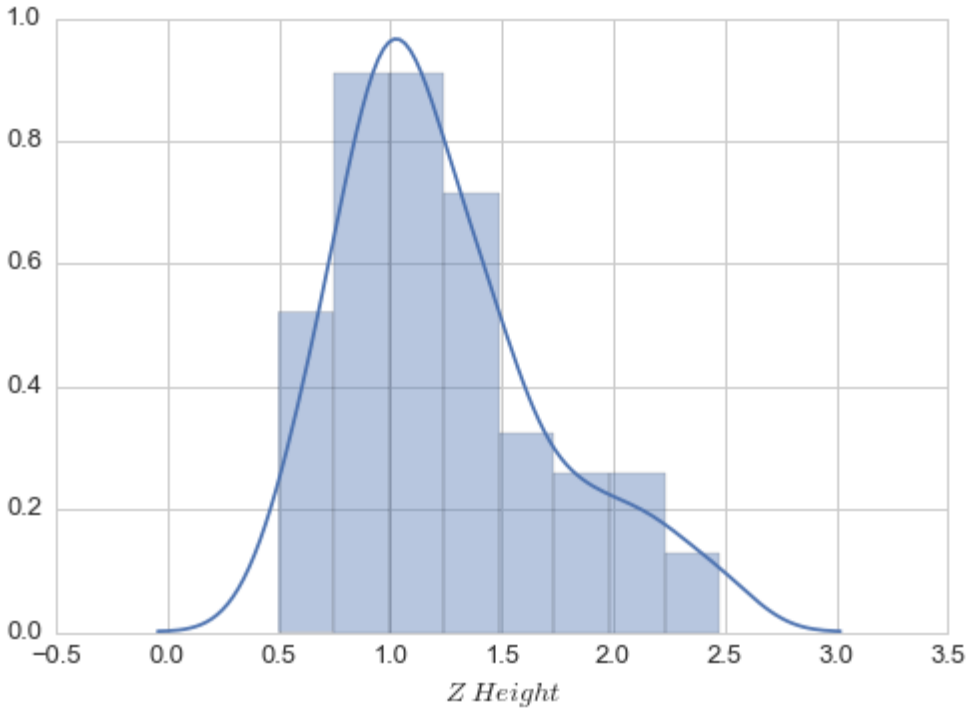

Figure 4.12: Distribution of the height to the stars from the Galactic plane.

According to Figure 4.10, there are very few alpha-enhanced stars beyond the Galactocentric distance of 11 kpc. Interestingly, our sample is dominated by high-alpha stars, with the average value of $[Fe/H] \sim 0.2\ dex$.

The disk stars formed via the merger or accretion could be the origin of -enhanced sequence observed in Milky Way. Brook et.al. (2005,) simulated the thick disk formed via multiple gas-rich minor mergers, to show the origin of the alpha-enhanced stars with relatively low-metallicity like our sample.

4.3 Summary

Using sample of red clump stars, we were able to estimate the chemical and kinematical charactor of the Canis Major Overdensity. The overall metallicity is in agreement with expected value for thick disk stars at this distance. The avarage alpha abundance for these stars is ~ 0.25 dex. This is in contrast with the few low-alpha stars observed at Galactocentric distances > 11 kpc of Hayden et.al.

The kinematic distribution of RC stars supports a mixture of thin/thick disk stars, while the large dispersion of the velocity does not favor a dynamically cold structure.

Few of the concerns we had during this study needs to be mentioned here.

The temperatures of the stars obtained from ULySS are 300 K higher than the temperatures obtained from *The Cannon*. This same offst was observed between the temperatures calculated from the spectrum fitting package, *SPAce* (Stellar Parameters and Chemical abundance Estimator)[3] and *The Cannon*. However, the temperatures obtained from *The Cannon* are consistant with temperatures predicted by both stellar isochrones and the APOGEE catalog at this metallicity.

As a test study we estimated $E(B-V)$ using the stellar parameters adopted from ULySS. This gave us mean $E(B-V)$ of 0.3. A separate study conducted by our group using the Blue Plume stars also predicted $E(B-V) \sim 0.3$ towards the CMO. Interestingly, this is in agreement with the Galactic dust maps obtained from Plank collaboration.

Also, we estimated the $[\alpha/Fe]$ for our sample using the *SPAce*. This gave us mean $[\alpha/Fe] \sim 0.$, which is consistant with the Hayden et.al. (2014). Again, we emphasize that the $[\alpha/Fe]$ derived from *The Cannon* depend on the accuracy of the $[\alpha/Fe]$ estimates of the training set and the accuracy of the LAMOST $[\alpha/Fe]$ values are not being fully tested yet.

[3] http://dc.g-vo.org/

Chapter 5 Summary and Conclusion

In this work we utilized many different strategies to determine the stellar parameters of individual stars. To that end we used all available flux data for a given star. The main conclusions of the work can be summarised as follows.

5.1 Stellar Parameters in UV

We evaluated the consistency between observed energy distribution of metal-poor A-type stars and that of Kurucz(ATLAS12) models, especially focusing on the UV wavelengths. We noticed that the observed and model energy distributions agreed quite well overall, with slight deviation at far-UV wavelengths. We have estimated that the model fluxes below 2000 Å predict less flux than the observed flux.

5.2 Blue Straggler Stars in the Galactic Field

Combining the flux data from optical and ultraviolet surveys, we were able to adentify 85 hot and young white dwarf companions to field blue straggler stars and measure their stellar parameters. Based on the WD parameter distribution we conclude that majority of the WDs are helium WDs formed through case-B mass transfer. Combining the WD stellar parameters with the evolutionary models we estimated the lower limit of the binary mass transfer efficiency in these stars to be, $\beta = 0.5$.

5.3 Canis Major Overdensity

The chemical and kinematical charactor of the red clump stars of the Canis Major Overdensity suggest an in-situ origin of the CMO. The kinematic distribution of RC stars supports a mixture of thin/thick disk stars, while the large dispersion of

the velocity does not favor a dynamically cold structure. The measured interstellar reddening towards CMO is in agreement with the work of Schlegel et. al (1998).

Bibliography

[1] Planck Collaboration, R. Adam, P. A. R. Ade, N. Aghanim, Y. Akrami, M. I. R. Alves, F. Argüeso, M. Arnaud, F. Arroja, M. Ashdown, and et al. Planck 2015 results. I. Overview of products and scientific results. *A&A*, 594:A1, September 2016.

[2] M. Fukugita and P. J. E. Peebles. The Cosmic Energy Inventory. *ApJ*, 616:643–668, December 2004.

[3] P. et.al. André. From filamentary clouds to prestellar cores to the stellar IMF: Initial highlights from the Herschel Gould Belt Survey. *A&A*, 518:L102, July 2010.

[4] F. LeBlanc. *An Introduction to Stellar Astrophysics*. 2010.

[5] Ž. Ivezić, B. Sesar, M. Jurić, N. Bond, J. Dalcanton, C. M. Rockosi, B. Yanny, H. J. Newberg, T. C. Beers, C. Allende Prieto, R. Wilhelm, Y. S. Lee, T. Sivarani, J. E. Norris, C. A. L. Bailer-Jones, P. Re Fiorentin, D. Schlegel, A. Uomoto, R. H. Lupton, G. R. Knapp, J. E. Gunn, K. R. Covey, J. Allyn Smith, G. Miknaitis, M. Doi, M. Tanaka, M. Fukugita, S. Kent, D. Finkbeiner, J. A. Munn, J. R. Pier, T. Quinn, S. Hawley, S. Anderson, F. Kiuchi, A. Chen, J. Bushong, H. Sohi, D. Haggard, A. Kimball, J. Barentine, H. Brewington, M. Harvanek, S. Kleinman, J. Krzesinski, D. Long, A. Nitta, S. Snedden, B. Lee, H. Harris, J. Brinkmann, D. P. Schneider, and D. G. York. The Milky Way Tomography with SDSS. II. Stellar Metallicity. *ApJ*, 684:287–325, September 2008.

[6] J. Debosscher, L. M. Sarro, C. Aerts, J. Cuypers, B. Vandenbussche, R. Garrido,

and E. Solano. VizieR Online Data Catalog: Supervised classification of variable stars (Debosscher+, 2007). *VizieR Online Data Catalog*, 347, November 2007.

[7] P. Dubath, L. Rimoldini, M. Süveges, J. Blomme, M. López, L. M. Sarro, J. De Ridder, J. Cuypers, L. Guy, I. Lecoeur, K. Nienartowicz, A. Jan, M. Beck, N. Mowlavi, P. De Cat, T. Lebzelter, and L. Eyer. Random forest automated supervised classification of Hipparcos periodic variable stars. *MNRAS*, 414:2602–2617, July 2011.

[8] D. N. C. Lin and S. M. Faber. Some implications of nonluminous matter in dwarf spheroidal galaxies. *ApJ*, 266:L21–L25, March 1983.

[9] F. Beutler, C. Blake, M. Colless, D. H. Jones, L. Staveley-Smith, L. Campbell, Q. Parker, W. Saunders, and F. Watson. The 6dF Galaxy Survey: baryon acoustic oscillations and the local Hubble constant. *MNRAS*, 416:3017–3032, October 2011.

[10] M. Montes, J. A. Acosta-Pulido, M. A. Prieto, and J. A. Fernández-Ontiveros. The innermost globular clusters of M87. *MNRAS*, 442:1350–1362, August 2014.

[11] F. Hernández-Pérez and G. Bruzual. Binary stars and the UVX in early-type galaxies. *MNRAS*, 444:2571–2579, November 2014.

[12] S. Kaviraj, K. Schawinski, J. E. G. Devriendt, I. Ferreras, S. Khochfar, S.-J. Yoon, S. K. Yi, J.-M. Deharveng, A. Boselli, T. Barlow, T. Conrow, K. Forster, P. G. Friedman, D. C. Martin, P. Morrissey, S. Neff, D. Schiminovich, M. Seibert, T. Small, T. Wyder, L. Bianchi, J. Donas, T. Heckman, Y.-W. Lee, B. Madore, B. Milliard, R. M. Rich, and A. Szalay. UV-Optical Colors As Probes of Early-Type Galaxy Evolution. *ApJS*, 173:619–642, December 2007.

[13] H.-c. Lee, Y.-W. Lee, and B. K. Gibson. Horizontal-Branch Morphology and the Photometric Evolution of Old Stellar Populations. *AJ*, 124:2664–2676, November 2002.

[14] C. Maraston and D. Thomas. Strong Balmer Lines in Old Stellar Populations: No Need for Young Ages in Ellipticals? *ApJ*, 541:126–133, September 2000.

[15] J. A. Rose. Spectral anomalies in the Hyades and Pleiades and in field stars with active chromospheres. *AJ*, 89:1238–1251, August 1984.

[16] D. P. Huenemoerder and S. C. Barden. Spectroscopy of RS CVn and W UMa Systems: Extraction of Component Spectra. In *Bulletin of the American Astronomical Society*, volume 16 of *BAAS*, page 510, March 1984.

[17] M. N. Fanelli, R. W. O'Connell, D. Burstein, and C.-C. Wu. Spectral synthesis in the ultraviolet. IV - A library of mean stellar groups. *ApJS*, 82:197–245, September 1992.

[18] A. Heck, D. Egret, M. Jaschek, and C. Jaschek. IUE low-dispersion spectra flux catalogue. I - Normal stars (magnetic tape). *A&AS*, 57:213–216, August 1984.

[19] M. D. Gregg, D. Silva, J. Rayner, F. Valdes, G. Worthey, A. Pickles, J. A. Rose, W. Vacca, and B. Carney. The HST/STIS Next Generation Spectral Library. In *American Astronomical Society Meeting Abstracts*, volume 36 of *Bulletin of the American Astronomical Society*, page 1496, December 2004.

[20] J. A. Cardelli, G. C. Clayton, and J. S. Mathis. The relationship between infrared, optical, and ultraviolet extinction. *ApJ*, 345:245–256, October 1989.

[21] R. O. Gray and C. J. Corbally. The calibration of MK spectral classes using spectral synthesis. 1: The effective temperature calibration of dwarf stars. *AJ*, 107:742–746, February 1994.

[22] A. R. Sandage. The color-magnitude diagram for the globular cluster M 3. *AJ*, 58:61–75, 1953.

[23] R. D. Mathieu and A. M. Geller. A binary star fraction of 76 per cent and unusual orbit parameters for the blue stragglers of NGC 188. *Nature*, 462:1032–1035, December 2009.

[24] F. R. Ferraro, B. Paltrinieri, R. T. Rood, and B. Dorman. Blue Straggler Stars: The Spectacular Population in M80. *ApJ*, 522:983–990, September 1999.

[25] Y. Momany, E. V. Held, I. Saviane, S. Zaggia, L. Rizzi, and M. Gullieuszik. The blue plume population in dwarf spheroidal galaxies. Genuine blue stragglers or young stellar population? *A&A*, 468:973–978, June 2007.

[26] G. W. Preston and C. Sneden. What Are These Blue Metal-Poor Stars? *AJ*, 120:1014–1055, August 2000.

[27] L. Deng, R. Chen, X. S. Liu, and J. S. Chen. The Blue Stragglers in M67 and Single-Population Synthesis. *ApJ*, 524:824–830, October 1999.

[28] J. C. Wheeler. Blue stragglers as long-lived stars. *ApJ*, 234:569–578, December 1979.

[29] W. H. McCrea. Extended main-sequence of some stellar clusters. *MNRAS*, 128:147, 1964.

[30] R. Kippenhahn and A. Weigert. Entwicklung in engen Doppelsternsystemen I. Massenaustausch vor und nach Beendigung des zentralen Wasserstoff-Brennens. *ZAp*, 65:251, 1967.

[31] X. Chen and Z. Han. Primordial binary evolution and blue stragglers. *MNRAS*, 395:1822–1836, June 2009.

[32] S. G. Ryan, S. G. Gregory, U. Kolb, T. C. Beers, and T. Kajino. Rapid Rotation of Ultra-Li-depleted Halo Stars and Their Association with Blue Stragglers. *ApJ*, 571:501–511, May 2002.

[33] G. W. Preston and A. U. Landolt. Pulsating Blue Metal-poor Stars. *AJ*, 118:3006–3015, December 1999.

[34] B. Yanny, H. J. Newberg, S. Kent, S. A. Laurent-Muehleisen, J. R. Pier, G. T. Richards, C. Stoughton, J. E. Anderson, Jr., J. Annis, J. Brinkmann, B. Chen, I. Csabai, M. Doi, M. Fukugita, G. S. Hennessy, Ž. Ivezić, G. R. Knapp, R. Lupton, J. A. Munn, T. Nash, C. M. Rockosi, D. P. Schneider, J. A. Smith, and D. G. York. Identification of A-colored Stars and Structure in the Halo of the Milky Way from Sloan Digital Sky Survey Commissioning Data. *ApJ*, 540:825–841, September 2000.

[35] E. Sirko, J. Goodman, G. R. Knapp, J. Brinkmann, Ž. Ivezić, E. J. Knerr, D. Schlegel, D. P. Schneider, and D. G. York. Blue Horizontal-Branch Stars in the Sloan Digital Sky Survey. II. Kinematics of the Galactic Halo. *AJ*, 127:914–924, February 2004.

[36] X. X. Xue, H. W. Rix, G. Zhao, P. Re Fiorentin, T. Naab, M. Steinmetz, F. C. van den Bosch, T. C. Beers, Y. S. Lee, E. F. Bell, C. Rockosi, B. Yanny, H. Newberg, R. Wilhelm, X. Kang, M. C. Smith, and D. P. Schneider. The Milky Way's Circular Velocity Curve to 60 kpc and an Estimate of the Dark Matter Halo Mass from the Kinematics of ˜2400 SDSS Blue Horizontal-Branch Stars. *ApJ*, 684:1143–1158, September 2008.

[37] Y. S. Lee, T. C. Beers, T. Sivarani, C. Allende Prieto, L. Koesterke, R. Wilhelm, P. Re Fiorentin, C. A. L. Bailer-Jones, J. E. Norris, C. M. Rockosi, B. Yanny, H. J. Newberg, K. R. Covey, H.-T. Zhang, and A.-L. Luo. The SEGUE Stellar

Parameter Pipeline. I. Description and Comparison of Individual Methods. *AJ*, 136:2022–2049, November 2008.

[38] Tamás Budavári et.al. Galex-sdss catalogs for statistical studies. *The Astrophysical Journal*, 694(2):1281, 2009.

[39] E. F. Schlafly and D. P. Finkbeiner. Measuring Reddening with Sloan Digital Sky Survey Stellar Spectra and Recalibrating SFD. *ApJ*, 737:103, August 2011.

[40] S.-C. Rey, R. M. Rich, S. T. Sohn, S.-J. Yoon, C. Chung, S. K. Yi, Y.-W. Lee, J. Rhee, L. Bianchi, B. F. Madore, K. Lee, T. A. Barlow, K. Forster, P. G. Friedman, D. C. Martin, P. Morrissey, S. G. Neff, D. Schiminovich, M. Seibert, T. Small, T. K. Wyder, J. Donas, T. M. Heckman, B. Milliard, A. S. Szalay, and B. Y. Welsh. GALEX Ultraviolet Photometry of Globular Clusters in M31: Three-Year Results and a Catalog. *ApJS*, 173:643–658, December 2007.

[41] D. J. Schlegel, D. P. Finkbeiner, and M. Davis. Maps of Dust Infrared Emission for Use in Estimation of Reddening and Cosmic Microwave Background Radiation Foregrounds. *ApJ*, 500:525–553, June 1998.

[42] A. Rebassa-Mansergas, A. Nebot Gómez-Morán, M. R. Schreiber, B. T. Gänsicke, A. Schwope, J. Gallardo, and D. Koester. Post-common envelope binaries from SDSS - XIV. The DR7 white dwarf-main-sequence binary catalogue. *MNRAS*, 419:806–816, January 2012.

[43] M. A. Smith, L. Bianchi, and B. Shiao. Interesting Features in the Combined GALEX and Sloan Color Diagrams of Solar-like Galactic Populations. *AJ*, 147:159, June 2014.

[44] M. A. Wood. Theoretical White Dwarf Luminosity Functions: DA Models. In D. Koester and K. Werner, editors, *White Dwarfs*, volume 443 of *Lecture Notes in Physics, Berlin Springer Verlag*, page 41, 1995.

[45] G. Fontaine, P. Brassard, and P. Bergeron. The Potential of White Dwarf Cosmochronology. *PASP*, 113:409–435, April 2001.

[46] M. Fukugita, T. Ichikawa, J. E. Gunn, M. Doi, K. Shimasaku, and D. P. Schneider. The Sloan Digital Sky Survey Photometric System. *AJ*, 111:1748, April 1996.

[47] C. Zhao and H. J. Newberg. Transformation from SDSS Photometric System to Johnson-Morgan-Cousins System in HK Survey. *ArXiv Astrophysics e-prints*, December 2006.

[48] T. C. Beers, D. Carollo, Ž. Ivezić, D. An, M. Chiba, J. E. Norris, K. C. Freeman, Y. S. Lee, J. A. Munn, P. Re Fiorentin, T. Sivarani, R. Wilhelm, B. Yanny, and D. G. York. The Case for the Dual Halo of the Milky Way. *ApJ*, 746:34, February 2012.

[49] T. D. Kinman, N. B. Suntzeff, and R. P. Kraft. The structure of the galactic halo outside the solar circle as traced by the blue horizontal branch stars. *AJ*, 108:1722–1772, November 1994.

[50] G. Torres. On the Use of Empirical Bolometric Corrections for Stars. *AJ*, 140:1158–1162, November 2010.

[51] J. R. Hurley, C. A. Tout, and O. R. Pols. Evolution of binary stars and the effect of tides on binary populations. *MNRAS*, 329:897–928, February 2002.

[52] Donald Knuth. Knuth: Computers and typesetting.

[53] Y. Momany, S. R. Zaggia, P. Bonifacio, G. Piotto, F. De Angeli, L. R. Bedin, and G. Carraro. Probing the Canis Major stellar over-density as due to the Galactic warp. *A&A*, 421:L29–L32, July 2004.

[54] J. P. De Greve and C. De Loore. Evolution of massive close binaries. *A&AS*, 96:653–663, December 1992.

[55] X. Chen and Z. Han. Primordial binary evolution and blue stragglers. *MNRAS*, 395:1822–1836, June 2009.

[56] A. Pietrinferni, S. Cassisi, M. Salaris, and F. Castelli. A Large Stellar Evolution Database for Population Synthesis Studies. II. Stellar Models and Isochrones for an α-enhanced Metal Distribution. *ApJ*, 642:797–812, May 2006.

[57] P. Jofré and A. Weiss. The age of the Milky Way halo stars from the Sloan Digital Sky Survey. *A&A*, 533:A59, September 2011.

[58] N. F. Martin, R. A. Ibata, M. Bellazzini, M. J. Irwin, G. F. Lewis, and W. Dehnen. A dwarf galaxy remnant in Canis Major: the fossil of an in-plane accretion on to the Milky Way. *MNRAS*, 348:12–23, February 2004.

[59] H. J. Newberg, B. Yanny, C. Rockosi, E. K. Grebel, H.-W. Rix, J. Brinkmann, I. Csabai, G. Hennessy, R. B. Hindsley, R. Ibata, Z. Ivezić, D. Lamb, E. T. Nash, M. Odenkirchen, H. A. Rave, D. P. Schneider, J. A. Smith, A. Stolte, and D. G. York. The Ghost of Sagittarius and Lumps in the Halo of the Milky Way. *ApJ*, 569:245–274, April 2002.

[60] J. Peñarrubia and A. J. Benson. Effects of dynamical evolution on the distribution of substructures. *MNRAS*, 364:977–989, December 2005.

[61] Y. Momany, S. R. Zaggia, P. Bonifacio, G. Piotto, F. De Angeli, L. R. Bedin, and G. Carraro. Probing the Canis Major stellar over-density as due to the Galactic warp. *A&A*, 421:L29–L32, July 2004.

[62] D. J. Schlegel, D. P. Finkbeiner, and M. Davis. Maps of Dust Infrared Emission for Use in Estimation of Reddening and Cosmic Microwave Background Radiation Foregrounds. *ApJ*, 500:525–553, June 1998.

[63] P. Bonifacio, V. Hill, P. Molaro, L. Pasquini, P. Di Marcantonio, and P. Santin. First results of UVES at VLT: abundances in the Sgr dSph. *A&A*, 359:663–668, July 2000.

[64] D. Hatzidimitriou and M. R. S. Hawkins. Stellar populations and large-scale structure of the SMC. II - Geometry of the north-eastern and south-western outlying regions. *MNRAS*, 241:667–690, December 1989.

[65] L. Girardi and M. Salaris. Population effects on the red giant clump absolute magnitude, and distance determinations to nearby galaxies. *MNRAS*, 323:109–129, May 2001.

[66] K. Z. Stanek and P. M. Garnavich. Red Clump Stars - New, Improved Distance Indicator. In *American Astronomical Society Meeting Abstracts*, volume 30 of *Bulletin of the American Astronomical Society*, page 1409, December 1998.

[67] K. C. Chambers, E. A. Magnier, N. Metcalfe, H. A. Flewelling, M. E. Huber, C. Z. Waters, L. Denneau, P. W. Draper, D. Farrow, D. P. Finkbeiner, C. Holmberg, J. Koppenhoefer, P. A. Price, R. P. Saglia, E. F. Schlafly, S. J. Smartt, W. Sweeney, R. J. Wainscoat, W. S. Burgett, T. Grav, J. N. Heasley, K. W. Hodapp, R. Jedicke, N. Kaiser, R.-P. Kudritzki, G. A. Luppino, R. H. Lupton, D. G. Monet, J. S. Morgan, P. M. Onaka, C. W. Stubbs, J. L. Tonry, E. Banados, E. F. Bell, R. Bender, E. J. Bernard, M. T. Botticella, S. Casertano, S. Chastel, W.-P. Chen, X. Chen, S. Cole, N. Deacon, C. Frenk, A. Fitzsimmons, S. Gezari, C. Goessl, T. Goggia, B. Goldman, E. K. Grebel, N. C. Hambly, G. Hasinger, A. F. Heavens, T. M. Heckman, R. Henderson, T. Henning, M. Holman, U. Hopp, W.-H. Ip, S. Isani, C. D. Keyes, A. Koekemoer, R. Kotak, K. S. Long, J. R Lucey, M. Liu, N. F. Martin, B. McLean, E. Morganson, D. N. A. Murphy, M. A. Nieto-Santisteban, P. Norberg, J. A. Peacock, E. A. Pier, M. Postman, N. Primak, C. Rae, A. Rest, A. Riess, A. Riffeser, H. W. Rix,

S. Roser, E. Schilbach, A. S. B. Schultz, D. Scolnic, A. Szalay, S. Seitz, B. Shiao, E. Small, K. W. Smith, D. Soderblom, A. N. Taylor, A. R. Thakar, J. Thiel, D. Thilker, Y. Urata, J. Valenti, F. Walter, S. P. Watters, S. Werner, R. White, W. M. Wood-Vasey, and R. Wyse. The Pan-STARRS1 Surveys. *ArXiv e-prints*, December 2016.

[68] J. Bovy, D. L. Nidever, H.-W. Rix, L. Girardi, G. Zasowski, S. D. Chojnowski, J. Holtzman, C. Epstein, P. M. Frinchaboy, M. R. Hayden, T. S. Rodrigues, S. R. Majewski, J. A. Johnson, M. H. Pinsonneault, D. Stello, C. Allende Prieto, B. Andrews, S. Basu, T. C. Beers, D. Bizyaev, A. Burton, W. J. Chaplin, K. Cunha, Y. Elsworth, R. A. García, D. A. García-Herńandez, A. E. García Pérez, F. R. Hearty, S. Hekker, T. Kallinger, K. Kinemuchi, L. Koesterke, S. Mészáros, B. Mosser, R. W. O'Connell, D. Oravetz, K. Pan, A. C. Robin, R. P. Schiavon, D. P. Schneider, M. Schultheis, A. Serenelli, M. Shetrone, V. Silva Aguirre, A. Simmons, M. Skrutskie, V. V. Smith, K. Stassun, D. H. Weinberg, J. C. Wilson, and O. Zamora. The APOGEE Red-clump Catalog: Precise Distances, Velocities, and High-resolution Elemental Abundances over a Large Area of the Milky Way's Disk. *ApJ*, 790:127, August 2014.

[69] A. Y. Q. Ho, M. K. Ness, D. W. Hogg, H.-W. Rix, C. Liu, F. Yang, Y. Zhang, Y. Hou, and Y. Wang. Label Transfer from APOGEE to LAMOST: Precise Stellar Parameters for 450,000 LAMOST Giants. *ApJ*, 836:5, February 2017.

[70] M. Koleva, P. Prugniel, A. Bouchard, and Y. Wu. ULySS: a full spectrum fitting package. *A&A*, 501:1269–1279, July 2009.

[71] M. Ness, D. W. Hogg, H.-W. Rix, A. Y. Q. Ho, and G. Zasowski. The Cannon: A data-driven approach to Stellar Label Determination. *ApJ*, 808:16, July 2015.

[72] X.-Q. Cui, Y.-H. Zhao, Y.-Q. Chu, G.-P. Li, Q. Li, L.-P. Zhang, H.-J. Su, Z.-Q.

Yao, Y.-N. Wang, X.-Z. Xing, X.-N. Li, Y.-T. Zhu, G. Wang, B.-Z. Gu, A.-L. Luo, X.-Q. Xu, Z.-C. Zhang, G.-R. Liu, H.-T. Zhang, D.-H. Yang, S.-Y. Cao, H.-Y. Chen, J.-J. Chen, K.-X. Chen, Y. Chen, J.-R. Chu, L. Feng, X.-F. Gong, Y.-H. Hou, H.-Z. Hu, N.-S. Hu, Z.-W. Hu, L. Jia, F.-H. Jiang, X. Jiang, Z.-B. Jiang, G. Jin, A.-H. Li, Y. Li, Y.-P. Li, G.-Q. Liu, Z.-G. Liu, W.-Z. Lu, Y.-D. Mao, L. Men, Y.-J. Qi, Z.-X. Qi, H.-M. Shi, Z.-H. Tang, Q.-S. Tao, D.-Q. Wang, D. Wang, G.-M. Wang, H. Wang, J.-N. Wang, J. Wang, J.-L. Wang, J.-P. Wang, L. Wang, S.-Q. Wang, Y. Wang, Y.-F. Wang, L.-Z. Xu, Y. Xu, S.-H. Yang, Y. Yu, H. Yuan, X.-Y. Yuan, C. Zhai, J. Zhang, Y.-X. Zhang, Y. Zhang, M. Zhao, F. Zhou, G.-H. Zhou, J. Zhu, and S.-C. Zou. The Large Sky Area Multi-Object Fiber Spectroscopic Telescope (LAMOST). *Research in Astronomy and Astrophysics*, 12:1197–1242, September 2012.

[73] M. S. Bessell. UBVRI passbands. *PASP*, 102:1181–1199, October 1990.

[74] J. L. Tonry, C. W. Stubbs, K. R. Lykke, P. Doherty, I. S. Shivvers, W. S. Burgett, K. C. Chambers, K. W. Hodapp, N. Kaiser, R.-P. Kudritzki, E. A. Magnier, J. S. Morgan, P. A. Price, and R. J. Wainscoat. The Pan-STARRS1 Photometric System. *ApJ*, 750:99, May 2012.

[75] K. Z. Stanek and P. M. Garnavich. Distance to M31 with the Hubble Space Telescope and HIPPARCOS Red Clump Stars. *ApJ*, 503:L131–L134, August 1998.

[76] M. Valentini and U. Munari. A spectroscopic survey of faint, high-Galactic-latitude red clump stars. I. The high resolution sample. *A&A*, 522:A79, November 2010.

[77] D. R. Alves. K-Band Calibration of the Red Clump Luminosity. *ApJ*, 539:732–741, August 2000.

[78] V. van Helshoecht and M. A. T. Groenewegen. K-band magnitude of the red clump as a distance indicator. *A&A*, 463:559–565, February 2007.

[79] L.-C. Deng, H. J. Newberg, C. Liu, J. L. Carlin, T. C. Beers, L. Chen, Y.-Q. Chen, N. Christlieb, C. J. Grillmair, P. Guhathakurta, Z.-W. Han, J.-L. Hou, H.-T. Lee, S. Lépine, J. Li, X.-W. Liu, K.-K. Pan, J. A. Sellwood, B. Wang, H.-C. Wang, F. Yang, B. Yanny, H.-T. Zhang, Y.-Y. Zhang, Z. Zheng, and Z. Zhu. LAMOST Experiment for Galactic Understanding and Exploration (LEGUE) The survey's science plan. *Research in Astronomy and Astrophysics*, 12:735–754, July 2012.

[80] W. Dehnen and J. J. Binney. Local stellar kinematics from HIPPARCOS data. *MNRAS*, 298:387–394, August 1998.

[81] A. Boehle, A. M. Ghez, R. Schödel, L. Meyer, S. Yelda, S. Albers, G. D. Martinez, E. E. Becklin, T. Do, J. R. Lu, K. Matthews, M. R. Morris, B. Sitarski, and G. Witzel. An Improved Distance and Mass Estimate for Sgr A* from a Multistar Orbit Analysis. *ApJ*, 830:17, October 2016.

[82] W. D. Arnett. On the bulk yields of nucleosynthesis from massive stars. *ApJ*, 219:1008–1016, February 1978.

[83] M. R. Hayden, J. A. Holtzman, J. Bovy, S. R. Majewski, J. A. Johnson, C. Allende Prieto, T. C. Beers, K. Cunha, P. M. Frinchaboy, A. E. García Pérez, L. Girardi, F. R. Hearty, Y. S. Lee, D. Nidever, R. P. Schiavon, K. J. Schlesinger, D. P. Schneider, M. Schultheis, M. Shetrone, V. V. Smith, G. Zasowski, D. Bizyaev, D. Feuillet, S. Hasselquist, K. Kinemuchi, E. Malanushenko, V. Malanushenko, R. O'Connell, K. Pan, and K. Stassun. Chemical Cartography with APOGEE: Large-scale Mean Metallicity Maps of the Milky Way Disk. *AJ*, 147:116, May 2014.

Vita

Gemunu Ekanayake

Education

Ph.D. Physics ..... expected May 2017

University of Kentucky, Lexington, Kentucky, United States

M.Sc. Physics ..... May 2014

University of Kentucky, Lexington, Kentucky, United States

B.S. Physics ..... August 2008

University of Peradeniya, Kandy, Sri Lanka

Professional Positions Held

Graduate Assistant ..... Sept 2015 - present

University of Kentucky, Lexington, Kentucky, United States

Teaching Assistant ..... Sept 2009 - May 2013

University of Kentucky, Lexington, Kentucky, United States

Society Memberships

American Physical Society

American Astronomical Society